Measurement of the strange quark contribution to the proton spin using neutral kaons at HERMES

Inaugural-Dissertation
zur Erlangung des Doktorgrades der Naturwissenschaften
der Justus-Liebig-Universität Giessen
Fachbereich 07
(Mathematik und Informatik, Physik, Geographie)

vorgelegt von

Shaojun Lu
aus
Jilin, P. R. China

II. Physikalisches Institut der Justus-Liebig-Universität Giessen
January 2007

This work was supported by Deutsche Forschungsgemeinschaft (DFG) and German Bundesministerium für Bildung und Forschung (BMBF).

Supervisor: Prof. Dr. M.Düren

Dekan : Prof. Dr. B. Baumann

1. Berichterstatter: Prof. Dr. M. Düren
2. Berichterstatter: Prof. Dr. A. Müller

Zusammenfassung

Ziel des HERMES-Experiments am DESY (Hamburg) ist die präzise Vermessung der Spinstruktur des Protons mittels tiefinelastischer Lepton-Nukleon-Streuung. Hierzu wird der in der HERMES- Wechselwirkungszone longitudinal polarisierte Positronen-Strahl des HERA-Beschleunigers mit einem Impuls von 27,5 GeV/c an einem ebenfalls longitudinal polarisierten Gastarget gestreut.

Eine erfolgreiche Beschreibung der Wechselwirkungsprozesse zwischen Quarks und Gluonen ist nach allgemeiner Auffassung der Schlüssel zum Verständnis der Grundlangen des Nukleonenspins. Die innere Struktur des Nukleons kann durch die Partonverteilungen der Quarks und der Gluonen, aus denen das Nukleon aufgebaut ist, dargestellt werden. Die spin-gemittelten PDFs (parton distribution functions) repräsentieren die Impulsverteilungen der Quarks und Antiquarks, der Quarkflavours $q = (u, d, s)$. Die Helizitätsverteilungen $\Delta q(x) = q^{\uparrow\uparrow}(x) - q^{\uparrow\downarrow}(x)$ beschreiben den flavourabhängigen Beitrag der Konstituentenquarks zum Nukleonenspin.

Die Helizitätsverteilung des Strange-Quark-Sees $\Delta S(x)$, ist hierbei von besonderem Interesse, da ihre Eigenschaften zum Verständnis des für die Entstehung des Quark-Sees verantwortlichen Reaktionsmechanismus beitragen können. Ein Großteil unseres Verständnisses der Spinstruktur des Nukleons und insbesondere die Tatsache, dass nur ein unerwartet kleiner Anteil des Nukleonenspins von den Spins der Quarks herrührt, basiert auf inklusiven Analysen der Daten aus tief-inelastischen Streuexperimenten sowie des Hyperonenzerfalls unter der Annahme von SU(3)-Symmetrie zwischen den Strukturen des Baryon-Oktetts. In solchen Experimenten jedoch ist die Helizitätsverteilung der Strange-Quarks keiner direkten Messung zugänglich. Diese Messungen deuteten auf eine beträchtliche negative Polarisation des Strange-Quark-Sees hin. Dies wurde als Ursache für die ebenfalls in diesen Analysen beobachtete Verletzung der Ellis-Jaffe-Summenregel angesehen. Darüber hinaus lässt

eine von Null verschiedene Polarisation der Strange-Quarks insoweit Rückschlüsse auf eine beträchtliche Polarisation der Gluonen zu, als Seequarks durch die Aufspaltung von Gluonen erzeugt werden. In der Tat wurden aufgrund der beobachteten negativen Strange-Quark-Polarisation Spekulationen bezüglich einer stark positiven Gluonenpolarisation angestellt.

Im Gegensatz zu den erwähnten inklusiven Analysen deuten aktuelle semi-inklusive Messungen von HERMES darauf hin, dass der Strange-Quark-See unpolarisiert ist. Eine Analyse, bei der Daten von Proton- und Deuteron-Targets komplett nach fünf Quarkflavours separiert wurden (die Analyse ist insensitiv auf $\Delta\bar{s}$), ergab einen Wert von $\Delta s = 0.028 \pm 0.033 \pm 0.009$. In einer unabhängigen Extraktion der Summe der Helizitätsverteilungen $\Delta s + \Delta\bar{s}$ von Deuteron-Daten wurde ein Wert von $\Delta s + \Delta\bar{s} = 0.129 \pm 0.042 \pm 0.129$ gemessen. (Der große systematische Fehler dieser Messung ist auf die Unsicherheiten der Kaon-Fragmentations-Funktionen zurückzuführen.)

Gegenstand dieser Dissertation ist eine neuartige "isoskalare" Messung von $\Delta s + \Delta\bar{s}$, in der diese Probleme umgangen werden. Da Strange-Quarks keinen Isospin tragen, ist der Strange-Quark-See im Proton und Deuteron gleich. Da das Deuteron ein isoskalares Target ist, kann der Fragmentationsprozess in der tiefinelastischen Streuung beschrieben werden, ohne dass Annahmen bezüglich isospinabhängiger Fragmentation notwendig sind. Zur isoskalaren Extraktion wird lediglich die Spinasymmetrie der K_s^0-Mesonen, $A_{1,d}^{K_s^0}(x, Q^2, z)$ sowie die inklusive Asymmetrie $A_{1,d}(x, Q^2)$ benötigt. Eine akkurate Messung der gesamten nicht-strange-Polarisation $\Delta Q = \Delta u + \Delta\bar{u} + \Delta d + \Delta\bar{d}$ ergibt sich direkt aus $A_{1,d}(x, Q^2)$. Die für eine Extraktion der gesamten Strange-Quark und -Antiquark-Polarisation $\Delta S = \Delta s + \Delta\bar{s}$ in führender Ordnung (leading order, LO) erforderlichen Fragmentationsfunktionen erhält man aus dem selben HERMES-Datensatz im benötigten kinematischen Bereich.

Ergebnis der hier beschriebenen Analyse ist, dass die Helizitäts-Dichteverteilungen für Strange-Quarks innerhalb des gemessenen Bereichs von $0.02 < x < 0.7$ konsistent mit Null sind: $\Delta S = 0.010 \pm 0.066 \pm 0.004$.

Abstract

The HERMES experiment at DESY, Germany was designed to carry out precision measurements of the proton spin structure using polarised deep-inelastic lepton-nucleon scattering. The experiment utilises the 27.5 GeV/c electron or positron beam of the HERA accelerator which is longitudinally polarised at HERMES, in combination with a longitudinal polarised internal gas target.

The key to understanding the origins of the spin of the nucleon is widely believed to lie in a successful description of the interactions of the quarks and gluons from which it is formed. The internal structure of the nucleon is embodied in parton distributions of the constituent quarks and gluons. The spin-averaged parton distribution functions $q(x)$ of quarks and antiquarks of flavours $q = (u, d, s)$ describe the parton momentum distributions. The differences, or helicity distributions, $\Delta q(x) = q^{\uparrow\uparrow}(x) - q^{\uparrow\downarrow}(x)$, describe the flavour dependent contributions of the constituent partons to the spin of the nucleon.

The helicity distribution of the strange quarks sea, $\Delta S(x)$, is an essential feature of the spin structure of the nucleon. Its properties reflect the reaction mechanism that is responsible for the formation of the quark sea. Much of the information on nucleon spin structure, in particular, the observation that an unexpected small fraction of the spin of the proton comes from the intrinsic quark spins is based on an analysis of inclusive deeply inelastic scattering and hyperon decay under the assumption of SU(3) symmetry among the structures of the octet baryons. In these experiments (EMC and SMC), the helicity distribution for strange quarks were directly accessible to measurement. The strange quark sea was observed to have a substantial negative polarisation. The violation of the Ellis-Jaffe sum rule observed in that analysis was attributed to this negative polarisation. To the extent that the virtual sea quarks are generated by gluon splitting, a non-zero strange quark polarisation can be attributed to a substantial polarisation of the gluons. Indeed, it has been speculated that the observed value of the strange sea helicity distribution results from a large positive gluon polarisation.

In contrast to the earlier inclusive measurements, recent data from semi-inclusive DIS at HERMES suggest that the strange sea is unpolarised. A full 5 parameter flavour decomposition using data from proton and deuteron targets, although not sensitive to the anti-strange quark spin $\Delta\bar{s}$, yielded $\Delta s = 0.028 \pm 0.033 \pm 0.009$. A separate extraction of $\Delta s + \Delta\bar{s}$ from DIS data on the deuteron alone gave $\Delta s + \Delta\bar{s} = 0.129 \pm 0.042 \pm 0.129$ where the large systematic error reflects the lack of knowledge of the kaon fragmentation functions.

This thesis reports a new "isoscalar" measurement of $\Delta s + \Delta\bar{s}$ in which these limitations are avoided. Because strange quarks carry no isospin, the strange seas in the proton and neutron are identical. In the deuteron, an isoscalar target, the fragmentation process in DIS can be described without any assumptions regarding isospin dependent fragmentation. In the isoscalar extraction of $\Delta s + \Delta\bar{s}$ only the spin asymmetry for K_s^0 $A_{1,d}^{K_s^0}(x, Q^2, z)$ and the inclusive asymmetry $A_{1,d}(x, Q^2)$ are used. An accurate measurement of the total non-strange quark polarisation $\Delta Q = \Delta u + \Delta\bar{u} + \Delta d + \Delta\bar{d}$ comes directly from $A_{1,d}(x, Q^2)$. The fragmentation functions needed for a leading order (LO) extraction of $\Delta S = \Delta s + \Delta\bar{s}$ are measured directly at HERMES kinematics using the same data.

As a result of this analysis, the helicity densities for the strange quarks are consistent with zero with the experimental uncertainty over the measured x kinematic range.

Contents

Chapter 1

Introduction

With the confirmation that the proton and neutron were not elementary particles, physicists were challenged with the task of explaining the nucleon's spin in terms of its constituents [1]. The attempt to understand the origin of the intrinsic spin of the proton and neutron has been an active area of both experimental and theoretical research for the past twenty years.

Since the 1960s it was hypothesized that the constituents of atomic nuclei (protons and neutrons) and other strongly interacting particles (collectively known as hadrons) have an internal structure. The elementary constituents of a hadron were first referred to as quarks by M. Gell-Mann [2] and G. Zweig [3].

This model described the hadron as a composite system of only three kinds of particles which Gell-Mann called "quarks" (u, d and s) and of their corresponding antiparticles. Static properties of the observed hadronic structure could be derived from the flavour, spin and charge of these quarks. Gell-Mann called this classification "The Eightfold Way", since octets of nucleons and mesons naturally appeared. The nucleons were found to belong to a supermultiplet of eight particles, i.e. an octet. For the mesons an octet was proposed where the π- and K-mesons filled seven places. And later the elementary constituents of a hadron were referred to as partons by R. Feynman [4] who introduced the parton model to explain observations in scattering experiments.

In both models the constituents of hadrons are point-like spin-1/2 particles carrying a fraction of the electric charge, and are distinguished by different flavours. But while in the constituent quark model only 3 quarks share the total mass of a nucleon (proton or neutron), the parton model predicts a nucleon to be made of a large number of partons of very small mass.

The quark and parton interpretations of the nucleus were subsequently merged together in the Quark-Parton Model (QPM). Within this framework, the process of electron-proton scattering could be expressed in terms of two structure functions, F_1 and F_2, which behave in accordance with Bjorken scaling. In 1972, measurements of the structure function F_2 of the nucleon revealed that the quarks only contribute for about 50% to the total momentum of the nucleon. [5, 6] The remaining momentum was later associated with new partons: the spin-1 gluons.

From the theoretical developments of new non-Abelian gauge field theories, Quantum Chromodynamics (QCD) [7, 8] was established as the suitable candidate to explain the interaction of quarks and gluons in terms of a strong force between color-charged particles. The missing momentum could be explained in this framework of QCD, which describes the strong interactions between the quarks in terms of the exchange of a bicolor-charged particle, namely the gluon. The missing momentum is carried by gluons which do not show up in the electro-weak scattering processes as they carry no electro-weak charge. The extension of the simple color model to QCD [9] could naturally describe the binding forces between quarks within hadrons.

The strength of the interaction is given by the strong coupling constant, which in contract to the electromagnetic coupling constant, becomes weaker with decreasing distance. This behavior explains the asymptotic freedom of quarks [7, 8].

In the asymptotic limit, i.e. when the strong coupling constant is small, QCD can be approached perturbatively and quantitative predictions can be formulated. In particular, a violation of Bjorken scaling of the structure functions is accurately predicted within QCD. It arises from the interaction between quarks by exchange of gluons. The momentum distributions of valence and sea quarks within the nucleon have been determined to a certain level of accuracy and provide further evidence for the important role of gluonic degrees of freedom.

However, the intuitive picture of the QPM can be regarded as the zeroth order approximation of perturbative QCD.

In a simple contituent picture, the total spin of the nucleon can be decomposed as

$$J_z^N = S_z^q + L_z^q + S_z^g + L_z^g = \frac{1}{2} \tag{1.1}$$

Where S_z and L_z represent the intrinsic and orbital angular momentum respectively for the quarks and the gluons. A simple non-relativistic quark model gives directly $\frac{1}{2}$ for S_z^q and 0 for all the other components.

The alternative expression is

$$\frac{1}{2} = \frac{1}{2}\Delta\Sigma + \Delta g + L_Z \tag{1.2}$$

where $\Delta\Sigma$ and Δg are the net spin contributions from the quarks and the gluons, respectively, and L_z is the contribution from the orbital angular momentum of the all partons.

In the late 1960s, the first deep-inelastic scattering experiments were carried out using high-energy electrons at the Stanford Linear Accelerator Center (SLAC) by Jerome I. Friedman, Henry W. Kendall (MIT, LNS) Richard E. Taylor (SLAC) [10]. They were repeated in the early 1970s using neutrino beams at CERN, and later still using mouns.

Starting from the late 1960s, experiments have provided evidence in support of the existence of constituents of the nucleon by exploiting the high resolution of virtual photons probing nucleon structure in deep-inelastic electron scattering. As the experimental data [10] were in agreement with the kinematic dependencies predicted by Bjorken [11] and Callan & Gross [12] on the basis of the Quark-Parton Model, first compelling evidence for the existence of quarks came available.

The investigation of the hadronic final state in deep inelastic scattering allows a deeper insight into the sub-nuclear process than the inclusive alone. One of the key propertries of QCD, the color confinement, shows up experimentally by the fact that quarks are never observed as free particles. When a quark inside a nucleon obtains a high momentum during a scattering process, it fragments into a bundle of hadrons, called a jet, when it tries to leave the color 'bag' of the nucleon. Experimentally, the momentum, the charge and the flavour of a struck quark can be measured indirectly by analysing the composition of the hadron jet. The first direct evidence for the existence of gluons was the observation of multi-jet events [13].

Electron scattering provides a powerful tool for studying the structure of the nucleus. In deep-inelastic electron scattering the interaction between an electron and a nucleon is mediated by the exchange of a virtual photon. If the virtuality of the photon (the square of its four-momentum) is high, the internal quark structure of the nucleon is probed. After absorbing the virtual photon, the quark is ejected from the nucleon with high kinetic energy. Because of the confinement property, the kinetic energy of the quark is transformed as potential energy which increases with the distance between the struck quark and the nucleon remnant. According to the string model description of this process a new quark-antiquark pair is created when the increase of potential energy is large enough, the string breaks eventually and leads to the formation of a jet of hadrons. This is the common way to describe the process of hadron formation (or string fragmentation).

Since the first SLAC-MIT experiments, the DIS process with charged lepton beams has been widely used to probe the structure of the nucleon and to enhance our understanding of QCD. With the technological development of polarised beams and targets the spin structure of the nucleon became accessible. The nucleon spin composition can be probed by studying the dependence of the cross sections on the relative orientations of the helicity of the lepton beam and the nucleon polarization in DIS. Experimentally, the determination of the ratio between the difference in the cross sections and their sum is exploited to extract an asymmetry. In fact, the systematic uncertainties in an asymmetry measurement are much more favorable than in the measurement of a cross section difference alone.

Since the late 1970s, a variety of experiment have been carried out to investigate the nucleon spin structure. The SLAC experiments E80 [14, 15] and E130 [16] measured asymmetries in DIS of polarised electrons from polarised protons. Their results confirmed the general ideas of scaling and QPM interpretation of the nucleon structure. In addition, the Ellis-Jaffe sum rule prediction for the integral of the proton spin structure was verified, though within large experimental uncertainties.

In 1987, a high precision measurement of the proton spin structure function was performed by the European Muon Collaboration (EMC) [17] with a polarised muon beam. Their result significantly deviated from the prediction of the Ellis-Jaffe sum rule. As a consequence, the EMC data imply that only 12% of the nucleon spin is carried by the quarks. This surprising result lead to the proposal of a new series of experiments which could test the validity of the EMC measurement with increased accuracy and add information on the structure functions for neutron and deuteron. Also the second generation of experiments (Spin Muon Collaboration ([17] 11) at CERN and E142 [18] and E143 [19, 20] at SLAC) confirmed the deviation from the naive parton model predictions found in the previous polarised scattering experiments.

The newly born "spin crisis" of the parton model is nowadays established rather as the "nucleon spin puzzle". In order to have a complete picture of the nucleon spin, also the spin contributions from the gluons and the orbital angular monenta in the nucleon must be taken into account.

Essentially, all the experimental information so far was gained through inclusive DIS where only the kinematics of the scattered lepton were measured. Further insight into the nucleon structure may be obtained through semi-inclusive DIS events in which a forward hadron is detected in coincidence with the scattered lepton. The detection of hadrons in the final state of a deep-inelastic scattering event (i.e. semi-inclusive deep-inelastic scattering) enables the experimental study of the fragmentation process. The identification of the particle in the hadronic final state gives a unique insight in the individual quark flavour contributions. With appropriate kinematic constraints it is possible to tag the flavour of the struck quark, allowing the separation of the contributions of the different quark flavours to the nucleon spin. In this way, semi-inclusive pion asymmetries are sensitive to the polarization of the light-sea quarks in the nucleon. Furthermore, since the K^- meson consists of only sea quarks, the K^-

asymmetry directly probes the spin content of the strange quarks in the nucleon. A direct measurement of the spin contributions of the light-sea and strange sea quarks is expecially interesting for a definitive interpretation of the nucleon spin puzzle. This thesis will be concentrated on the Δq analysis from the K_s^0 meson.

The HERMES (HERa MEasurement of Spin) experiment, together with the SLAC experiments E154 [21, 22] and E155 [23, 24], SMC [25] and compass [26], belongs to a new generation of polarised DIS experiments designed to optimize the study of the spin nuclear structure. In particular, HERMES specialized its efforts not only on precise inclusive measurements but also on the semi-inclusive physics via the measurement of semi-inclusive pion and kaon asymmetries. The experiment is located at the Deutsches Elektronen Synchrotron (DESY) laboratory in Hamburg, Germany. The longitudinally self-polarised 27.5 GeV positron beam circulating in the HERA (Hadronen Electronen Ring Anlage) storage ring interacts with a longitudinally polarised atomic gas of the HERMES target. For the experimental set-up the novel technique of an open-ended storage cell target internal to the positron beam pipe is used. In the HERMES experiment the reduction in luminosity due to the limited thickness of the gaseous target is compensated by the multiple interactions of the circulating positron beam.

The HERMES large acceptance spectrometer detects the forward going positrons and the corresponding hadronic fragments resulting from the interactions. A good hadron/positron separation is achieved by four particle identification detectors: a leadglass calorimeter combined with a preshower, a threshold Cerenkov counter and a transition radiation detector (TRD). Pion identification was possible with the threshold Cerenkov counter. Since 1998 a Ring Imaging Cerenkov detector has been in operation, allowing full hadron identification over a wide momentum range.

The spin distribution of the sea quarks can be directly accessed through the measured pion and kaon semi-inclusive asymmetries. Since the commissioning of the experiment in 1995, three different polarised targets have been used: ^{3}He (1995), hydrogen (1996-1997) and deuterium (1998-2000). In this thesis, the results obtained on deuteron target are shown.

The work presented in this thesis is organized as follows. Chapter 1, is an introduction to DIS, the HERMES experiment and the physics analysis motivation. In chapter 2, an overview is given about the theoretical framework of polarised deep-inelastic scattering. The interpretation of observables within the Quark-Parton Model and its extension to the theory of Quantum Chromodynamics is also reviewed. The HERMES experimental setup is introduced briefly in chapter 3. In chapter 4, the event selection has been discussed in detail. The related K_s^0 reconstruction and background suppression is introduced in chapter 5. The measured semi-inclusive asymmetries, which are related to the quark polarisation, are presented in chapter 6. The integral fragmentation functions, which extracted from the multiplicity of K_s^0, are given in chapter 7. Finally, the results of the strange and the non-strange quark polarisation and the quark helicity distributions are presented in chapter 8. The conclusions derived from this analysis are given in chapter 9.

Chapter 2

Polarised deep inelastic scattering

This chapter will give a brief introduction to a large and important field in particle physics, Deep Inelastic Scattering (DIS).

The idea is to accelerate electrons to very high energies, then allow them to interact with a stationary proton, and investigate what happens.

Deep inelastic scattering may be viewed in two ways: as inelastic scattering off a proton because it has constituents inside, or as elastic scattering from one of the constituents inside (ignoring the whole proton and other constituents). We are able to say that the constituents appear to be point-like and so can be considered as fundamental particles. (see section 2.3 Quark-Parton model). The DIS experiments in the late 60s paved the way for understanding the structure of the proton and neutron which was interpreted in the Quark-Parton model.

In this chapter, the formalism of polarised deep inelastic scattering is discussed. The kinematics are given in Section 2.1 for the DIS of a charged lepton from a nucleon. The polarised cross section for this process is discussed in Section 2.2 for the inclusive case. It will be shown how the measurement of polarised cross section asymmetries can be related to spin observables. The structure functions are interpreted in terms of point-like constituents of the nucleon within the framework of the Quark Parton Model (Section 2.3). Section 2.3.2 presents the sum rules for the spin structure of the nucleon by using the Operator Product Expansion formalism. Finally, in Section 2.4 the importance of the polarised semi-inclusive asymmetries is discussed. It is shown that they provide essential information on the flavour dependence of the polarised quark distributions.

2.1 Deep inelastic scattering kinematics

Deep inelastic scattering plays a key role in determining the partonic structure of the proton. If the incident lepton carries enough energy, all sorts of other stuff may come out–pions, kaons, deltas, and so on. In inclusive DIS process only the scattering lepton is detected, which is denoted as:

$$e + N \rightarrow e' + X \tag{2.1}$$

while in semi-inclusive process at least one of the final state hadrons is measured in coincidence with the lepton, that is:

$$e + N \rightarrow e' + h + X \tag{2.2}$$

The DIS process is mediated by the exchange of a virtual boson (γ^*, Z^0) between the lepton and one of the partons inside the target nucleon.

HERMES performs deep-inelastic positron-nucleon scattering experiments. At HERMES energy ($\sqrt{s} \sim 7.2 GeV$ in the center of mass), where the energy transfer ν is small compared to the Z-boson mass, the contributions due to the weak interaction can be neglected, the dominant process is one-photon exchange. Therefore only the electromagnetic interaction in the approximation of one-photon exchange is discussed at HERMES. In this case, The deep inelastic scattering can be described in lowest order, as schematically depicted in Fig. 2.1.

The corrections due to multi-photon exchange are suppressed by the smallness of the fine structure constant $\alpha_{EM} \sim 1/137$. Since the interference between one- and two-photon exchange is sensitive to the charge of the lepton beam. The contributions from multi-photon exchange processes can be extracted by comparing the results from DIS experiments which use oppositely charged leptons. There is no experimental evidence for the DIS cross section ratio $\sigma_{e^+}/\sigma_{e^-}$ at HERMES energies, thus it can be negligible. Moreover only the three light quark flavours up (u), down (d) and strange (s) are of relevance at this energy.

The relevant kinematic variables are denoted as the four-momenta of the incoming positron $\mathbf{k} = (E, \overrightarrow{k})$ and scattered positron $\mathbf{k}' = (E', \overrightarrow{k'})$, $\mathbf{q} = (\mu, \overrightarrow{q})$, $\mathbf{p} = (E_p, \overrightarrow{p})$, and $\mathbf{p}_h = (E_h, \overrightarrow{p_h})$ as those of the exchanged virtual photon, the target nucleon, and a hadron produced in the scattering process. The following Lorentz invariants are defined in the standard way as [27]:

$$Q^2 \equiv -q^2 = -(\mathbf{k} - \mathbf{k}')^2, \quad \text{squared four–momentum transfer,} \tag{2.3}$$

$$s = (\mathbf{p} + \mathbf{k})^2, \quad \text{squared center–of–mass energy,} \tag{2.4}$$

$$W^2 = (\mathbf{p} + \mathbf{q})^2, \quad \text{squared invariant mass of the photon–nucleon system.} \tag{2.5}$$

As a fixed target experiment, $\mathbf{p} = (M, 0)$, HERMES also neglect the thermal motion of the target atoms and the Fermi motion of the nucleons. The laboratory frame coincides with the nucleon rest frame. In addition, since the energies of incident and scattered leptons are large compared to their mass, the lepton mass may also be

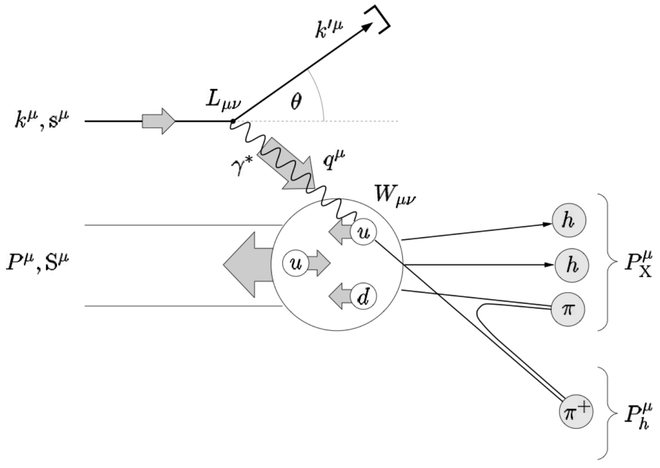

Figure 2.1: Diagram of the deep-inelastic lepton-nucleon scattering in the one-photon exchange approximation as seen in the laboratory system. The shaded arrows indicate the spins of the particles.

neglected. These approximations are used in the derivation of the DIS kinematic quantities listed in Tab. 2.1. Therefore, in the nucleon rest system:

$$Q^2 \overset{Lab}{\simeq} 4EE'\sin^2(\theta/2) = 2EE'(1-\cos\theta) \tag{2.6}$$

$$s \overset{Lab}{=} M^2 + 2ME \tag{2.7}$$

$$\nu \overset{Lab}{=} E - E' \tag{2.8}$$

$$W^2 \overset{Lab}{=} M^2 + 2M\nu - Q^2 \tag{2.9}$$

Where θ is the electron scattering angle in the laboratory system, M is the mass of the proton. and ν is the energy of the virtual photon transfered from the electron to the nucleon. The dimensionless scaling variables x and y are defined as:

$$x = \frac{Q^2}{2\mathbf{p}\cdot\mathbf{q}} \overset{Lab}{=} \frac{Q^2}{2M\nu}, \tag{2.10}$$

$$y = \frac{\mathbf{p}\cdot\mathbf{q}}{\mathbf{p}\cdot\mathbf{k}} \overset{Lab}{=} \frac{\nu}{E}. \tag{2.11}$$

x is the Bjørken scaling variable. For the elastic scattering, $W^2 = M^2$, and consequently $x = 1$, while for the inelastic process, $W^2 > M^2$ and $x < 1$. The variable x can also be interpreted as the fraction of the nucleon's light–cone momentum carried by the struck quark. y is the fractional energy–transfer from the electron to the nucleon. In general the kinematically allowed ranges are $0 \leq x \leq 1$ and $0 \leq y \leq 1$.

In the case of semi-inclusive measurements, the kinematics of the final state hadron are described by its fractional energy z with respect to the energy transfer ν in the laboratory frame.

$$z = \frac{\mathbf{p}\cdot\mathbf{p}_h}{\mathbf{p}\cdot\mathbf{q}} \overset{Lab}{=} \frac{E_h}{v} \tag{2.12}$$

and the Feynman variable x_F,

$$x_F = \frac{P^*_{||}}{|\overrightarrow{q}|} \simeq \frac{2P^*_{||}}{W} \tag{2.13}$$

Experimental Observables	
Lepton:	
$k^\mu \ = \ (E, \vec{k})$	Four-momentum of the incodent lepton
$k'^\mu \ = \ (E', \vec{k}')$	Four-momentum of the scattered lepton
(θ, ϕ)	Polar and azimuthal angles of the scattered lepton
Hadron:	
$P^\mu \overset{Lab}{=} (M, \vec{0})$	Four-momentum of the target nucleon
$P_h^\mu \overset{Lab}{=} (E_h, \vec{P}_h)$	Four-momentum of a detected final state hadron h
Derived Quantities	
Inclusive DIS:	
$q^\mu = k^\mu - k'^\mu = (\nu, \vec{q})$	Four-momentum of the virtual photon
$\vec{q} = \vec{k} - \vec{k}'$	Three-momentum of the virtual photon in the lab. frame
$\nu = \frac{P_\mu q^\mu}{M} \overset{Lab}{=} E - E'$	Energy of the virtual photon in the lab. frame
$Q^2 = -q_\mu q^\mu$ $\overset{Lab}{\simeq} 4EE'\sin^2(\theta/2)$	Squared invariant mass of the virtual photon
$W^2 = (P^\mu + q^\mu)^2$ $\overset{Lab}{=} M^2 + 2M\nu - Q^2$	Squared invariant mass of the final hadronic system
$x = Q^2/(2P_\mu q^\mu)$ $\overset{Lab}{=} Q^2/(2M\nu)$	Bjorken scaling variable
$y = P_\mu q^\mu / P_\mu k^\mu \overset{Lab}{=} \nu/E$	Fractional energy transfer of the photon
$s = (P^\mu + k^\mu)^2$ $\overset{Lab}{=} 2ME + M^2 + m_l^2$	Squared centre of mass energy
Semi-inclusive DIS:	
$P^*_{\vert\vert} = \vec{P}_h \cdot \frac{\vec{q}}{\vert\vec{q}\vert}$	Longitudinal momentum of a hadron h in the $\gamma^* - N$ centre of mass system
$x_F = \frac{P^*_{\vert\vert}}{\vert\vec{q}\vert} \backsimeq \frac{2P^*_{\vert\vert}}{W}$	Feynman scaling variable
$z = \frac{P_\mu P_h^\mu}{P_\mu q^\mu} \overset{Lab}{=} E_h/\nu$	Fractional energy of the photon carried by the hadron h

Table 2.1: A legend of kinematic quantities used in the description of deep inelastic positron nucleon scattering.

where $P_{||}^{*}$ is the hadron's longitudinal momentum with respect to the photon momentum in the virtual photon-nucleon center-of-mass system. The kinematically allowed ranges for the variables z and x_F are $0 < z < 1$ and $-1 < x_F < 1$ respectively. The hadron that contains the struck quark carries a large energy fraction z and has positive x-Feynmann, as it travels in the forward direction with respect to the photon. Hadrons that contain the struck quark or that are part of the "jet" that contains the struck quark are called the current fragments, where as hadrons in the final state that are formed from the spectator quarks are the target fragments.

2.2 Inclusive deep inelastic scattering

In lowest-order perturbation theory, for one photon exchange, the differential deep-inelastic cross section for detection the scattering lepton in a solid angle dΩ and in an energy range $[E', E' + dE']$ can be written in term of leptonic and hardronic tensors, $L_{\mu\nu}$ and $W^{\mu\nu}$, which describe the structure of the leptonic and hardronic vertices [28, 29, 30, 31, 32, 33]

$$\frac{\mathrm{d}^2\sigma}{\mathrm{d}\Omega \mathrm{d}E'} = \frac{\alpha^2}{Q^4}\frac{E'}{E} L_{\mu\nu} W^{\mu\nu} \tag{2.14}$$

Where α denotes the electromagnetic coupling constant (The fine-structure constant), and $L_{\mu\nu}$ and $W_{\mu\nu}$ are the lepton and hadron tensors, respectively. As the electromagnetic interaction conserves parity, only terms with like symmetry contribute to the DIS cross section in Eq. 2.14. Due to the pointlike nature of the positrons, the lepton tensor $L_{\mu\nu}$ can be calculated in QED from

$$L_{\mu\nu}(k, s; k', s') = [\bar{u}'(k', s')\gamma_\mu u(k, s)] * [\bar{u}'(k', s')\gamma_\nu u(k, s)] \tag{2.15}$$

where $u(k, s), u'(k', s')$ are the Dirac spinors for spin-$\frac{1}{2}$ particles with four-momentum $k[k']$ and spin four-vector $s[s']$, describing the incident [scattered] positron. Due to that the polarisation is not observed in the experiment, summing over the spin four-vector s' of the scattered positron, the lepton and hadron tensors can be split into two parts, which are symmetric tensors $L_{\mu\nu}^{(S)}$ $W_{\mu\nu}^{(S)}$ and anti-symmetric tensors $L_{\mu\nu}^{(A)}$ $W_{\mu\nu}^{(A)}$ under parity transformations:

$$L_{\mu\nu} = L_{\mu\nu}^{(S)} + L_{\mu\nu}^{(A)} \tag{2.16}$$

$$W_{\mu\nu} = W_{\mu\nu}^{(S)} + W_{\mu\nu}^{(A)} \tag{2.17}$$

where $L_{\mu\nu}^{(S)}(k,k')$ and $L_{\mu\nu}^{(A)}(k,s,k')$ are defined as:

$$L_{\mu\nu}^{(S)}(k,k') = 2[k_\mu k_\nu{}' + k_\mu{}' k_\nu - g_{\mu\nu}(k \cdot k' - m_e^2)] \tag{2.18}$$

$$L_{\mu\nu}^{(A)}(k,s,k') = 2m_e \epsilon_{\mu\nu\lambda\sigma} s^\lambda (k-k')^\sigma \tag{2.19}$$

The anti-symmetric part depends on the spin s^λ of the incident positron, while the symmetric part is spin-independent. In the above expressions, $g_{\mu\nu}$ is the metric tensor, m_e denotes the positron mass, and $\epsilon_{\mu\nu\lambda\sigma}$ is the totally anti-symmetric Levi-Civita tensor of rank four.

The unknown hadronic tensor $W_{\mu\nu}$, which contains the strong interaction dynamics, can be written in terms of four scalar inelastic form factors, $W_{1,2}$ and $G_{1,2}$, functions at most of q^2 and $p \cdot q$ [34].

$$W_{\mu\nu}^{(S)} = \left(-g_{\mu\nu} + \frac{q_\mu q_\nu}{q^2}\right) W_1 + \left(p_\mu - \frac{p \cdot q}{q^2} q_\mu\right) \left(p_\nu - \frac{p \cdot q}{q^2} q_\nu\right) \frac{W_2}{M^2} \tag{2.20}$$

$$W_{\mu\nu}^{(A)} = \epsilon_{\mu\nu\alpha\beta} q^\alpha \left\{ M S^\beta G_1 + \left[(p \cdot q) S^\beta - (S \cdot q) p^\beta\right] \frac{G_2}{M} \right\} \tag{2.21}$$

In contrast to the lepton tensor, the hadron tensor $W_{\mu\nu}$ which describes the interaction at the virtual photon-nucleon vertex is unknown. It represents the internal structure of the nucleon, whose understanding in a specific aspect is the aim of this thesis. The internal nucleon structure, and hence the hadronic tensor, can be parameterized by a set of structure functions, which will be discussed in the following two sections.

2.2.1 The unpolarised cross section and structure functions

The usual unpolarised cross section is proportional to $L^{(S)}_{\mu\nu} W^{\mu\nu(S)}$.

$$\begin{aligned}\frac{\mathrm{d}^2\sigma^{\mathrm{unpol}}}{\mathrm{d}\Omega\mathrm{d}E'} &= \frac{1}{4}\sum_{s,s',S}\frac{\mathrm{d}^2\sigma}{\mathrm{d}\Omega\mathrm{d}E'}(k,s,P,S;k',s') \\ &= \frac{\alpha^2}{Q^4}\frac{E'}{E}L^{(S)}_{\mu\nu}W^{\mu\nu(S)} \qquad (2.22)\end{aligned}$$

Inserting Eqs. 2.18 and 2.20 in 2.22, then the well-known unpolarised cross section expression can be obtained with neglecting the lepton mass in the laboratory frame:

$$\frac{\mathrm{d}^2\sigma^{\mathrm{unpol}}}{\mathrm{d}\Omega\mathrm{d}E'} = \frac{4\alpha^2 E'}{Q^4}\left[2W_1(\nu,Q^2)\mathrm{sin}^2\frac{\theta}{2} + W_2(\nu,Q^2)\mathrm{cos}^2\frac{\theta}{2}\right] \qquad (2.23)$$

Where θ is the scattering angle of lepton, W_1 and W_2 are unpolarised structure functions. In the Bjørken limit, or DIS regime, (i.e. $Q^2 \to \infty$ and $\nu \to \infty$), $x = \frac{Q^2}{2P\cdot q} = \frac{Q^2}{2M\nu}$ is fixed. Introducing the dimensionless structure functions $F_1(x,Q^2)$ and $F_2(x,Q^2)$,

$$\begin{aligned}F_1(x,Q^2) &= MW_1(Q^2,\nu) \qquad (2.24)\\ F_2(x,Q^2) &= \nu W_2(Q^2,\nu) \qquad (2.25)\end{aligned}$$

which vary very slowly with Q^2 at fixed x. The unpolarised cross section becomes

$$\frac{\mathrm{d}^2\sigma^{\mathrm{unpol}}}{\mathrm{d}x\mathrm{d}Q^2} = \frac{4\pi\alpha^2}{Q^4}\cdot\left[F_1(x,Q^2)\cdot y^2 + \frac{F_2(x,Q^2)}{x}\cdot\left(1-y-\frac{Mxy}{2E}\right)\right] \qquad (2.26)$$

Precise measurements of the proton and deuterium structure functions F_2^{p} and F_2^{d} have been performed by numerous fixed target (BCDMS [35], E665 [36], NMC [37], SLAC [38]) and collider experiments (H1 [39] and ZEUS [40]), covering a broad kinematic range of $0.000063 \leq x \leq 0.85$, and $0.1 \leq (Q^2/\mathrm{GeV}^2) \leq 5\cdot 10^3$. In Fig. 2.2 a compilation of world data on the proton structure function F_2^{p} in the kinematic range relevant to HERMES is shown. For values of $x \leq 0.18$ and $x \geq 0.3$ the structure function shows a significant dependence on Q^2, which is not expected from the naive quark model. This Q^2-dependence is a consequence of QCD effects.

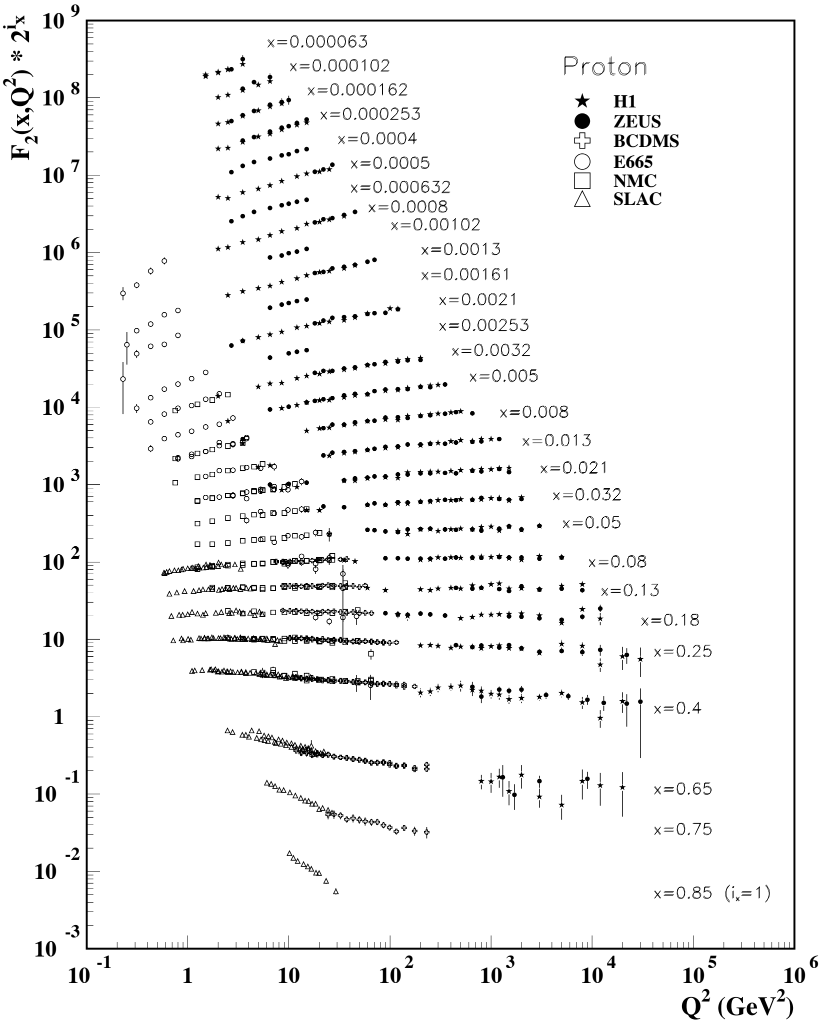

Figure 2.2: The unpolarised proton structure function $F_2^p(x, Q^2)$ measured in electromagnetic scattering of positrons on protons (collider experiments ZEUS and H1), in the kinematic domain of the HERA data, for $x > 0.00006$, and for electrons (SLAC) and mouns (BCDMS, E665, NMC) on a fixed target. The statistical and systematic errors added in quadrature are shown. For the better representation, F_2^p has been multiplied by 2^{i_x}, where i_x is the number of the x bin. [41].

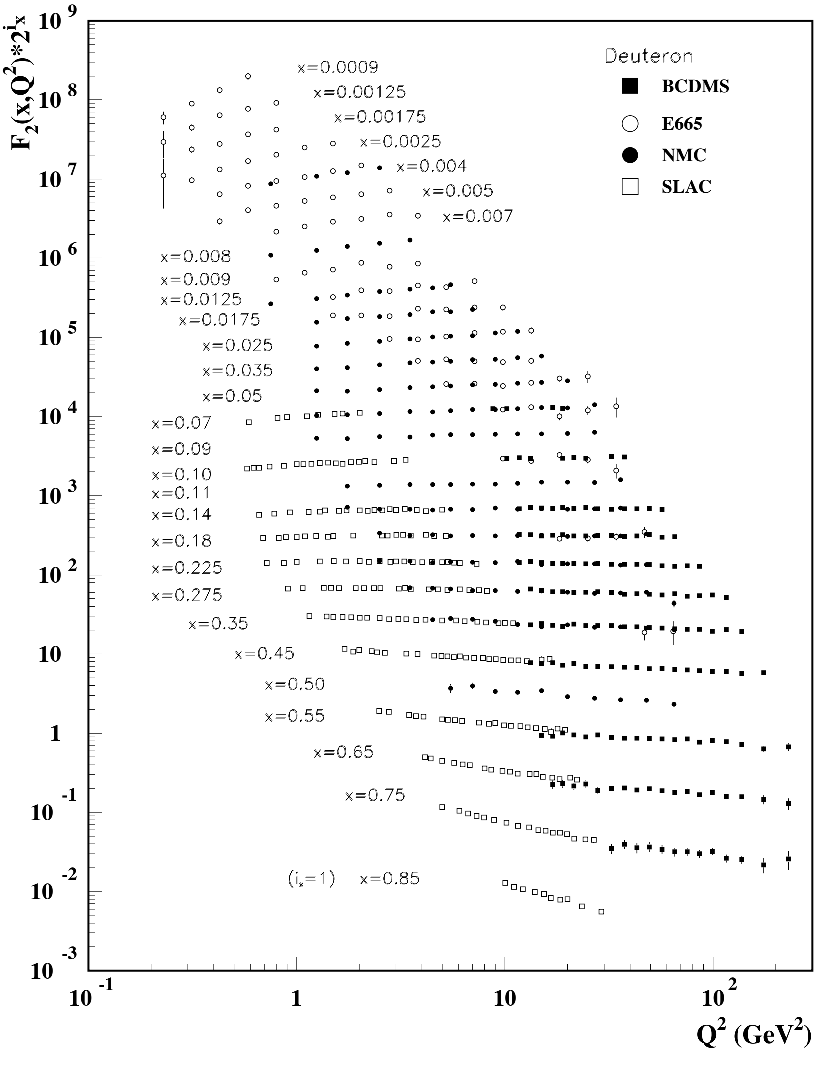

Figure 2.3: The unpolarised deuteron structure function $F_2^d(x, Q^2)$ measured in electromagnetic scattering of electrons (SLAC) and mouns (BCDMS, E665, NMC) on a fixed target. The statistical and systematic errors added in quadrature are shown. For the better representation, F_2^d has been multiplied by 2^{i_x}, where i_x is the number of the x bin. [41].

Photon absorption cross section

The unpolarised cross section can alternatively be expressed in terms of the transversely photon absorption cross section σ_T and the longitudinally polarised virtual photon absorption cross section σ_L on a nucleon:

$$\frac{\mathrm{d}^2\sigma^{\mathrm{unpol}}}{\mathrm{d}x\mathrm{d}Q^2} = \Gamma\left[\sigma_T(x,Q^2) + \epsilon\sigma_L(x,Q^2)\right] \tag{2.27}$$

Where, Γ gives the flux of virtual photons, which originate from the lepton beam. And ϵ is the degree of longitudinal polarisation of the virtual photon. Neglecting the positron rest mass m_e, ϵ is given by

$$\epsilon \overset{Q^2>>2m_e^2}{\simeq} \frac{1-y-\frac{1}{4}\gamma^2y^2}{1-y-\frac{1}{4}y^2(\gamma^2+2)} \tag{2.28}$$

$$\text{with} \quad \gamma^2 = \frac{Q^2}{\nu^2} = \frac{4M^2x^2}{Q^2} \tag{2.29}$$

Introducing the ratio $R(x,Q^2)$ of the photo absorption cross sections

$$R(x,Q^2) = \frac{\sigma_L(x,Q^2)}{\sigma_T(x,Q^2)} \tag{2.30}$$

the structure functions $F_1(x,Q^2)$ and $F_2(x,Q^2)$ can be related to each other by the longitudinal structure function $F_L(x,Q^2)$

$$R(x,Q^2) = \frac{F_L(x,Q^2)}{2xF_1(x,Q^2)} = \frac{(1+\gamma^2)F_2(x,Q^2) - 2xF_1(x,Q^2)}{2xF_1(x,Q^2)} \tag{2.31}$$

or

$$F_1(x,Q^2) = F_2(x,Q^2)\cdot\frac{1+\gamma^2}{2x[1+R(x,Q^2)]} \tag{2.32}$$

The cross section ratio $R(x,Q^2)$ has been measured by several DIS experiments in the HERMES kinematic range and found to be identical for proton and neutron targets within the experimental uncertainties. The available data and a parameterization of R [42] are shown in Fig. 2.4, which is used in extracting the photon-nucleon asymmetries in the analysis in this thesis.

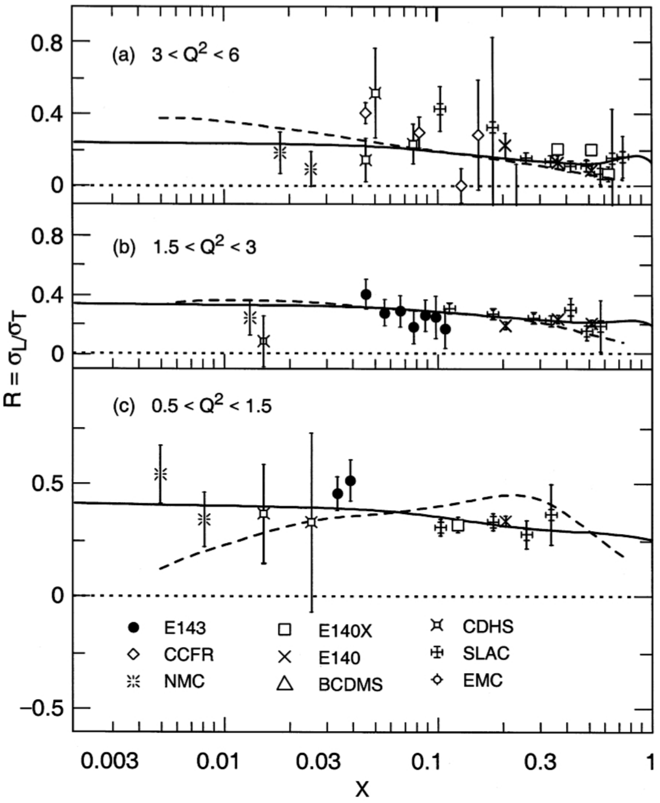

Figure 2.4: The Ratio of longitudinal and transverse cross sections $R = \sigma_L/\sigma_T$ as a function of x in three ranges of Q^2. The solid line shows the parameterization R1998 [42]. Also shown are measurements from various experiments. The dashed lines show the results of a next-to-next-to-leading order calculation in perturbative QCD. The figure is reported in Ref. [42].

In the Bjørken limit (i.e. $Q^2 \to \infty$ and $\nu \to \infty$), $x = Q^2/2M\nu$ remains constant, for longitudinally polarised photons, the photo absorption cross section σ_L vanishes as a consequence of the requirement of helicity conservation at the virtual photon-quark scattering vertex.

In the limit, $R \to 0$, Eq. 2.32 gives the Callan-Gross relation [12]:

$$2xF_1(x) = F_2(x) \tag{2.33}$$

2.2.2 The polarised cross section differences, structure functions and asymmetries

The differences of cross sections with opposite target spins are proportional to $L_{\mu\nu}^{(A)} W^{\mu\nu(A)}$.

$$\sum_{s'} \left[\frac{\mathrm{d}^2\sigma}{\mathrm{d}\Omega \mathrm{d}E'}(k, s, P, -S; k', s') - \frac{\mathrm{d}^2\sigma}{\mathrm{d}\Omega \mathrm{d}E'}(k, s, P, S; k', s') \right]$$
$$= \frac{\alpha^2}{Q^4} \frac{E'}{E} 2L_{\mu\nu}^{(A)} W^{\mu\nu(A)} \tag{2.34}$$

In the target frame, using the definitions of scattering angles in Fig. 2.5 the cross section difference can be expressed as:

$$\begin{aligned} \frac{\mathrm{d}^2\sigma(-S)}{\mathrm{d}\Omega \mathrm{d}E'} - \frac{\mathrm{d}^2\sigma(+S)}{\mathrm{d}\Omega \mathrm{d}E'} &= \frac{4\alpha^2 E'}{Q^2 E} \\ &\times \{[E\cos\alpha + E'(\sin\theta \sin\alpha \cos\phi + \cos\theta\cos\alpha)]MG_1 \\ &+ 2EE'(\sin\theta\sin\alpha\cos\phi + \cos\theta\cos\alpha - \cos\alpha)G_2\} \end{aligned} \tag{2.35}$$

In particular, when the target nucleon is longitudinally polarised (that is the polarised along the incoming lepton direction, $\alpha = 0$), and the differences of cross section becomes

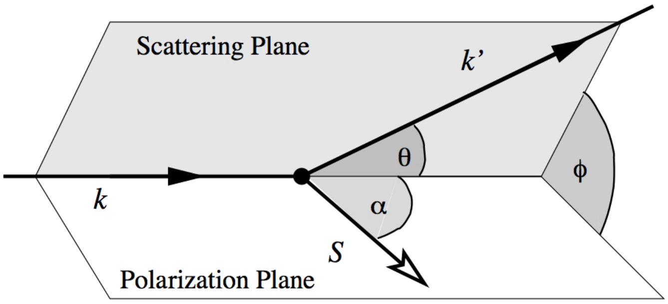

Figure 2.5: Definition of the angles in polarised inclusive deep inelastic scattering in the laboratory system.

$$\frac{\mathrm{d}^2\sigma^{\overset{\rightarrow}{\Leftarrow}}}{\mathrm{d}\Omega\mathrm{d}E'} - \frac{\mathrm{d}^2\sigma^{\overset{\rightarrow}{\Rightarrow}}}{\mathrm{d}\Omega\mathrm{d}E'} = \frac{4\alpha^2 E'}{Q^2 E}[(E + E'\cos\phi)MG_1 - Q^2 G_2] \tag{2.36}$$

When the target nucleon is transversely polarised (that is, polarised orthogonally to the incoming lepton direction, $\alpha = \pi/2$), and the differences of cross section becomes

$$\frac{\mathrm{d}^2\sigma^{\rightarrow\Downarrow}}{\mathrm{d}\Omega\mathrm{d}E'} - \frac{\mathrm{d}^2\sigma^{\rightarrow\Uparrow}}{\mathrm{d}\Omega\mathrm{d}E'} = \frac{4\alpha^2 E'}{Q^2 E}\sin\theta[MG_1 + 2EG_2] \tag{2.37}$$

Where G_1 and G_2 are the polarised structure functions. In the Bjørken limit, (i.e. $Q^2 \rightarrow \infty$ and $\nu \rightarrow \infty$), they are expected to scale approximately:

$$g_1(x, Q^2) = M^2\nu G_1(\nu, Q^2) \tag{2.38}$$

$$g_2(x, Q^2) = M\nu^2 G_2(\nu, Q^2) \tag{2.39}$$

Here, → indicates the spin orientation of the incoming lepton and $\Leftarrow, \Rightarrow$ denote the different spin states of the target nucleon. The cross section is dominated by the structure function $g_1(x, Q^2)$, since $g_2(x, Q^2)$ is suppressed by $\gamma^2 \sim 1/Q^2$ and $g_2(x, Q^2)$ is small quantity and even is neglected in the simple quark parton model. The contribution of $g_2(x, Q^2)$ vanishes completely in case of a target polarised longitudinally with respect to the virtual photon. Experimentally, however, a polarisation with respect to the virtual photon is not achievable. Figure 2.6 shows measurements on longitudinally polarised proton and deuteron targets of different experiments.

The structure function $g_2(x, Q^2)$ is usually taken into account by a parametrization of world data. The precision of the parametrization has only a marginal effect on the $g_1(x, Q^2)$ measurement and is part of the systematic uncertainty. The neutron structure function is extracted from the difference of the results for the deuteron and the proton. It can be measured also directly with a polarised ^{3}He target, which is an effective polarised neutron target due to the almost complete cancellation of the proton spins (see e.g. [49]).

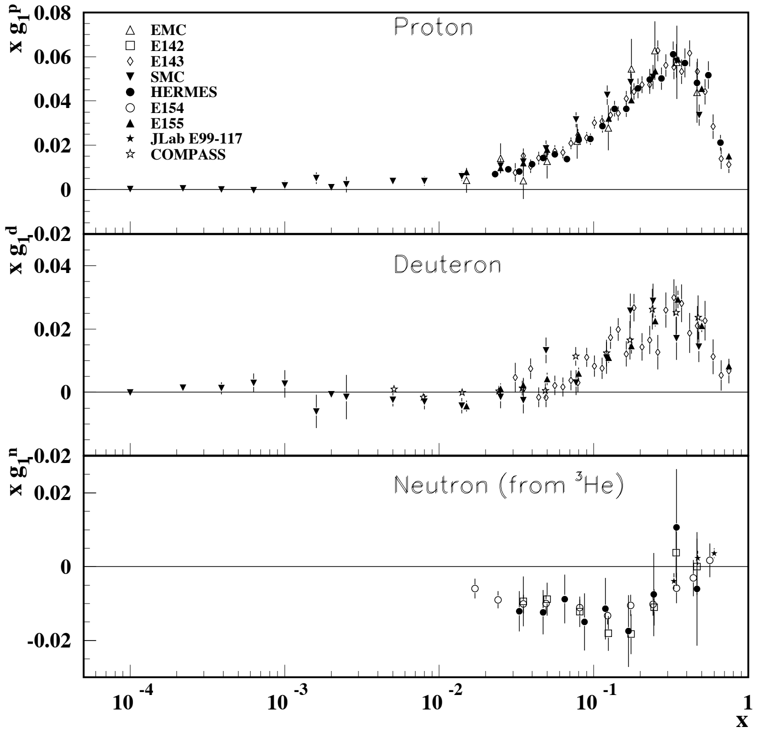

Figure 2.6: The spin-dependent structure function $xg_1(x)$ of the proton, deuteron, and neutron (from ^{3}He target) measured as function of x in deep inelastic scattering of polarised electrons/positrons. (EMC: [43], E142: [44], E143: [45], SMC: [46], HERMES: [47], E155: [23, 48],). Statistical and systematic uncertainties added in quadrature are shown.

Double spin asymmetries

In principle, the spin-dependent structure functions g_1 and g_2 can be determined by measuring the cross section differences for a longitudinally ($\alpha = 0, \pi$) and a transversely ($\alpha = \frac{\pi}{2}, \frac{3\pi}{2}$) polarised target. Rather than measuring cross section differences, it is advantageous from an experimental point of view to measure the following cross section asymmetries:

$$A_{||}(x, Q^2) = \frac{\sigma^{\overset{\rightarrow}{\Leftarrow}} - \sigma^{\overset{\rightarrow}{\Rightarrow}}}{\sigma^{\overset{\rightarrow}{\Leftarrow}} + \sigma^{\overset{\rightarrow}{\Rightarrow}}}, \qquad A_{\perp}(x, Q^2) = \frac{\sigma^{\rightarrow\Downarrow} - \sigma^{\rightarrow\Uparrow}}{\sigma^{\rightarrow\Downarrow} + \sigma^{\rightarrow\Uparrow}} \tag{2.40}$$

Here, $\sigma^{\overset{\rightarrow}{\Leftarrow}(\overset{\rightarrow}{\Rightarrow})}$ is a short notation for the differential cross sections $\dfrac{\mathrm{d}^2\sigma^{\overset{\rightarrow}{\Leftarrow}(\overset{\rightarrow}{\Rightarrow})}}{\mathrm{d}x\mathrm{d}Q^2}$ for parallel (anti-parallel) alignments of beam and target spin, which have been introduced in the previous section. The $\sigma^{\rightarrow\Uparrow(\rightarrow\Downarrow)}$ are defined accordingly. Provided the time intervals between the flipping of the target or beam spin are short enough, efficiency and acceptance effects, which are not correlated to the relative orientation of the beam and target spins, cancel out by measuring cross section asymmetries instead of cross section differences. Hence, asymmetry measurements are less susceptible to systematic effects than measurements of differences of absolute cross sections.

Photon absorption cross section

In the virtual photon-nucleon reference frame, the cross section differences can be expressed in terms of the two asymmetries A_1 and A_2:

$$A_1(x,Q^2) = A_1 = \frac{\sigma_{\frac{1}{2}} - \sigma_{\frac{3}{2}}}{\sigma_{\frac{1}{2}} + \sigma_{\frac{3}{2}}} = \frac{g_1 - \gamma^2 g_2}{F_1} \tag{2.41}$$

$$A_2(x,Q^2) = A_2 = \frac{2\sigma_I}{\sigma_{\frac{1}{2}} + \sigma_{\frac{3}{2}}} = \frac{\gamma(g_1 + g_2)}{F_1} \tag{2.42}$$

where the dependence of the structure functions and cross sections on the kinematical quantities x and Q^2 has been omitted for clarity. In these definitions, $\sigma_{\frac{1}{2}}(\sigma_{\frac{3}{2}})$ denotes the cross section for the absorption of a virtual photon by the nucleon, when the projection of the total angular momentum of the virtual photon-nucleon system along the momentum of the photon is $\frac{1}{2}(\frac{3}{2})$. $\sigma_T = \frac{1}{2}(\sigma_{\frac{1}{2}} + \sigma_{\frac{3}{2}})$ is the total transverse photo absorption cross section, while σ_I arises from the interference of longitudinal and transverse photo absorption amplitudes. Like in the above definitions for $A_{||}$ and $A_{\perp}$, the $\sigma_j, (j = I, L, T)$ are short notations for the corresponding differential cross sections with respect to x and Q^2. The interference cross section term has to obey the triangular relation $\sigma_I \leq \sqrt{\sigma_L \sigma_T}$, thus leading to a positivity limit for the absolute value of the asymmetry A_2:

$$|A_2| = |\frac{\sigma_I}{\sigma_T}| \leq \sqrt{\frac{\sigma_L \sigma_T}{\sigma_T^2}} = \sqrt{R(x,Q^2)} \tag{2.43}$$

which is given by the square root of the cross section ratio R introduced in Sect. 2.2.2. The virtual photon asymmetries A_1 and A_2 are related to the experimental asymmetries $A_{||}$ and $A_{\perp}$ by

$$A_{||} = D(A_1 + \eta A_2), \qquad A_{\perp} = D(\xi A_2 - \frac{\eta}{\xi} A_1) \tag{2.44}$$

$D = D(x, Q^2)$ is the depolarisation factor of the virtual photon, which depends on the kinematical quantities and the cross section ratio R, while η and ξ are purely kinematical factors:

$$D = \frac{1-(1-y)\varepsilon}{1+\varepsilon R} \tag{2.45}$$

$$\eta = \frac{\varepsilon\gamma y}{1-(1-y)\varepsilon} \tag{2.46}$$

$$\xi = \sqrt{\frac{2\varepsilon}{1+\varepsilon}} \tag{2.47}$$

and ϵ is the degree of longitudinal polarisation of the virtual photon, already defined in Eq. (2.28).

Rewriting Eq. 2.41 and using the definition in Eq. 2.44, the virtual photon asymmetry A_1 can be expressed as

$$A_1 = \frac{A_{||}}{D(1+\eta\gamma)} - \frac{\eta\gamma(1+\gamma^2)}{1+\eta\gamma}\frac{g_2}{F_1} \overset{g_2=0}{\simeq} \frac{A_{||}}{D(1+\eta\gamma)} \tag{2.48}$$

This allows to approximately extract the virtual photon asymmetry A_1 from a measurement of the longitudinal asymmetry $A_{||}$ alone, under the assumption that the polarised structure function g_2 vanishes. The contribution from g_2 in Eq. 2.48 is additionally suppressed by the kinematic factors γ^2 and $\eta\gamma$, which in the HERMES kinematic domain are small ($0.003 < \gamma^2 < 0.15$ and $0.001 < \eta\gamma < 0.15$). The uncertainty arising from neglecting g_2 is considered in the calculation of the systematic uncertainties on the extracted values of the virtual photon asymmetry A_1 in Sect. 6.4.

2.3 Quark Parton Model

The Quark-Parton Model (QPM) is a simple model (and a very useful tool), which was developed by Bjørken and Paschos [50], and Feynman [51] in order to give an interpretation of deep inelastic scattering and its scale invariance. The structure functions describe the internal composition of the target nucleon and are approximately independent of the variable Q^2, (i.e. scaling behaviour). The observation of Bjørken scaling at SLAC provide experimental verification of Feynman's parton model [4]. As Q^2 defines the resolution of the scattering process, the independence of Q^2 has to be interpreted in the way that the internal structure of the components is point-like or at least much smaller than the resolution of the process. In the QPM, deep inelastic lepton-nucleon scattering is interpreted as elastic scattering of lepton from pointlike particles in the nucleon with spin-$\frac{1}{2}$ and charge $e_q \neq 0$: the partons. Later the partons were identified with the quarks proposed by Gell-Mann [2] and Zweig [52] to describe the hadronic spectra. In the framework of QCD, partons behave approximately like free particles due to the asymptotic freedom of QCD.

2.3.1 The naive QPM, structure functions and quark distribution

Elastic quark scattering

The deep inelastic scattering process is actually the incoherent superposition of elastic scattering off partons, from the elastic scattering kinematics, the following conditions can be derived:

$$Q^2 = 2m_q\nu \tag{2.49}$$

$$x = \frac{Q^2}{2M\nu} = \frac{m_q}{M} \tag{2.50}$$

where m_q is an apparent mass of the parton in the scattering process. The picture of the infinite momentum frame is used to illustrate the meaning of the Bjøken variable x in an intuitive way. The parton carries the fraction $p_q = xp$ of the momentum p of the nucleon. Momentum distributions $q_f(x)$ are assigned in the quark model which describe the probability to find a quark of flavour f with momentum fraction x inside the nucleon.

The cross section for the scattering off quarks can be directly calculated from the probability distribution $q_f(x)$. The hadronic tenser $W_{\mu\nu}$ becomes similar to the leptonic tenser in formula (2.18,2.19) where k and k' are replace by xp and p' and the 'charge density' $e_f^2 q_f(x)$ and a phase space factor is added to the formula:

$$W_{\mu\nu} = \frac{e_f^2 q_f(x)}{2Mxp \cdot q}[xp_\mu xp'_\nu + xp_\nu xp'_\mu - g_{\mu\nu} xp \cdot p' + ih\epsilon_{\mu\nu\alpha\beta} q^\alpha xp^\beta] \tag{2.51}$$

Here, h is the helicity of the quark. With the relation $p' = xp + q$ and after omitting the p^μ and p^ν terms (they disapper in the contraction with $W_{\mu\nu}$ due to current conservation) the equation becomes:

$$W_{\mu\nu} = \frac{e_f^2 q_f(x)}{2Mxp \cdot q}[2xp_\mu xp_\nu - g_{\mu\nu} xp \cdot q + ih\epsilon_{\mu\nu\alpha\beta} q^\alpha xp^\beta] \tag{2.52}$$

This formula has to compared with the parameterisation of $W_{\mu\nu}$ in terms of structure functions. The following formula is deduced from equations (2.20, 2.21) by omitting q_μ, q_ν terms (they desappear when $W_{\mu\nu}$ is contracted with $L^{\mu\nu}$). The expression for $W_{\mu\nu}$ becomes:

$$\begin{aligned} W_{\mu\nu} &= -\frac{F_1(Q^2,\nu)}{M} g_{\mu\nu} \\ &+ \frac{F_2(Q^2,\nu)}{Mp \cdot q} p_\mu p_\nu \\ &+ \frac{ig_1(Q^2,\nu)}{M\nu} \epsilon_{\mu\nu\lambda\sigma} q^\lambda s_h^\sigma \\ &+ \frac{ig_1(Q^2,\nu)}{M^2\nu^2} \epsilon_{\mu\nu\lambda\sigma} q^\lambda (p \cdot q s_h^\sigma - s_h \cdot q p^\sigma) \end{aligned} \tag{2.53}$$

In the quark-parton model, with the notation that $q_f^{+(-)}$ is the probability to find a quark of momentum fraction x with the helicity parallel (anti-parallel) to the nucleon spin. The structure functions are related to the quark distributions:

$$F_1(x,Q^2) = \sum_f \frac{e_f^2}{2}(q_f^+(x) + q_f^-(x)) \tag{2.54}$$

$$F_2(x,Q^2) = \sum_f e_f^2 x(q_f^+(x) + q_f^-(x)) \tag{2.55}$$

$$g_1(x,Q^2) = \sum_f \frac{e_f^2}{2}(q_f^+(x) - q_f^-(x)) \tag{2.56}$$

$$g_2(x,Q^2) = 0 \tag{2.57}$$

where the sum is over all quark and antiquark flavours (u, d, s, c, b, t and $\bar{u}$, $\bar{d}$, $\bar{s}$, $\bar{c}$, $\bar{b}$, $\bar{t}$) which contribute to the structure of the nucleon at a given momentum transfer.

The unpolarised quark distributions

In the simple parton model, all structure functions are independent of Q^2. The structure functions $F_1(x)$ and $F_2(x)$ are determined by the unpolarised quark distributions

$$q_f(x) = q_f^+(x) + q_f^-(x) \tag{2.58}$$

From formula 2.54 and 2.55 it follows that $F_1(x)$ and $F_2(x)$ are directly correlated by equation

$$F_2 = 2xF_1 = \sum_q e_q^2 x q(x) \tag{2.59}$$

The first identity, $F_2 = 2xF_1$, is known as the Callan-Gross relation [12] and is a direct consequence of the spin-$\frac{1}{2}$ nature of the quarks. The function $q(x)$ is known as the parton distribution function. The second identity is also interesting: it predicts that the cross section only depends on one variable, x. This property is called Bjørken scaling. Approximate scaling is observed in the data at $x \approx 0.1$, but violation of scaling is observed for lower and higher x. Fig. 2.2 shows F_2 versus Q^2 measured by various HERA- and fixed target experiments [2].

At the energy of the HERMES experiment only the u, d, s and $\bar{u}$, $\bar{d}$, $\bar{s}$, quarks contribute and the structure functions $F_2^p(x)$ for the proton is

$$F_2^p(x) = x\left[\frac{4}{9}u(x) + \frac{1}{9}d(x) + \frac{1}{9}s(x) + \frac{4}{9}\bar{u}(x) + \frac{1}{9}\bar{d}(x) + \frac{1}{9}\bar{s}(x)\right] \tag{2.60}$$

The contribution by charm and heavier quarks is neglected at moderate momentum transfer. Assuming SU(2) isospin symmetry, the structure function of the neutron is

$$F_2^n(x) = x\left[(\frac{1}{9}u(x) + \frac{4}{9}d(x) + \frac{1}{9}s(x) + \frac{1}{9}\bar{u}(x) + \frac{4}{9}\bar{d}(x) + \frac{1}{9}\bar{s}(x)\right] \tag{2.61}$$

Note that $u(x)$ is the momentum distribution of the 'up' quark in the proton and of the 'down' quark in the neutron:

$$u(x) \;=\; u^p(x) \;=\; d^n(x) \tag{2.62}$$

$$d(x) \;=\; d^p(x) \;=\; u^n(x) \tag{2.63}$$

A different parameterisation distinguishes between valence distributions q_ν which account for the quantum numbers of the nucleon and sea distributions $q_s(x) = \bar{q}_s(x)$ which arise from the production of quark-antiquark pairs due to quantum fluctuations:

$$\begin{aligned} F_2^p(x) \;&=\; x\left\{\frac{4}{9}\left[u_v(x) + u_s(x) + \bar{u}_s(x)\right]\right. \\ &+\; \left.\frac{1}{9}\left[d_v(x) + d_s(x) + \bar{d}_s(x) + s_s(x) + \bar{s}_s(x)\right]\right\} \end{aligned} \tag{2.64}$$

It should be mentioned that according to recent measurement [53], the light quark sea is not flavour symmetric:

$$u_s(x) \neq d_s(x) \tag{2.65}$$

The polarised quark distributions

In a similar way, the function $g_1(x)$ is determined by the spin distributions $\Delta q_f(x)$ of the quarks:

$$\Delta q_f(x) = q_f^+(x) - q_f^-(x) \tag{2.66}$$

The spin structure function $g_1^p(x)$ for the proton is given as

$$g_1^p(x) = \frac{1}{2}\left[\frac{4}{9}\Delta u(x) + \frac{1}{9}\Delta d(x) + \frac{1}{9}\Delta s(x) + \frac{4}{9}\Delta \bar{u}(x) + \frac{1}{9}\Delta \bar{d}(x) + \frac{1}{9}\Delta \bar{s}(x)\right] \tag{2.67}$$

The spin structure function $g_2(x)$ is zero in this simple model which neglects mass and intrinsic momenta of the quarks inside the nucleon.

2.3.2 Quantum chromodynamics improved QPM and sum rules

Quantum chromodynamics (QCD) is the theory of the strong interaction (color force), a fundamental force describing the interactions of the quarks and gluons found in hadrons, such as the proton and the neutron. QCD is a quantum field theory of a special kind called a non-abelian gauge theory. It is an important part of the Standard Model of particle physics. A huge body of experimental evidence for QCD has been gathered over the years. QCD is able to explain the confinement of quarks, the basic features of fragmentation and the asymptotic freedom of quarks at high momentum transfer.

asymptotic freedom, which means that in very high-energy reactions, quarks and gluons interact very weakly. That QCD predicts this behavior was first discovered in the early 1970s by David Politzer and by Frank Wilczek and David Gross. For this work they were awarded the 2004 Nobel Prize in Physics.

confinement, which means that the force between quarks does not diminish as they are separated. Because of this, it would take an infinite amount of energy to separate two quarks; they are forever bound into hadrons such as the proton and the neutron. Although analytically unproven, confinement is widely believed to be true because it explains the consistent failure of free quark searches, and it has been demonstrated in lattice QCD.

QCD in principle should be able to predict the quark wave functions of the nucleons, however theory is still far away from this goal as pertubative methods are not applicable and lattice calculations are very difficult and not yet far enough advanced. Neverless, techniques have been developed to approach the calculation of structure functions [54]. They can be illustrated by the following intuitive picture: with increasing Q^2 the resolution of the scattering process increases and more softer at high momentum transfer. The experimental results are in excellent agreement with the QCD predictions. The variation of the structure functions with Q^2 is used to extract the coupling constant (a_s) of the strong interaction [55].

A powerful technique to derive sum rules of the structure functions is the operator product expansion (OPE) [56]. In OPE the virtual photon-proton scattering amplitude is divided into a part which represents the long-distance physics and another which describes the light-cone physics. The latter one can be handled by techniques of pertubative QCD. The importance of these sum rules comes from the fact that they are derived directly from QCD and allow for a model independent test of QCD.

Operator production expansion

The Operator Production Expansion (OPE) [57, 58] formalism allows one to directly derive QCD sum rules for the structure functions. The importance of the sum rules relies on the fact that they do not depend on any model of hadronic structure, and provide a direct test of QCD. Integrated over the range in momentum fraction , the parton number densities have to reproduce the quantum numbers of the nucleon. The simplest integrals, or sum rules, are the first moments of the unpolarised densities that for the proton give baryon number one, charge one and strangeness zero,

$$\int_0^1 \mathrm{d}u_V(x,Q^2) = \int_0^1 (u(x,Q^2) - \bar{u}(x,Q^2)) = 2 \tag{2.68}$$

$$\int_0^1 \mathrm{d}d_V(x,Q^2) = \int_0^1 (d(x,Q^2) - \bar{d}(x,Q^2)) = 1 \tag{2.69}$$

$$\int_0^1 (s(x,Q^2) - \bar{s}(x,Q^2)) = 0 \tag{2.70}$$

The Gottfried sum rule [59] involves the proton and neutron structure functions F_2^p and F_2^n respectively:

$$\int_0^1 \frac{\mathrm{d}x}{x}(F_2^p(x,Q^2) - F_2^n(x,Q^2)) = \frac{1}{3} \tag{2.71}$$

This sum rule follows in the simple parton model, with the assumptions of isospin symmetry and of a symmetric light quark sea, $\bar{u}(x,Q^2) = \bar{d}(x,Q^2)$. Perturbative QCD corrections to the right hand side of Eq. 2.71 were found to be small [60]. Clear evidence of a deviation from the Gottfried sum rule was found at CERN in 1990 [61], showing that the symmetry of the light quark sea is violated.

Sum rules involving the polarised structure function provide insight into the nucleon spin structure. The integral of the proton and neutron structure functions $g_1^{p(n)}$ can be written as [30]

$$\Gamma_1^{p(n)} = \int_0^1 \mathrm{d}x g_1^{p(n)}(x,Q^2) = \frac{1}{12}\left(+(-)a_3 + \frac{a_8}{3}\right)\Delta C_{NS}(Q^2) + \frac{a_0}{9}\Delta C_S(Q^2) \tag{2.72}$$

where the minus sign is for the neutron structure function. $\Delta C_S(Q^2)$ and $\Delta C_{NS}(Q^2)$ are the singlet and non-singlet coefficient functions respectively.

In the $\overline{MS}$-renormalization scheme, they are for three quark flavours to second (third) order in [62]:

$$\Delta C_S(Q^2) = 1 - \frac{a_s(Q^2)}{\pi} - 1.096\left(\frac{a_s(Q^2)}{\pi}\right)^2 \tag{2.73}$$

$$\Delta C_{NS}(Q^2) = 1 - \frac{a_s(Q^2)}{\pi} - 3.583\left(\frac{a_s(Q^2)}{\pi}\right)^2 - 20.215\left(\frac{a_s(Q^2)}{\pi}\right)^3 \tag{2.74}$$

The quantities a_0, a_3, and a_8 measure the proton matrix elements of the flavour singlet, triplet, and octet vector currents:

$$a_3 = g_a/g_v = F + D = \Delta u - \Delta d \tag{2.75}$$

$$a_8 = 3F - D = \Delta u + \Delta d - 2\Delta s \tag{2.76}$$

$$a_0 = \Delta\Sigma = \Delta u + \Delta d + \Delta s \tag{2.77}$$

a_3 and a_8 are known from neutron and from hyperon decay. The numerical values are [63, 64]

$$\begin{aligned} F + D &= 1.2573 \pm 0.0028 & (2.78) \\ F/D &= 0.575 \pm 0.016 & (2.79) \end{aligned}$$

or

$$\begin{aligned} F &= 0.459 \pm 0.008 & (2.80) \\ D &= 0.798 \pm 0.008 & (2.81) \end{aligned}$$

However, the determination of a_8 requires the assumption of SU(3) flavour symmetry. The effects of symmetry breaking in hyperon β-decay were estimated to be on the order of 10% [65].

Bjørken sum rule

From the knowledge of axial vector coupling in weak interactions, a prediction for $\int \mathrm{d}x(g_1^p(x) - g_1^n(x))$ can be obtained based on isospin only. This is the famous Bjørken sum rule [66], which relates the difference of the first moments of the spin structure functions on a proton and a neutron target to the decay constant $g_a = |g_A/g_V| = 1.2670 \pm 0.00035$ [67] from neutron β-decay. Including QCD corrections, the Bjørken sum rule is written as:

$$\Gamma_1^{Bj} = \Gamma_1^p - \Gamma_1^n = \int_0^1 \mathrm{d}x[g_1^p(x, Q^2) - g_1^n(x, Q^2)] = \frac{1}{6}\left|\frac{g_A}{g_V}\right| \Delta C_{NS}(Q^2) \tag{2.82}$$

where $\Delta C_{NS}(Q^2)$ is given in Eqn. 2.74. At a scale of $Q_0^2 = 5GeV$ and using an input value for the strong coupling constant $a_s(m_{Z^0}) = 0.118 \pm 0.003$ at the mass of the neutral boson Z^0, the value for the Bjørken sum rule is $\Gamma_1^{Bj}(Q_0^2) = 0.182 \pm 0.003$. From the combined results of EMC, SMC, and E143 data, an experimental value, $\Gamma_{1,exp.}^{Bj} = 0.170 \pm 0.012$ [45], was obtained, thus confirming the theoretical prediction within the experimental and theoretical uncertainties. Alternatively, under the assumption that the Bjørken sum rule is accurate, Eq. 2.82 can be solved for $\alpha_s(Q^2)$ using Eq. 2.74 to obtain a rather precise value of $\alpha_s(m_{Z^0}) = 0.123^{+0.010}_{-0.006}$ [45].

Ellis-Jaffe sum rule

Ellis and Jaffe derived sum rules for Γ_1^p and Γ_1^n separately. They assumed the validity of SU(3) flavour symmetry and that the strange sea quarks and the gluons carry no net polarisation: $\Delta s + \Delta\bar{s} = \Delta g = 0$ [68]. Including the QCD corrections, the Ellis-Jaffe sum rule for the proton (neutron) can be expressed as:

$$\Gamma_1^{p(n)} = \int_0^1 g_1^{p(n)}(x)\mathrm{d}x = \frac{1}{12}\left(+(-)a_3 + \frac{a_8}{3}\right)\Delta C_{NS}(Q^2) + \frac{a_0}{9}\Delta C_S(Q^2) \tag{2.83}$$

or separately for the proton and the neutron:

$$\Gamma_1^p(Q^2) = \frac{1}{18}[(3F+D)\Delta C_{NS}(Q^2) + 2(3F-D)\Delta C_S(Q^2)] \tag{2.84}$$

$$\Gamma_1^n(Q^2) = \frac{1}{9}[-D\Delta C_{NS}(Q^2) + (3F-D)\Delta C_S(Q^2)] \tag{2.85}$$

At the same scale $Q_0^2 = 5GeV$ and using the same value for the strong coupling constant $a_s(m_{Z^0}) = 0.118 \pm 0.011$, the values of $\Gamma_1^p(Q_0^2) = 0.163 \pm 0.004$ and $\Gamma_1^n(Q_0^2) = -0.019 \pm 0.004$ from the Eqs. 2.84 and 2.85 can be obtained. A comparison with the combined experimental results $\Gamma_{1,\mathrm{exp}}^p(Q_0^2) = 0.118 \pm 0.004$ and $\Gamma_{1,\mathrm{exp}}^n(Q_0^2) = -0.058 \pm 0.005$, shows a significant violation of the Ellis-Jaffe sum rule [1]. This violation implies that there might be a SU(3) symmetry breaking, or there is a significant contribution from strange quarks and/or gluons to the spin of the nucleon. Under the assumption that SU(3) flavour symmetry is valid, it is possible to extract values for the strange quark polarization. As a surprise a relatively large negative value was obtained: $\Delta s + \Delta\bar{s} = -0.14 \pm 0.03$ [1].

2.4 Semi-inclusive deep inelastic scattering

As presented in Sect. 2.1, the Semi-Inclusive Deep Inelastic Scattering (SIDIS) is such process that at least one final state hadron is detected in coincidence with the scattered lepton. To analyse the polarised SIDIS events may offer another way to access more information on the spin structure of nucleon.

2.4.1 Semi-inclusive cross section and asymmetries

In LO QCD the differential cross section $\frac{\mathrm{d}\sigma^h}{\mathrm{d}z}$ for the production of a hadron of type h can be expressed in terms of fragmentation functions and unpolarised quark distribution functions as:

$$\frac{\mathrm{d}\sigma^h}{\mathrm{d}z} = \sigma_{\mathrm{INCL}} \left[\frac{\sum_f e_f^2 q_f(x,Q^2) D_f^h(Q^2,z)}{\sum_f e_f^2 q_f(x,Q^2)} \right] \tag{2.86}$$

Where σ_{INCL} is the inclusive DIS cross section. The $D_f^h(z,Q^2)$ are called fragmentation functions and denotes the probability to find a hadron h with momentum fraction z if a quark of flavour f has been struck in the hard-scattering subprocess.

Furthermore, the unpolarised and polarised semi-inclusive structure functions F_1^h and g_1^h are defined in LO as

$$F_1^h(x,Q^2,z) = \frac{1}{2}\sum_f e_f^2 q_f(x,Q^2) D_f^h(Q^2,z) \tag{2.87}$$

$$g_1^h(x,Q^2,z) = \frac{1}{2}\sum_f e_f^2 \Delta q_f(x,Q^2) D_f^h(Q^2,z) \tag{2.88}$$

The definition of g_1^h is valid under the assumption that the fragmentation process is independent of the relative orientation of the spin of the struck quark with respect to the spin of the target nucleon.

Using the same assumption as in the inclusive case, the semi-inclusive photon asymmetry is obtained from

$$\begin{aligned}
A_1^h(x,Q^2) &\overset{g_2^h=0}{\simeq} \frac{\int_{z_{min}}^1 \mathrm{d}g_1^h(x,Q^2,z)}{\int_{z_{min}}^1 \mathrm{d}F_1^h(x,Q^2,z)} = \frac{\sum_f e_f^2 \Delta q(x,Q^2) \int_{z_{min}}^1 \mathrm{d}z D_f^h(Q^2,z)}{\sum_f e_f^2 q(x,Q^2) \int_{z_{min}}^1 \mathrm{d}z D_f^h(Q^2,z)} \\
&= \frac{A_{||}^h(x,Q^2)}{D(1+\eta\gamma)} \qquad (2.89)
\end{aligned}$$

where the integration is performed over the range in z, as applied to select hadrons from the current fragmentation region. Given the integrated fragmentation functions and the unpolarised quark distributions $q_f(x,Q^2)$, Eq. 2.89 will be the basis for the extraction of the polarised quark distributions $\Delta q_f(x,Q^2)$ from a set of semi-inclusive asymmetries.

Semi-inclusive asymmetries offer more direct information on the individual contributions of the different quark flavours. Within the QPM, the charge and the valence quark composition of the hadron detected in coincidence with the scattered lepton provided sensitivity to the flavour of the struck quark.

In Chapter 8, a method of accessing quark polarisation in semi-inclusive data will be presented. From the measured semi-inclusive asymmetries, the quark polarisation and helicity of the nucleon spin can be performed at the LO QCD by using Eq. 2.89 in combination with an input parameterisation STEQ6 for the unpolarised parton distributions $q_f(x,Q^2)$ and the integrated fragmentation functions.

2.4.2 Fragmentation functions

With the quark model, in the laboratory frame, the semi-inclusive DIS process is described in terms of a single quark which is struck by the virtual photon and ejected from the nucleon (see Fig. 2.1). The struck quark absorbs the energy of the virtual photon and is ejected along the direction of the virtual photon. Due to the confinement properties of QCD, both the struck quark and the target remnants have to form a set of colour neutral final state hadrons. This process is so called hadronisation, and can not be described in perturbative QCD, because it involves long-range interactions between the struck quark and the target remnant as they move apart. Instead, the hadronisation process is parameterised by fragmentation functions $D_f^h(Q^2,z)$, which give the probability density that a struck quark of flavour f, probed at a particular scale Q^2, produces a final state f hadron with fractional energy z.

The fragmentation functions are normalised to conserve energy and particle multiplicities n_h:

$$\sum_h \int_0^1 \mathrm{d}zz \cdot D_f^h(Q^2, z) = 1 \tag{2.90}$$

$$\sum_f \int_0^1 \mathrm{d}z D_f^h(Q^2, z) = n_h(Q^2) \tag{2.91}$$

Since the fragmentation process proceeds by the strong interaction, charge conjugation and isospin invariance reduce the number of independent fragmentation functions significantly. In the case of charged pions, for three different flavours of quarks and antiquarks, the total number of twelve possible combinations can be reduced to three independent fragmentation functions, using charge conjugation symmetry $[D_u^{\pi^+}(z) = D_{\bar{u}}^{\pi^-}(z)]$ and isospin symmetry $[D_u^{\pi^+}(z) = D_d^{\pi^-}(z)]$:

$$D_+ = D_u^{\pi^+}(z) = D_{\bar{u}}^{\pi^-}(z) = D_{\bar{d}}^{\pi^+}(z) = D_d^{\pi^-}(z) \tag{2.92}$$

$$D_- = D_u^{\pi^-}(z) = D_{\bar{u}}^{\pi^+}(z) = D_{\bar{d}}^{\pi^-}(z) = D_d^{\pi^+}(z) \tag{2.93}$$

$$D_s \;= D_s^{\pi^+}(z) = D_{\bar{s}}^{\pi^-}(z) = D_{\bar{s}}^{\pi^+}(z) = D_s^{\pi^-}(z) \tag{2.94}$$

The fragmentation function D_+ is called favoured fragmentation function as the initial quark which produced the pion is in their ground state wave function. Such process are more probable than the unfavoured fragmentation function D_- and strange fragmentation function D_s. The dependence on Q^2 has been omitted here.

In the Børken limit, factorisation demands that the hadronisation process is independent of the hard photon-quark scattering process, and hence should be independent of x and Q^2. The fragmentation process is assumed to be universal, i.e. independent of the original environment of the initial quark, which starts the hadronisation process. This environmental independence implies that fragmentation functions determined in DIS should equally well describe hadronisation processes from $q\bar{q}$ pair production in e^+e^- collisions, which has been confirmed experimentally [69, 70].

2.4.3 Fragmentation models

As already mentioned, the fragmentation process cannot be calculated from the first principles in perturbative QCD directly, fragmentation models have been developed in order to provide a general framework in which the properties of hadron production can be studied phenomenologically [71]. In particular, the models have been designed to be used in Monte Carlo programs.

The models are based on the quark-parton model. Two important models, the independent fragmentation model and the LUND string fragmentation model, have been implemented into the JETSET Monte Carlo generator [72, 73, 74], which is used at HERMES. The models contain parameters, which have to be adapted to the kinematical domain of the experiment. These model parameters have been adjusted to reproduce measured particle multiplicities and event shapes optimally in a recursive tuning procedure [75, 76].

The independent fragmentation model

The independent fragmentation model was developed in the early 1970s by Field and Feynman [77] to reproduce the limited transverse momenta and approximate scaling of energy fraction distributions observed in quark jets produced in e^+e^--annihilation. It is based on the simple assumption that every parton fragments independently. In this model, the struck quark q_0 combines with the antiquark $\bar{q}_1$ of a quark-antiquark pair $q_1\bar{q}_1$ created out of the vacuum. The $q_0\bar{q}_1$ creates the first rank primary meson with energy fraction z_0, see Fig. 2.7.

In the model, the "rank" of a specific hadron is the ordering in production time in the center-of-mass system, starting with the hardron containing the struck quark.

The left over energy fraction $(1 - z_0) = z_1$ of the first-rank primary meson $q_0\bar{q}_0$ is

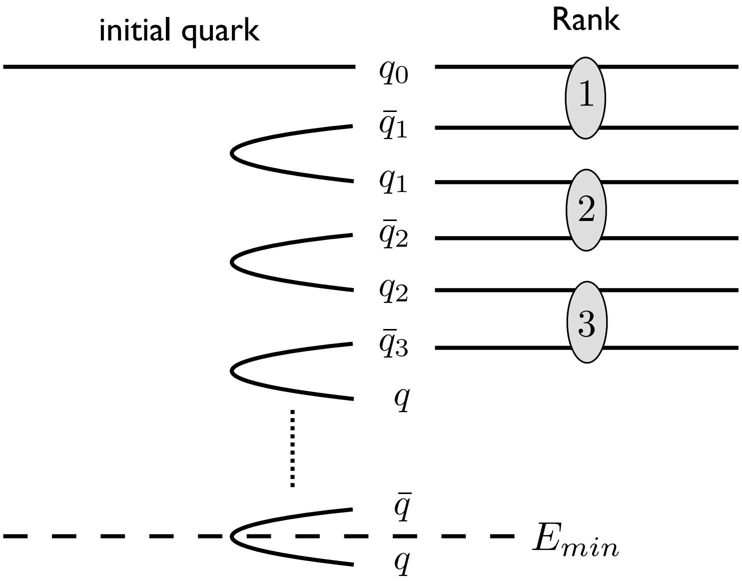

Figure 2.7: Diagram of independent fragmentation.

assigned to the remaining quark q_1. In this way, quark-antiquark pair $q_i\bar{q}_i$ are created with energy fraction $(1 - z_i)$. The antiquark $\bar{q}_i$ then combines with the quark of the former rank q_{i-1} to form a meson with quark content $q_{i-1}\bar{q}_i$. The energy is assigned randomly according to an universal distribution $f(z)$ which cause the fragmentation to scale with energy. This precess proceeds until the remaining energy falls below cut-off E_{min}. The produced mesons may be unstable and decay to long-lived particles after their formation.

The transformation into a different reference frame does not conserve the relative momenta and hence the multiplicities of produced particles change. Furthermore, the colour and flavour quantum numbers are not conserved, because the last quarks below the energy cut-off are neglected.

The string fragmentation models

The LUND String Fragmentation (SF) model [78] is based on the idea that a fragmenting quarks system is connected by colour flux tubes, or string. It employs the concept of linear confinement, motivated by QCD. In this model, the initial partons are connected via the colour field stretching in between them. This colour field is assumed to possess a constant field energy density per unit length, which leads to a linear rising potential for two partons separated by a distance . As the struck parton moves apart from its partner, the energy stored in the colour string exceeds the mass of a pair. At this point the string breaks up and forms a pair, connecting now two strings to the initial pair of partons. These new substrings continue to break independently, until a string-connected quark-antiquark pair is close to the mass shell of a colour singlet hadron. (See Fig. 2.8).

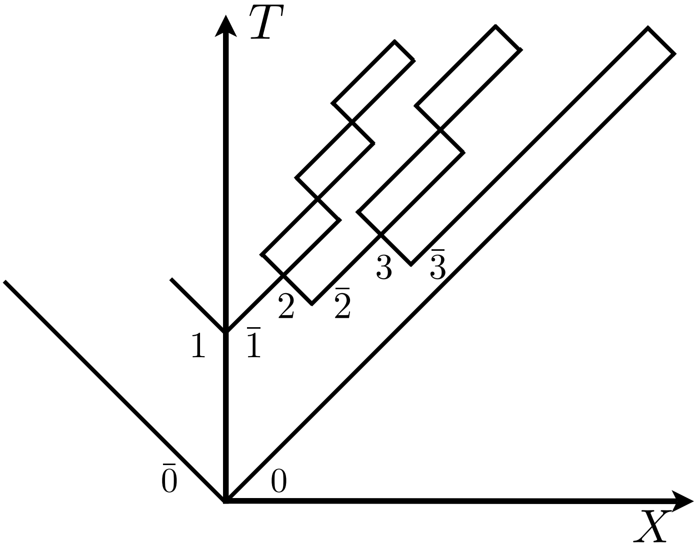

Figure 2.8: Hadroproduction in e^+e^--annihilation according to the Lund string model. The initially produced quark $q_0\bar{q}_0$, denoted here by 0 and $\bar{0}$, are moving away in opposite directions. Quark-antiquark pairs are produced in the field. The production point of a $q\bar{q}$ pair is lying on a hyperbola given by $(\Delta x)^2 - (\Delta t)^2 = const.$

The LUND SF model has up to date proven to be a very successful model for the description of experimental data. The production probability of a pair in this tunnelling mechanism is controlled by two free parameters, which have to be determined by tuning the model to experimental distributions.

As a main advantage over the IF model, the LUND string model conserves all quantum numbers and it is invariant under Lorentz transformations. It has been implemented in the JETSET Monte Carlo package [72, 73, 74]. The default parameters of this model were optimised to describe the high energy data of collider experiments at LEP and HERA. For a satisfactory description of the hadron multiplicities measured at HERMES they had to be tuned, as described in [75, 76].

Chapter 3

The HERMES experiment

HERMES, the name comes from HERa MEasurement of Spin, [79] is one of the four experiments at HERA at the DESY laboratory in Hamburg, Germany. HERMES is designed for precise measurement of the nucleon spin structure. It uses the high current longitudinally polarised electron beam of HERA with a beam energy of about 27.5 GeV together with polarised and unpolarised gas targets internal to the storage ring. Scattered electrons and particles produced in the deep-inelastic electron-nucleon interactions are detected and identified by an open-geometry forward spectrometer with large momentum and solid angle acceptance.

HERMES is based on two novel techniques: longitudinal electron polarisation in a high energy storage ring, which is achieved by a system of spin rotator magnets, and a storage cell target where the polarised atoms from a high intensity polarised source are present as pure atomic species without dilution from unpolarised target material.

In this chapter, the components of the HERA accelerator relevant to the HERMES experiment, the HERMES target, the HERMES spectrometer, the luminosity and the data acquisition system are described. More detailed information is found in ref. [79]

3.1 The polarised electron beam at HERA

The HERA accelerator provides two beams, one is 920 GeV protons and another one is 27.5 GeV electrons or positrons. In addition to HERMES, they are used by two collider experiments ZEUS and H1. The HERMES experiment is operated in the east hall of the storage ring facility HERA, diametrically opposite to the HERA-B hall. It is one of two fixed target experiments. The experiments ZEUS and H1 are investigating nucleon structure functions by means of deep inelastic scattering over a wide kinematic region in collider mode. The goal of HERA-B experiment was to study CP-violation in B-meson production in proton-proton collisions.

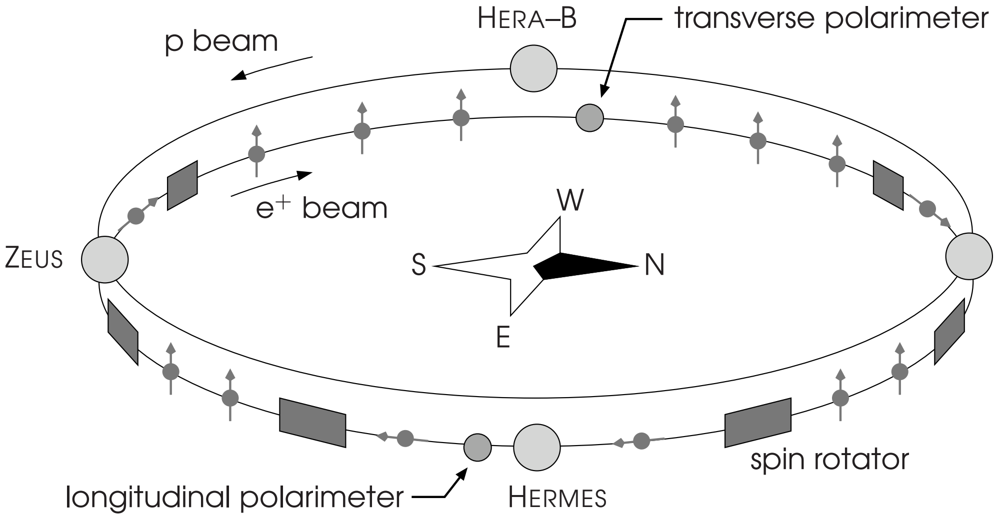

Figure 3.1: Location of HERMES at the HERA storage ring. The other experiments H1, HERA-B and ZEUS, the Spin rotators and polarimeters are superimposed. The setup of run 2001-2007 is shown. Prior to 2001 there were no rotators at H1 and ZEUS.

The HERA electron beam has a time structure which allows for up to 220 bunches along the HERA storage ring's 6.3 km circumference which have a length of 27 ps and are separated by 96 ns. This corresponds to a duty factor of 0.3×10^{-3}. The average beam current at injection is up to 50 mA and due to residual gas interactions, the beam current decays nearly exponentially. The average lifetime, which can be derived from the decay constant, is between 12 and 14 hours. Usually the beam is dumped earlier by inserting high density unpolarised gas in the HERMES target cell in order to obtain large statistics for unpolarised DIS experiments (important for the study of nuclear effects).

In high-energy storage rings, electron beams can became transversely polarised through the emission of spin-flip synchrotron radiation [80] in the arcs, the so-called Sokolov-Ternov mechanism. This process is due to an asymmetry in the synchrotron radiation cross section. The theoretical limit for polarisation is 92.4%. The real polarisation reaches typically about 55% approximately 40 minutes after the start of the fill.

Spin rotators have been installed upstream and downstream of the HERMES experiment (see Fig. 3.1), since for the measurement of the beam spin asymmetries, longitudinal polarisation is required in contrast to polarisation in the storage ring which is in the transverse direction. The spin rotators at H1 and ZEUS were installed in addition during the shutdown of 2001. The polarisation of the beam is measured by two laser backscattering polarimeters. The transverse polarimeter is located in the West Hall and longitudinal polarimeter is inside the spin rotator at the East Hall.

3.2 The internal gas target

A fixed target in a storage ring needs a special setup to preserve a reasonable life time of the stored beam, without causing significant disruption to the beam lifetime, requiring a fill to remain for at least 10 hours. This immediately excluded any possibility of using solid material for the target in HERMES. In fact, the target density is limited to 10^{15} atoms/cm^2. In order to fulfil the requirement of HERA, a gaseous target [81] cell intended to sit inline to the storage ring was designed for use in the experiment.

The HERMES experiment uses an innovative technique for the polarised target, which is very different from other polarised deep-inelastic scattering experiments, that is a polarised gas target internal to the HERA storage ring. This technique permits

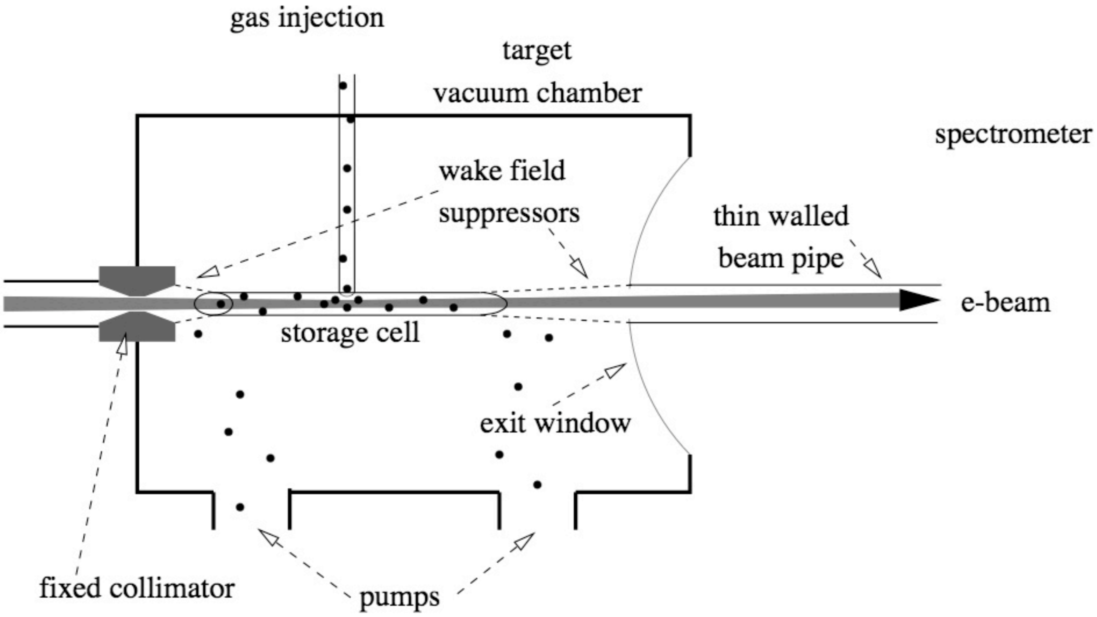

Figure 3.2: Diagram of the target chamber. The figure omits to show the asymmetric design of the target cell, see text for detail. The diagram is not to scale.

essentially background-free measurements from highly polarised nucleons with little or no dilution of the signal from unpolarised nucleons in the target.

The HERMES experiment uses both polarised and unpolarised targets. The polarised target consists of Hydrogen, Deuterium or ^{3}He, whilst the unpolarised gases are one of H_2, D_2, ^{3}He, ^{4}He, N_2, Ne, Kr, and Xe. A polarised ^{3}He target was used in 1995 but during 1996 - 1997 a longitudinally polarised hydrogen target was used and in 1998 - 2000 longitudinally polarised deuterium. In 2001, a transversally polarised target was installed during a HERA upgrade.

The polarised hydrogen(deuterium) beam is produced by means of an atomic beam source (ABS) [82]. This device consists of dissociator, powerful differential pumping system, beam forming system, sextuple magnet system and adiabatic high-frequency transitions.

Molecular hydrogen/deuterium gas is dissociated by a radio frequency of 13.56 MHz in a pyrex-type tube. The degree of produced dissociation is up to 80 %. Atomic gas flows through a conical nozzle with an opening of diameter 2 mm, which is cooled to

100 K. Five sextupole permanent magnets split this beam into hyperfine states. The particular polarisation state of interest is selected by combination of strong field transition (SFT), medium field transition (MFT) and weak field transition (WFT). The polarised atomic beam is injected into target cell with a pressure of about 10^{-7} mbar. The target cell is an elliptical tube with open ends which holds the gas at the lepton beam position. At the end of the target cell two powerful turbo-pumps are installed in order to protect the ultra high vacuum in the accelerator ring.

For polarised gas, there are two instruments installed for monitoring: a Breit-Rabi Polarimeter (BRP) and Target Gas Analyser (TGA). The former measures the polarisation of the gas and the latter gives an estimate of the degree of dissociation. For unpolarised gas, neither measurement makes sense, so the gas is filled directly into the target cell.

3.3 The HERMES spectrometer

A schematic side view of the HERMES spectrometer with a dipole magnet is shown in Fig. 3.3. It is a forward spectrometer that consists of two identically constructed halves, one above and one below the HERA beam pipes. Both the positron and the proton beam pass through the central plane of the spectrometer and are shielded from the HERMES magnetic field by a steel plate. Each spectrometer half consists of a set of tracking chambers, hodoscopes (trigger) and four particle identification detectors. A luminosity monitor is installed at the rear of the spectrometer. The acceptance of the spectrometer extends vertically from 40 to 140 mrad and horizontally to ±170 mrad. The resulting total angular acceptance from 40 to 220 mrad covers a large kinematic region.

3.3.1 Magnet and tracking detectors

The dipole magnet of the HERMES forward spectrometer, surrounding the electron and proton beam pipes, provids an integrated field of $\int B\mathrm{d}l = 1.3$ Tm. The magnet is divided into two identical sections, "up" and "down", by a horizontal septum plate

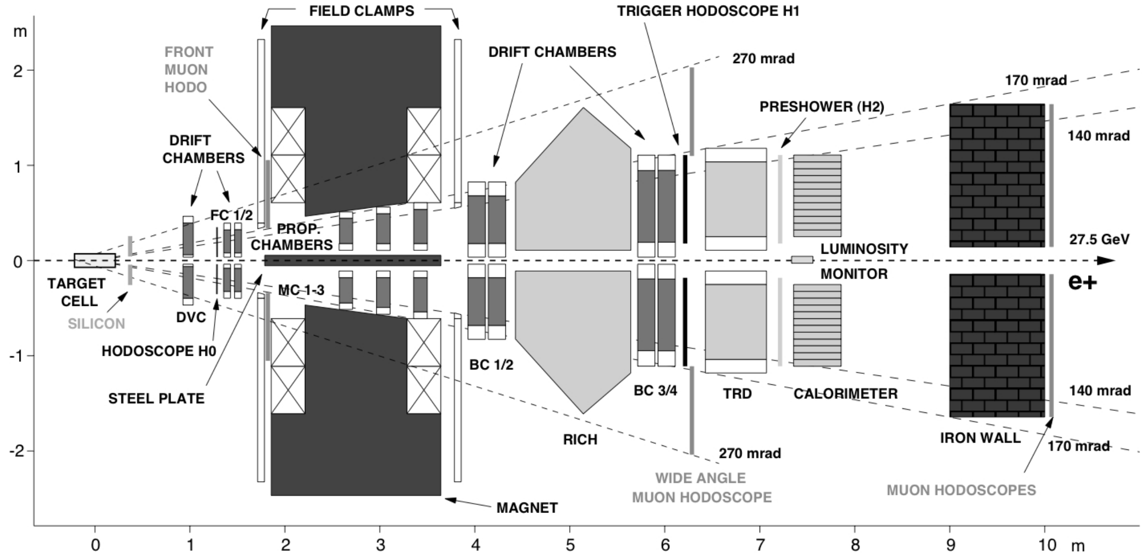

Figure 3.3: Side view of the current setup of the HERMES spectrometer

that shields the electron and proton beams from the spectrometer's magnetic field. Consequently, the spectrometer is constructed as two identical halves, mounted above and below the beam pipes. The acceptance of the spectrometer is given by the opening angle of the spectrometer magnets. And the protection of the electron and proton beams against strong magnetic field is accomplished by a septum plate which limits acceptance for small vertical scattering angle to 40 mrad. So the scattered electrons and hadrons produced in the inelastic reactions can be detected and identified within an angular acceptance 170 mrad horizontally and $40 - 140$ mrad vertically. The deflection of the charged particles by magnetic field is used for measurement of their momenta. This is accomplished by measuring the particles' track in the magnetic field region of the spectrometer. For tracking in each spectrometer half several tracking chambers (multiwire proportional chambers and drift chambers) before, inside and behind the magnet are used. Due to the 40 cm long extended gas target, the tracking detectors in front of the magnet are needed for the determination of the interaction vertex, the polar and azimuthal scattering angles of the particles and the initial trajectory for the determination of the particles momentum.

Tracking detectors measure a full complement of track information for any registered particle: the scattering angle (θ), the azimuthal angle (ϕ) and the vertex position. The tracking detector system is depicted in Fig. 3.3.

- DVC: The Drift Vertex Chambers have been installed in 1996 and are in use since the data taking in 1997. They help to increase the redundancy of the tracking system in the front region and have a larger geometrical acceptance than the other detectors extending vertically from ±35 mrad to ±270 mrad and covering ±200 mrad horizontally, mainly to increase the efficiency for the detection of events from charmed particle decays. The width of the drift cell is 6 mm, the module has 6 planes with the configuration XX′UU′VV′, the total number of wires is 1088. The non-flammable gas mixture is the same as for all the other drift chambers: $Ar/CO_2/CF_4$ (90/5/5), the spatial resolution per plane (σ) is 220 μm.

- FC1/2: The Front Chambers [83] provide good spatial resolution immediately in front of the magnet. They are drift chambers with a cell width of 7 mm, each module has six planes with a UU′XX′VV′ configuration, resulting in 2304 channels. The measured resolution per plane is 225 μm.

- MC1/3: The magnet chambers MC1 through MC3 [84] are multiwire proportional chambers with a spacing of the readout wires of 2 mm and a corresponding resolution per plane of 700 μm. They are located in the gap of the magnet and were originally intended to help resolve multiple tracks in case of high multiplicity events and to improve track reconstruction in case of missing planes in the front region. Since low background and good performance of the front detectors have made this unnecessary, their primary function is now the momentum analysis of relatively low energy particles from the decay of Λ hyperons or K_s, mesons, for example. Each module has three planes of the configuration UXV, the total number of channels is 11008, and the gas mixture used is $Ar/CO_2/CF_4$ (65/30/5).

- BCl-4: The Back Chambers BCl through BC4 [85, 86] are drift chambers with a cell width of 15 mm. Each of the four modules has six planes with UU′XX′VV′

configuration. The active areas of the chambers are chosen according to their z-position and the acceptance of the spectrometer, resulting in 7680 channels. The measured resolution per plane is in average 275 μm (300 μm) for BC1/2 (BC3/4) with a minimum of about 210 μm (250 μm) in the middle of the drift cell.

3.3.2 Particle identification detectors

Particle Identification (PID) at HERMES is provided by a dual-radiator Ring Imaging Čerenkov Detector (RICH) which replaced the threshold Čerenkov Detector from 1998, a Transition Radiation Detector (TRD), a Preshower Detector, and a lead glass Electromagnetic Calorimeter. Combining the four detectors together, the HERMES experiment provides an excellent hadron-lepton separation.

Ring-Imaging Čerenkov Detector (RICH)

Semi-inclusive deep inelastic scattering in which a hadron is detected in coincidence with a lepton scattered from the incident beam is the primary reaction studied in the HERMES experiment. The detection of an identified coincident hadron provides an additional dimension for probing experimentally the flavor structure of elementary particles and related phenomena. For the kinematics characteristic of the HERMES beam energy of 27.5 GeV, 95% of the hadrons produced are in the momentum range of 2-15 GeV. In order to achieve reasonable PID over the full range of momenta, a dual radiator RICH detector [87] which used the clear aerogel in combination with a heavy gas, C_4F_{10} was developed and installed in 1998, to provide clean separation of pions, kaons, and protons over most of the acceptance of the HERMES experiment.

The RICH detector consists of two symmetric RICH modules, which are positioned between the two rear tracking chambers BC1/2 and BC3/4. The upper part is shown in Fig. 3.4.

The aerogel radiator is a wall of tiles configured to fill the entrance of the detector with an aerogel thickness of 5 cm, in total 5 × 17 × 5 tiles silica aerogel, each size

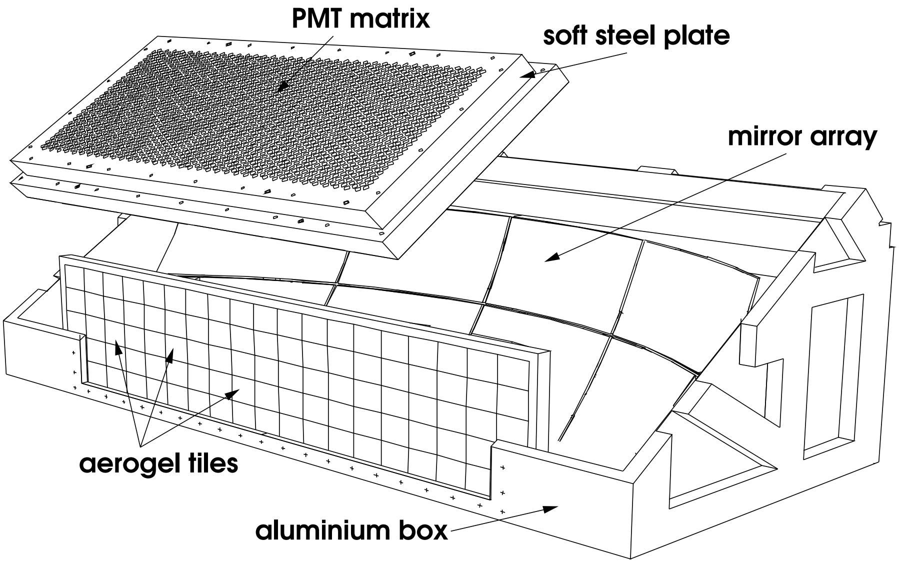

Figure 3.4: A perspective view of the upper RICH detector setup

$11 \times 11 \times 1.0$ cm^3, which refractive index is 1.0303 and performs PID covering the lower part of the accepted momentum range. The unoccupied space of the detector behind the aerogel is filled with the gas radiator, 4000 litre volume C_4F_{10}, which refractive index is 1.00137. A 2×8 spherical mirror array located at the rear of the radiator box images the Čerenkov light on a focal surface located above (below) the active volume. The mirror array is a graphite fiber composite structure with a radius of curvature of 220 cm. The photon detector is a hexagonal close-packed matrix of 1934 Philips XP1911/uv green enhanced photomultipliers (PMTs) which are read out by a LeCroy PCOS4 system. These photomultiplier tubes give a pixel size of 23.3 mm and a corresponding single photon angular resolution.

When a charged particle in a material medium moves faster than the speed of light in that same medium, it emits Čerenkov Radiation on a cone with a characteristic opening angle θ_c given by [88].

$$\cos\theta_C = \frac{1}{n\beta} \tag{3.1}$$

Where n is the refraction index of the material and $\beta = \frac{v}{c}$ is the ratio of the velocity v of the particle and the speed of light in vacuum c. And the Čerenkov threshold

	Aerogel	C_4F_{10}
n	1.0304	1.00137
P^{π}_{thresh}	0.6 GeV	2.7 GeV
P^{k}_{thresh}	2.0 GeV	9.4 GeV
P^{p}_{thresh}	3.8 GeV	17.9 GeV

Table 3.1: The Čerenkov light threshold for pions, kaons and protons. The index of refraction for Aerogel and C_4F_{10} is given at 633 nm.

momentum p_{thresh} for the particle emitting the Čerenkov Radiation in a material medium is given by

$$p_{\text{thresh}} = \frac{m}{\sqrt{(n^2 - 1)}} \tag{3.2}$$

where m is the mass of the particle. The refractive indices of the radiators for the HERMES dual-radiators RICH and the threshold momenta can be found in Table 3.1.

In the RICH detectors, the Čerenkov cone is focused on the matrix of photon detectors where a ring pattern is created. The diameter of the ring is proportional to the Čerenkov angle θ_C.

The RICH particle identification is based on reconstruction of the Čerenkov angle and the particle momentum which is estimated by track reconstruction in BC and FC and deflection radius in the spectrometer magnet. Since the position of the track is known from the track reconstruction and the Čerenkov photons are detected by the RICH PMTs which position are also known, the Čerenkov photons angle θ_C can be calculated.

At HERMES, hadrons are separated from leptons with the TRD and calorimeter components of the spectrometer.

For the hadron identification with the RICH, two different concepts are employed: *Indirect Ray-Tracing Method* (IRT) and *Direct Ray-Tracing Method* (DRT)

IRT: For each track, it is assumed that the hit could be coming from the aerogel

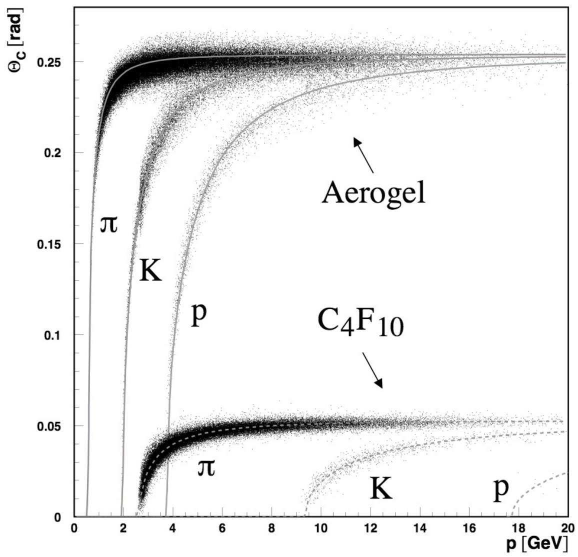

Figure 3.5: Distribution of reconstructed angles in the HERMES RICH. The upper triplet of curves corresponds to aerogel events, and the lower to gas events. From left to right the contours in each case are for π, K, and p.

or the gas, and the photon emission point is estimated accordingly. For each radiator hypothesis, the distribution of angles for hits in an angular range corresponding to each particle hypothesis (π, K, and p) is reconstructed. The likelihoods for the two radiators are combined in an overall likelihood. The advantages of this method lie in its fast and robust calculation.

DRT: The DRT Method calculates a hit probability for each photon-multiplier of the matrix by a full Monte-Carlo simulation. This is done specifically for the track configuration of every event under all particle hypotheses possible. The particle type is deduced from the actual hits and their simulated probabilities. Compared to the IRT Method, DRT needs orders of magnitude more computering time but for instance identifies events with more tracks in one detecter half more reliably.

Identification is based on the highest likelihood, L_1, consistent with a value of the quality parameter,

$$rQ_p = \log_{10} \frac{L_1}{L_2} \tag{3.3}$$

greater than a preassigned value.

During the processing of HERMES events, a program, the RICH PID-Scheduler[89], decides event-wise which method is best to be employed.

The distribution of average reconstructed angles using this decision network for (π's, K's, and p's) is shown in Fig. 3.5

Transition Radiation Detector (TRD)

The two halves (top and bottom) of the HERMES TRD are located between the two hodoscopes H1 and H2. Each half consists of six identically constructed models in a row (shown in Fig. 3.6)

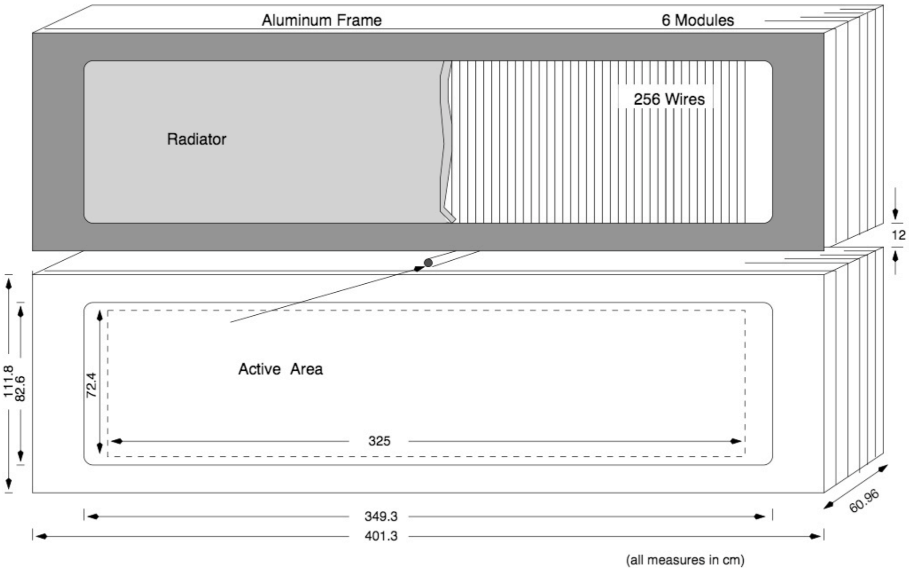

Figure 3.6: Overview of TRD detecter.

A single module contains a 6.35 cm thick matrix of polypropylene/polyethylene fibres as radiator in front of a 2.54 cm thick Multi-Wire Proportional Chambers (MWPC). The MWPC is filled with a mixture of 90% Xe and 10% CH_4 and detects the generated transition radiation photons as well as the energy lost by the charged particle through ionisation. The large active area of $2 \times 72.4 \times 325$ cm^2 of both TRD halves covers the entire HERMES acceptance.

When a highly relativistic point charge traverses a dielectric boundary, it emits

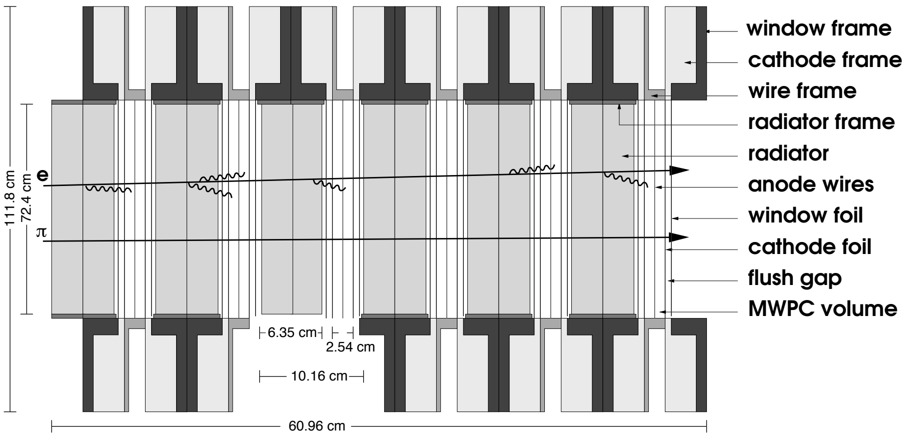

Figure 3.7: The upper half of the TRD with a positron and a pion track. The opening angles of the transition radiation produced by the lepton are exaggerated.

electromagnetic radiation. In this case, an electromagnetic wave is emitted. The photons are usually emitted in the visible part of the spectrum but an X-ray may be emitted as well. To increase the probability of the emission of X-ray photons in the Transition Radiation Detector (TRD), a high number of boundaries are introduced. The ideal case would be a set of thin foils with a narrow uniform separation by vacuum. Such a construction is technically difficult. In the HERMES TRD it is replaced by packets of pseudo-randomly arranged polypropylene/polyethylene fibers with diameters of 17-20 μm. The fiber material is held in place with an aluminium frame and stitched together to maintain the proper density.

Preshower Detector

Located behind the TRD, the hodoscope wall H2 with a 11 mm lead curtain in front is used as pershower detector. The hodoscope H2 consist of 42 vertical plastic scintillator paddles with photo-multipliers mounted on the end away from the beam pipe(Fig. 3.8). The thickness of the lead corresponds to two radiation lengths so positrons have a relatively high probability of starting an electromagnetic shower which can be detected in the scintillators. The resulting light is captured by the photo-multipliers. Since the nuclear interaction length is much larger than a radiation length, hadrons have a much lower probability of showering than positron. Hadrons will give only a minimum ionising signal in hodoscope H2 and can be separated from positrons.

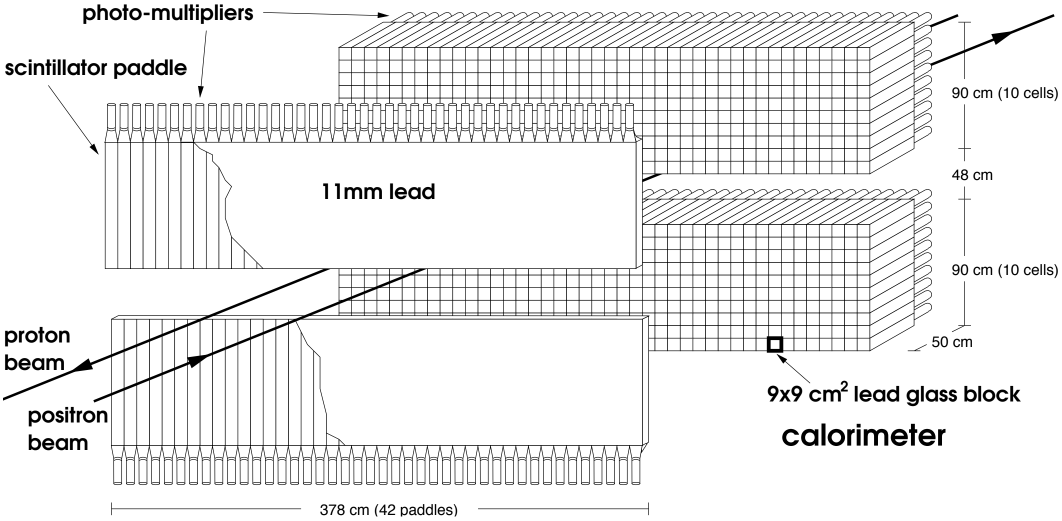

Figure 3.8: Overview of the preshower and the calorimeter.

Calorimeter

The lead glass calorimeter [90] follows downstream of the preshower detector. The calorimeter serves to separate positrons and electrons from hadrons as well as to detect energetic photons. The upper and lower half of the calorimeter can be moved 50 cm away from the beam during injection to avoid radiation damage. Each half consists of 42×10 lead glass blocks of 9×9 cm^2 (Fig. 3.8). The length of the calorimeter blocks corresponds to 18 radiation lengths. The light is collected in photo-multiplier tubes mounted at the rear of each block.

The 18 radiation lengths provided by calorimeter wall make it most likely that a shower started by a photon or a positron is completely contained in the material. The hadron-lepton separation in the calorimeter is based on this fact. Hence, for photons, positrons, and electrons the ratio of deposited energy to momentum (E_{CALO}/p) is equal to one. Hadrons deposit only a fraction of their energy in the calorimeter ($E_{\mathrm{CALO}}/p < 1$). Neutral photons are stopped in the calorimeter as well. Since photons do not produce ionisation along their track in the detector, they are identified as a hit in the calorimeter and a corresponding missing hit in the hodoscope system. The energy resolution of the HERMES calorimeter is

$$\frac{\sigma(E)}{E}[\%] = \frac{5.1 \pm 1.1}{\sqrt{E[GeV]}} + (1.5 \pm 0.5) \tag{3.4}$$

The selection of leptons from hadrons is done by combining the information from all PID detectors.

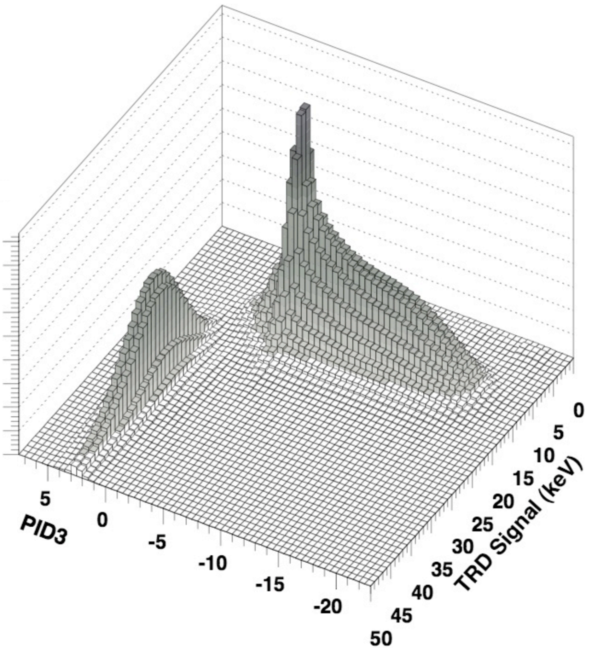

Figure 3.9: Hadrons and leptons separation via PID3 and TRD.

The probability functions $\mathcal{P}_i^j(p,x)$ (where the particle i with momentum p causes a response x in the detector j) are calculated. This is accomplished by comparing detector response to so-called "parent distributions". The parent distributions are obtained from data and Monte-Carlo simulations. By combining the probability functions of the calorimeter and the preshower, a likelihood (rPID3) is obtained:

$$r\text{PID3} = \log_{10} \frac{\mathcal{P}^e_{Cal} \cdot \mathcal{P}^e_{\check{C}er} \cdot \mathcal{P}^e_{Pre}}{\mathcal{P}^h_{Cal} \cdot \mathcal{P}^h_{\check{C}er} \cdot \mathcal{P}^h_{Pre}} \tag{3.5}$$

The rPID3 is the logarithmic likelihood that a certain particle has been identified by the calorimeter and the preshower as a lepton, rather than a hadron. The same method is used for the calculation of the value rPID5 in the case of the TRD, where each module is treated as an independent detector:

$$r\mathrm{PID5} = \log_{10}\frac{\mathcal{P}^{e}_{TRD}}{\mathcal{P}^{h}_{TRD}} = \log_{10}\frac{\prod_{i=1}^{6}\mathcal{P}^{e}_{TRD_i}}{\prod_{i=1}^{6}\mathcal{P}^{h}_{TRD_i}} \tag{3.6}$$

The sum of PID parameters, rPID3 $+r$PID5, is used for hadron selection. The efficiency of lepton-hadron separation is better than 98% with a contamination of less than 1%.

3.4 Luminosity monitor

The measurement of absolute and relative luminosities are necessary for the calculation of cross sections and cross section asymmetries. In the HERMES experiment the luminosity is measured by means of a reference scattering process which is the scattering of beam leptons off shell electrons in the target gas. In case of a positron beam there are the annihilation into photons and the Bhabha scattering process. For electrons as beam particles Møller scattering takes place. For high energetic beam positrons which scatter off or annihilate with fixed target shell electrons, the scattering angles of both leptons or two photons, respectively are small. Therefore the luminosity monitor (LUMI)[91, 92] consists of a pair of small electromagnetic calorimeters installed 7.21 m downstream the target on the left and right of the positron beam line. Each calorimeter of the luminosity monitor consists of an array of 3×4 radiation resistant $\mathrm{NaBi(WO_4)_2}$ Čerenkov crystals with a size $22 \times 22 \times 200$ mm^3 (Fig. 3.11). The charged particles of an electromagnetic shower produce Čerenkov light in the crystals, collected by Hamamatsu R4125Q photomutipliers and read out by LeCroy ADCs. The LUMI can be moved away from the beam pipe about 20 cm in the horizontal direction during beam injection, tuning and before dumping to minimise radiation damages.

The luminosity measurement is based on the observation of elastic scattering of the beam positrons off the target gas electrons $e^+e^- \to e^+e^-$ (Bhabha scattering) and their annihilation into photon pairs $e^+e^- \to \gamma\gamma$. When an electron beam is used,

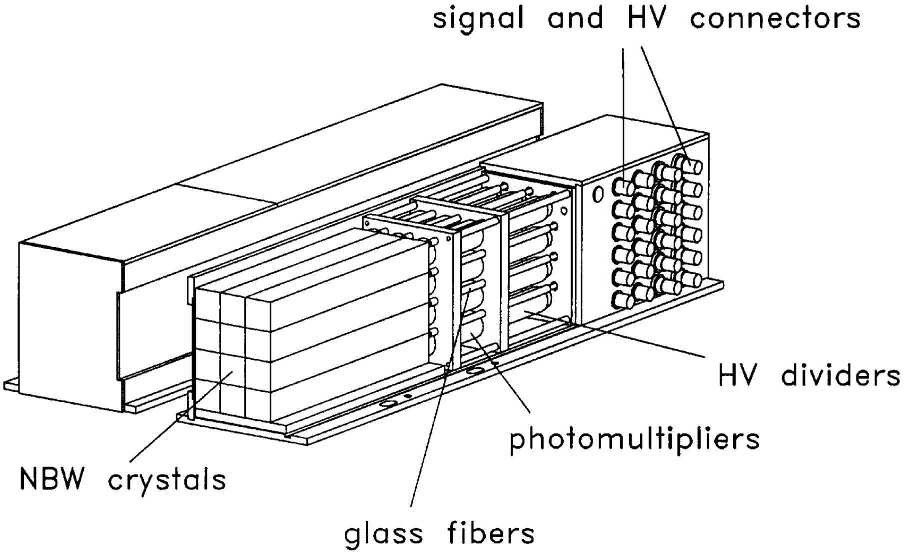

Figure 3.10: Overview of luminosity detector

electron-electron elastic scattering $e^-e^- \rightarrow e^-e^-$ (Møller scattering) is measured. The events selected are quasi symmetric Bhabha and annihilation events where each of the final state particles hits one of the calorimeters. Background is suppressed by requiring coincident hits of more than 4.5 GeV in each calorimeter. The rate of these events is proportional to the luminosity at the HERMES interaction point. Residual asymmetries from the small spin-dependence of the Bhabha cross section are corrected in the offline analysis [93]. Furthermore, the influences of beam position and beam slope drifts on the accepted events have to be taken into account.

Since the cross sections of these processes are calculable using Quantum Electrodynamics (QED) techniques and the electron density in the target is the same as the nucleon density, the luminosity can be extracted from its measurement. By measuring event rates R, the luminosity L is given as:

$$L = \frac{R}{\int_{\Delta\Omega} \mathrm{d}\Omega \epsilon (\mathrm{d}\sigma/\mathrm{d}\Omega)} \tag{3.7}$$

where ϵ is detection efficiency and the integration is performed over an acceptance angle $\Delta\Omega$. The forward scattered electrons passing an opening in the septum plate are detected by a luminosity detector [91].

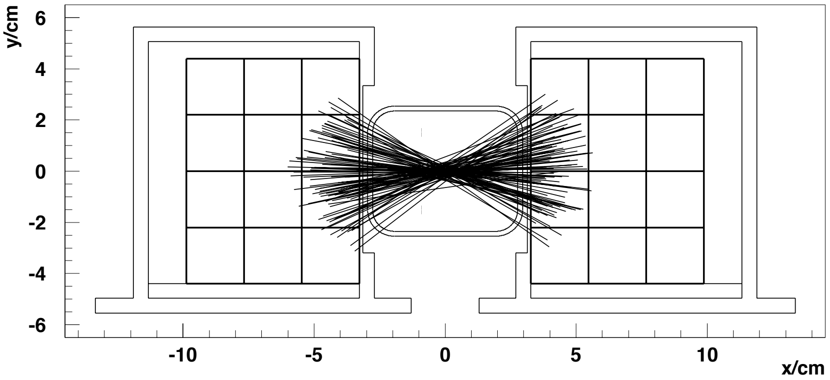

Figure 3.11: Determination of the beam position from the reconstructed impact points of the coincident events.

Because the beam position has significant influence on the luminosity monitor acceptance, it is measured by a set of beam position monitors. For physics analyses, the measured rates are corrected with respect to the beam position at the moment of the measurement [94].

The large systematic uncertainty of 6% in the measurement of absolute luminosities due to the dependence of the luminosity monitor acceptance on the beam position and slope [95] cancels in the calculation of relative luminosities. Their uncertainties are negligible.

3.5 Triggers and data acquisition

The HERMES experiment is equipped with a variety of first level triggers. Since second level triggering is not necessary at HERMES, all first level triggers of the spectrometer lead to a complete readout of the detector. Exceptions are the trigger logics of the luminosity monitor and the Longitudinal Polarimeter which activate only the readout of the corresponding components.

In order to keep the overall trigger rate low enough, most non-physics triggers are prescaled, meaning that only every second, fourth, eighth ... one is recorded. This prohibits an overload of the data acquisition due to a too high overall trigger rate.

Further information on the HERMES trigger system can be found in [96].

Trigger 21

The most important trigger at HERMES is Trigger 21, the DIS trigger, which is defined to optimise the chance of recording an event with a positron from a deep inelastic reaction. The trigger 21 is based on the following conditions that have to occur in one detector half in coincidence within the time window defined by a positron bunch crossing the interaction point:

- Hodoscope H1 and H2 give signals above threshold which is set below minimum ionising energy, so that also minimum ionising particles are triggered, allowing for a highly efficient trigger. Photons are suppressed by this condition since they do not leave signals in the scintillators.
- The Hodoscope H0 is the only trigger detector in front of the regain of the HERMES spectrometer. The signal in hodoscope H0 is required also. In addition to the suppression of photons, this condition reduces the chance of triggers caused by backward flying shower from protons originating from the proton beam.
- The sum of two adjacent calorimeter columns results in more than E_{thresh} deposited energy. This condition rejects energetic hadrons from photoproduction.

Trigger 21 is not prescaled to collect the largest DIS sample possible. For running with unpolarised target gas at high densities, the calorimeter threshold E_{thresh} was set to 3.5 GeV. For the polarised running the threshold was set to 1.4 GeV to extend the kinematic coverage of the recorded DIS events to higher values of y.

Trigger 28

The photoproduction Trigger 28 was originally implemented to detect $\mu^+\mu^-$ pairs originating from J/ψ decays [97, 98]. The trigger is designed to detect events with two tracks: one in the upper and one in the lower detector half. Trigger 28 does not require an energy deposition in the calorimeter. The following conditions have to be fulfilled for Trigger 28: time window defined by a positron bunch crossing the interaction point:

- Hodoscopes H0, H1 and H2 fire in coincidence for the top and bottom detector. This ensures two forward going tracks.
- The x-plane of BC1 must have detected a particle for the top and bottom detector. Thus, short tracks and background in the front region of the detector are suppressed. Since 1997, the second x-plane of the BC1 is added to trigger and the allowed time window for the drift chamber signals is increased. These measures significantly increase the efficiency of the trigger.
- The size of the H0 signal must not exceed the equivalent of eight minimum-ionising particles. Thus, an implicit cut on the multiplicity seen in the front detector is imposed. In 1996 this condition was slightly different since, apart from the condition on h0, additional constraints on the particle multiplicity were imposed on H1, H2 and the back chamber.

Data Acquisition

The HERMES data acquisition system is based on a Fast-Bus backbone. The LeCroy 1877 Multihit Fast-Bus TDCs (Time-to-Digital Convertor) and LeCroy 1881M Fast-Bus ADCs (Analog-to-Digital Convertor) perform the readout. The drift chambers are read out by TDCs. The magnet chambers and RICH are read out by the LeCroy PCOS IV system that is restricted to a single bit per channel.

The data from the FastBus crates are bundled by event builder modules and sent over fast optical links to a linux cluster, where they are stored on staging disks and on data tapes.

So-called slow control data, like information from the luminosity monitor, the polarimeters, the target, detector temperatures, voltage settings, etc., is recorded in addition. The slow control data are read out once every $\sim$ 10 s, independent of triggers from the spectrometer. All raw data is buffered in EPIO format on hard disk in the linux cluster and backed up regularly on data tapes. It is transferred to a taping robot at the DESY main site after the end of each HERA positron fill using a FDDI (fast distributed data interface) link.

From the electronic detector signals, the hit positions, energy depositions, etc. are determined with the HERMES decoder (HDC) using mapping, geometry and calibration of the individual detectors. All required information is stored in an ADAMO database, which is an entity-relationship database allowing structured and portable data storage. In a next step the HERMES reconstruction (HRC) program finds tracks in the spectrometer. Using a timing signal that is written to the event data and slow control data streams, both data streams can be synchronised. All synchronised data which is useful for physics analyses, is stored in data summary tables - the so-called DST files.

Different time scales are used in the HERMES data. The shortest time interval is the event containing all reconstructed tracks which are observed when a trigger is generated. All events recorded within approximately 10 s are grouped into a burst. This is the time scale on which the slow control information is synchronised to the event data. In order to split up the raw data into small enough pieces for storage, bursts are combined into a run with a size of about 450 MB. Dependent on the luminosity, a run lasts around 10 min. The longest time scale, the fill, is determined by the 8-12 h storage time of the HERA positron beam.

Chapter 4

Event selection

The analysis presented in this thesis is based on the data set collected with a longitudinal polarised deuterium target in the year 2000.

In order to minimise the systematic uncertainties and to maximise the statistical precision, the acquired data have to pass a series of selection cuts to ensure it is suitable for the extraction of double spin asymmetries and multiplicities.

4.1 Run level data quality selection

As explained in Section 3.5, the HERMES DAQ system separates the data collected within a fill in runs. When an accidental failure of a component of the detector is recorded, the corresponding runs are marked accordingly in the logbook. The rejection of these runs is the first step in the data quality selection.

4.2 Burst and record quality

Within a run, the data are subdivided in "Bursts", which correspond to approximate 10 seconds of data taking. Each burst contains the complete so called "slow control" information of the experimental status (e.g. beam and target polarisation and luminosity monitor rates) integrated over these 10 seconds.

It is obviously preferable to determine the data quality on a smaller time scale.

This is advantageous, since complete runs do not have to be rejected if a detector problem only affects a few bursts. Hence, most studies of data quality focus on this subdivision. At burst level, the quality criteria are used to reject data, due to detector instability. The following selection criteria are applied to both detector halves simultaneously. A summary of the data quality selection criteria for the analysed data sets is given in Table 4.1.

The following paragraphs detail the criteria applied for the selection of data suitable for the analysis.

Parameter	Quality Selection CriteriumCriteria
DAQ:	
Initialisation	Exclude first bursts
Efficiency	$0.7 \leq T_{\mathrm{Acc}}/T_{\mathrm{Gen}} \leq 1.0$
Record Length	$0.0\ \mathrm{s} \leq \Delta_{\mathrm{Record}} \leq 11.0$
Beam:	
Current	$5.0\ \mathrm{mA} < I_{\mathrm{B}} < 50.0\ \mathrm{mA}$
Polarimeter	OK
Polarisation	$40\% \leq \lvert P_{\mathrm{B}} \rvert \leq 80\%$
Target:	
Polarisation	$\lvert P_{\mathrm{T}} \rvert \geq 70\%$
Detector:	
HV Trips	Exclude
Calorimeter	OK
TRD	OK
Čerenkov/RICH	OK
Luminosity Rate	$5\ \mathrm{Hz} \leq \mathcal{L}_{\mathrm{fit}} \leq 50\ \mathrm{Hz}$

Table 4.1: Summary of the data quality cuts applied to the HERMES data.

4.2.1 Data acquisition conditions

The online data collection is base on the HERMES DAQ and the trigger system. A trigger is an electronic signal indicating the occurrence of a desired temporal and spatial correlation in the detector signals: B(beam) $\bigotimes$ F(final-state in detector) The purpose is to select those rare events which are relevant for the derived physics analysis and to suppress background events, to reduce 'dead time' of the data acquisition system by reducing the amount of data taking and to reduce the cost of data storage and effort the data reduction.

The dead time is the non-sensitive period of the detector, the electronics, or the readout system.

At the beginning and at the end of each run, the DAQ performs a variety of initialisation and clean up operations, which affect the information recorded in a burst. For this reason, the first burst of each run is rejected. To ensure good synchronisation between the flipping of the target state and the acquired events, the length of a record is required to be between 0 and 11 seconds. Bursts, where the ratio between the accepted triggers (T_{Acc}) and the generated triggers (T_{Gen}) were below 70% are excluded.

Both, the burst length and the life time, enter directly in the normalisation of the experimental count rates.

4.2.2 Beam conditions

A stable beam of high current and precisely measured polarisation is essential for the analysis. The minimum limitations on the beam current is $I_{\mathrm{B}} > 5\,\mathrm{mA}$, and the beam polarisation value is required to exceed 40% ($|P_{\mathrm{B}}| > 40\%$).

4.2.3 Target conditions

The burst level selection of the polarisation for the nuclear target was set to $P_{\mathrm{T}} > 70\%$ in a well-defined spin state, either parallel or anti-parallel to the beam polarisation direction. Due to the exceptionally good stability of the HERMES ABS, it is possible to use avearage values for the entire data taking period. For the year 2000 data taking period, the values used for the nuclear target polarisation were $\langle P_{z+} \rangle = 0.851$ and $\langle P_{z-} \rangle = -0.840$ [99].

4.2.4 Detector and tracking conditions

All detectors in both spectrometer halves were required to be operational. The proper functioning of the tracking system in the spectrometer is required, therefore data acquired during trips of the high voltage of the tracking chambers are rejected.

4.2.5 Luminosity

The rate in the luminosity monitor is sensitive to variations in beam current and target density. The requirement for the rate to remain within a nominal operating range ($5\text{ Hz} \leq \mathcal{L}_{\text{fit}} \leq 50\text{ Hz}$) is a test of the stability for the HERA positron beam and the target density.

4.3 Event selection

Once a data sample has been established by the data quality cuts, events originating from deep inelastic scattering processes have to be identified out of all recorded events.

The trigger requirements as described in Sect. 3.4 already enhance DIS over other competing processes. In order to further increase the purity of the DIS events sample and to discard tracks from the edges of the acceptance, cuts on geometrical and kinematic track quantities are applied as listed in Table 4.2. They will be briefly discussed in the following paragraphs.

At event level, each track that belongs to the event is considered separately. Selection criteria take care of particle identification and kinematic quantities in order to determine the DIS candidates and the semi-inclusive hadrons that are to be used for evaluation of the asymmetries. Table 4.2 summarises the criteria applied on a track-by-track level.

4.3.1 Track selection

The DIS trigger (trigger 21) preselects events that are likely to be deep-inelastic. Tracks that are part of these events are subjected to further cuts in order to ensure that they are fully inside of the spectrometer's acceptance and to identify the DIS positron and coincident semi-inclusive hadrons. The reconstruction method of the tracks called "FC only" requires a partial track in the front detector region by using front chambers (FC) only, and a back partial track by using the back chambers (BC). Tracks for which only the front partial track is available (short tracks) were excluded.

4.3.2 Geometry requirements

The geometry selection criteria ensure that the particle originated from an interaction with the gas inside the cell and passed through all the detectors of the spectrometer.

The particle trajectories were required to be contained within the fiducial volume of the spectrometer. This condition guarantees a proper track reconstruction and identification also for those particles whose trajectories are close to the edges of the acceptance.

Additionally, the position of the particle trajectory at the calorimeter was selected to be within $|x_{calo}| \leq 175$ cm and $30\,\text{cm} \leq |y_{calo}| \leq 100\,\text{cm}$. These criteria ensure an optimal cluster energy reconstruction and negligible energy loss outside the calorimeter volume for the selected tracks.

4.3.3 Particle identification

As explained in Section 3.4, the relevant quantities for particle identification are the expressions PID3 + PID5 for the data sets, which refer to the summed likelihood parameter from the various PID detectors. For each track, the corrected probability is derived by subtracting from the value of the flux ratio $\log_{10}\Phi(p,\theta)$ from the PID term, where momentum p and angle θ are specific for the track. The separation of leptonic tracks from charged hadronic tracks was performed as follows

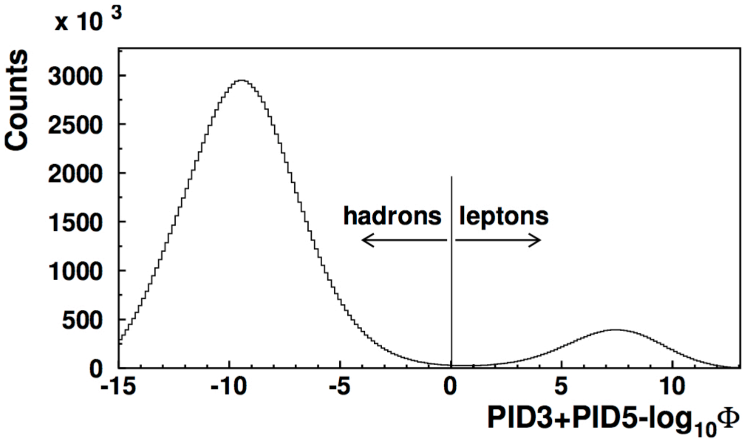

Figure 4.1: The Distribution of the PID variables.

$$\text{Leptons}: 100.0 \geq \mathrm{PID}_3 + \mathrm{PID}_5 - \log\phi > 0.0; \tag{4.1}$$

$$\text{Hadrons}: \quad 0.0 \geq \mathrm{PID}_3 + \mathrm{PID}_5 - \log\phi \geq -100.0 \tag{4.2}$$

DIS leptons were further selected in each event by applying the kinematic DIS criteria to the leptonic track. In coincidence with the DIS lepton, hadrons that passed the kinematic criteria are selected for the formation of the semi-inclusive asymmetries for each event. A cut on the quality parameter $rQp > 0.0$ was applied for RICH detector.

4.3.4 Kinematic selection criteria for DIS events and semi-inclusive hadrons

After leptonic tracks have been discriminated from hadronic tracks, the scattered positrons from the DIS processes were selected applying kinematic criteria that define the phase-space associated with the deep-inelastic scattering events.

At this point of the selection, no distinction was made between electrons and positrons, as electrons measure charge-symmetric background in the positron sample for a positron beam. The electrons and positrons are all taken into accounts, even if there are more than one lepton that fulfils the DIS cuts. Each lepton is treated

Track Selection
Trigger pattern T21 fired
Method of reconstruction NOVC
The momentum of Track $P > 0.5$ GeV
Full tracks only

Geometry requirements	
Position at the Calorimeter	$\lvert x_{calo} \rvert \leq 175$ cm 30 cm $\leq \lvert y_{calo} \rvert \leq 100$ cm.
Longitudinal vertex position	Lepton : $\lvert z_{vertex} \rvert \leq 18$ cm Hadron : $-$ 20 cm $\leq z_{vertex} \leq 18$ cm
Transverse vertex position	Lepton :$\lvert d_{vertex} \rvert \leq 0.75$ cm
DIS Selection (lepton)	
PID	$0.0 < \mathrm{PID}_3 + \mathrm{PID}_5 \leq 100.0$
Calorimeter cluster energy	$E_{Calo} \geq 3.5$ GeV
Momentum transfer	$Q^2 \geq 1.0$ GeV^2
Invariant mass	$W^2 \geq 10.0$ GeV^2
Fractional energy transfer	$y \leq 0.85$
Hadrons Selection	
PID	$-100.0 \leq \mathrm{PID}_3 + \mathrm{PID}_5 \leq 0.0$
Method of reconstruction(RICH)	IRT, rQp ≥ 0.
Hadron energy fraction	$z \geq 0.1$
Feynman variable	$x_F \geq 0.1$
Momentum of hadrons	2.0 GeV $\leq P \leq 15.0$ GeV

Table 4.2: Summary of the kinematic cuts used in this analysis to select the inclusive and semi-inclusive events.

as separate event for the determination of the kinematic variables x, y, Q^2 and W^2. These kinematic variables are calculated from the particle momenta and the scattering angles.

An upper limit of $y \leq 0.85$ suppresses radiative corrections to the cross section. The criterion on the invariant mass of the final hadronic state, $W^2 \geq 10\,\mathrm{GeV}^2$, was used to select the deep-inelastic region, where the nucleon breaks apart incoherently. The requirement $Q^2 \geq 1\,\mathrm{GeV}^2$ allows the modelling of the events within the perturbative QCD framework, and it also suppresses higher twist effects.

These requirements define a base sample of inclusive DIS candidates. In this analysis the events are extracted as function of x. The binning in x consists of eight bins with the limits given in Tab. 4.3. The binning was chosen to approximately yield the same number of events in each bin.

For the semi-inclusive analysis, the hadrons in the event in coincidence with the DIS candidate were selected.

	x-range	$< x >$	$< Q^2 >$	$< y >$
1	$0.023 \cdots 0.040$	0.033	1.222	0.725
2	$0.040 \cdots 0.055$	0.047	1.489	0.609
3	$0.055 \cdots 0.075$	0.065	1.743	0.523
4	$0.075 \cdots 0.100$	0.087	2.013	0.449
5	$0.100 \cdots 0.140$	0.118	2.413	0.396
6	$0.140 \cdots 0.200$	0.166	3.225	0.376
7	$0.200 \cdots 0.300$	0.239	4.519	0.371
8	$0.300 \cdots 0.700$	0.360	7.134	0.381

Table 4.3: Definition of the binning in x. The first column gives the ordinal number of each bin, with the limits defined in the second column. In the third column the mean value $< x >$ is given.

Chapter 5

K_s^0 production in deep inelastic scattering at HERMES

Due to the short life time of the K_s^0 of $\tau = 8.9$ns, these particles are identified in the HERMES spectrometers by their decay produces in the channel $K_s^0 \rightarrow \pi^+\pi^-$.

5.1 The K_s^0 candidates finding algorithm

In this analysis, the K_s^0 mesons are reconstructed using the decay channel $K_s^0 \rightarrow \pi^+\pi^-$ which has a branching ratio of about 69% [100]. Tracks of opposite charged are paired together. Each track had to fulfil the event selection criteria which are introduced in Chapter 4. After applying this procedure to the hadronic event sample and assigning the pion mass to both tracks, the mass distribution of the reconstructed K_s^0 decay is shown in Fig. 5.1 assuming both tracks to be pions.

At the same time, the parameters $c \cdot \tau$ and $\cos(\gamma)$ are calculated as shown below, which are used to suppress the background which did not come from the decay mode $K_s^0 \rightarrow \pi^+\pi^-$.

5.2 K_s^0 identification and background suppression

In order to get a clear K_s^0 signal and to enhance the K_s^0 signal-to-background ratio, additional cuts have been introduced. The cuts are based on the event topology shown in Fig. 5.1. The position of the decay vertex and the distance of the closet approach (DCA) $D2$ of the pion tracks have been calculated. The tracks of particles which are produced by the decay of the same parent particle are supposed to come from the same vertex. This is, in the analysis, expressed for two pion tracks by the cut $D2$:

$$D2_{(\pi^+\pi^-)} < 1\text{cm} \tag{5.1}$$

The next topology cut utilises the knowledge of the mean life time of the K_s^0(8.9 ns). For a K_s^0 with a momentum of 1 GeV/c, the mean life time corresponds to a flight distance of approximately 10 cm. In order to estimate the decay length of a potential K_s^0, its track and production vertex has been reconstructed. Then, the distance $d12$

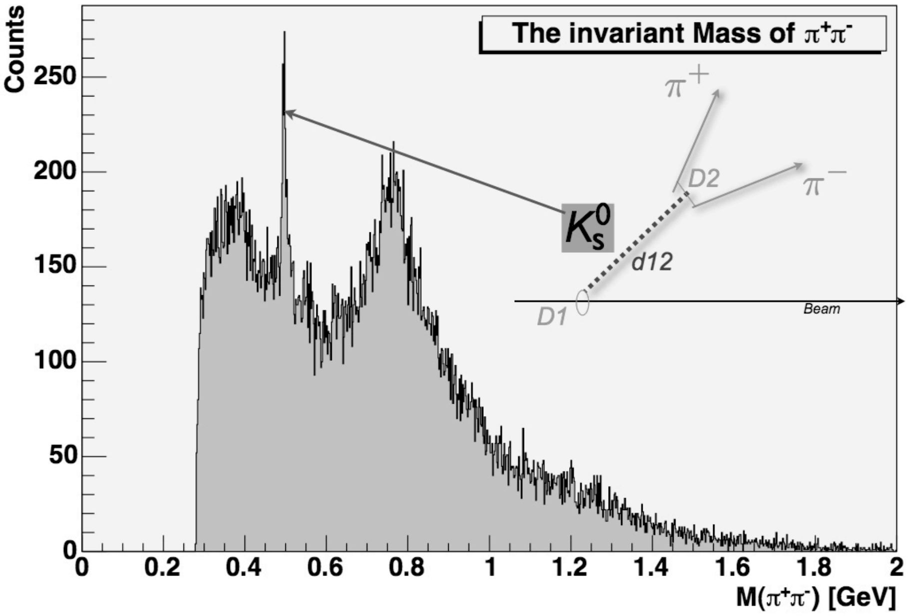

Figure 5.1: Invariant mass distribution of reconstructed $\pi^+\pi^-$ candidate events. The topology of reconstructed event.

is:

$$d12 = |V_{D1} - V_{D2}| \tag{5.2}$$

The following parameter has been introduced to be an important cut:

$$c \cdot \tau = \frac{M_{K_s^0} \cdot d12}{P_{K_s^0}} \tag{5.3}$$

The direction of the K_s^0 track is given by the sum of the two pion's three-momenta vectors. The K_s^0 production vertex has been reconstructed using the assumption that the K_s^0 and the beam and scattering positron come from the same production vertex. There is an angle γ, which is the angle between direction of K_s^0 momentum and the direction from vertex $D2$ to the beam and scattering vertex which has to be close to zero ($D2_{(\pi^+\pi^-)} <$ 1cm is used in this analysis).

$$\cos\gamma > 0.99 \tag{5.4}$$

	K_s^0 selection
mean life time	$c \cdot \tau < 10.0$
deviation from beam scattering vertex	$\cos\gamma > 0.99$

Table 5.1: Summary of the cuts used in the selection of K_s^0 sample

Using these criteria (summarised in Tab. 5.1), the background in the mass region of the K_s^0 is reduced and the K_s^0 signal is shown in Fig. 5.2.

To determine mass and width of the K_s^0, the distribution of the $\pi^+\pi^-$ mass spectrum was fitted with a Gaussian shape and a polynomial expression for the background in the region 0.4 to 0.6 GeV (shown in Fig 5.2). The measured K_s^0 mass value obtained is $(497.3 \pm 0.1)\mathrm{MeV}/c^2$, in reasonable agreement with the world average of $(497.672 \pm 0.031)\mathrm{MeV}/c^2$ [100]. The width obtained, $\sigma = (7.0 \pm 0.1)\mathrm{MeV}/c^2$, corresponds to our experimental mass resolution. The value of mass and the width of the signal are well reproduced by the HERMES Monte Carlo simulations. In the signal region extends from 480 to 515 MeV, total of 5596 K_s^0 mesons on top of a background

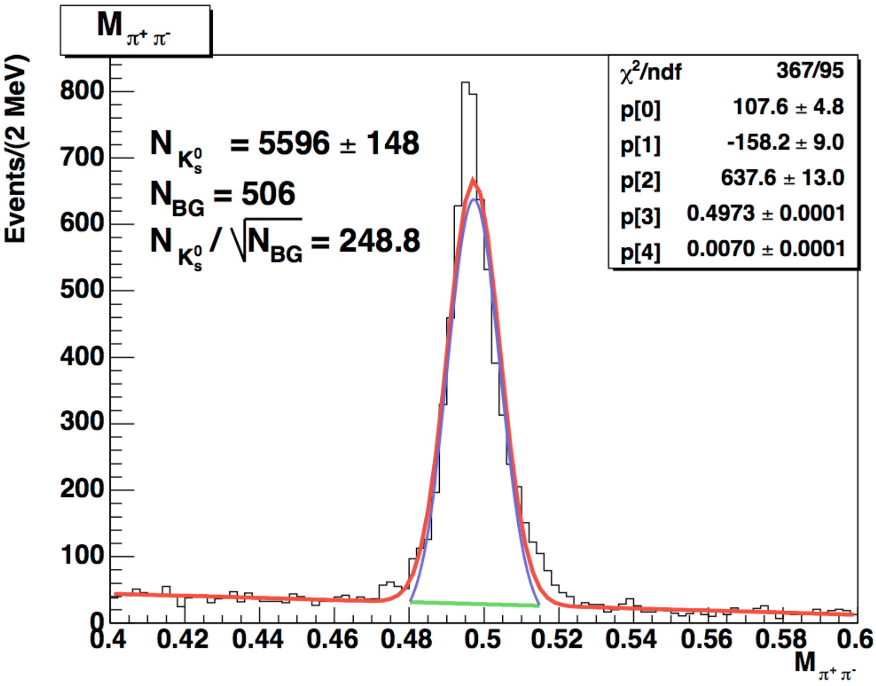

Figure 5.2: The $\pi^+\pi^-$ invariant mass distribution of reconstructed K_s^0 candidate events after selections and cuts. The green line indicates the selected mass interval.

of about 506 $\pi^+\pi^-$-combinations was obtained. The peak contains 5596 ± 148 K_s^0 mesons. All errors are statistical only.

Chapter 6

Double spin asymmetries

6.1 Determination of the double spin asymmetries

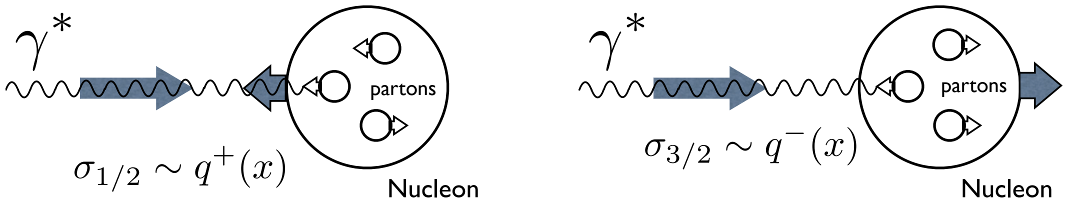

Figure 6.1: representation of the orientations of spin

The longitudinal double spin asymmetry $A_{||}(x, Q^2)$ in the laboratory system is defined as the difference of the cross sections for anti-parallel and parallel alignments of the beam and target spins, normalised to the sum of these two cross sections.

$$A_{||}(x, Q^2) = \frac{\sigma^{\overset{\rightarrow}{\Leftarrow}} - \sigma^{\overset{\rightarrow}{\Rightarrow}}}{\sigma^{\overset{\rightarrow}{\Leftarrow}} + \sigma^{\overset{\rightarrow}{\Rightarrow}}} \tag{6.1}$$

The unpolarised cross section $\bar{\sigma} = (\sigma^{\overset{\rightarrow}{\Leftarrow}} + \sigma^{\overset{\rightarrow}{\Rightarrow}})/2$ equals the average of the polarised cross sections. Using this, the polarised cross sections can be rewritten as

$$\sigma^{\overset{\rightarrow}{\Leftarrow}(\overset{\rightarrow}{\Rightarrow})} = \bar{\sigma}(x, Q^2)[1 \;_{(}\pm_{)}\; A_{||}(x, Q^2)] \tag{6.2}$$

The measured experimental asymmetry $A_{||}^{\exp}(x, Q^2)$ is proportinal to asymmetry $A_{||}(x, Q^2)$:

$$A_{||}^{\mathrm{exp}}(x,Q^2) = f \cdot P_{\mathrm{B}} \cdot P_{\mathrm{T}} \cdot A_{||}(x,Q^2) \qquad (6.3)$$

where f is the target dilution factor and P_{B} and P_{T} denotes the beam and target polarisations, respectively. The target dilution factor f represents the fraction of nucleons in the target which are polarised. For the polarised pure gas target at HERMES $f = 1$, which is unique compared to all other previous experiments on polarised DIS. Other experiments (SMC [25], E143 [45], etc.) use polarised solid state targets with dilution factor in the range of $f \approx 0.04 \rightarrow 0.2$, thereby reducing the size of their measured experimental asymmetries significantly. As the present analysis only deals with data taken on a polarised deuteron target, f is neglected from here on.

The total number of the events measured per spin state, $N^{\overset{\rightarrow}{\Leftarrow}(\overset{\rightarrow}{\Rightarrow})}(x,Q^2)$, is related to the unpolarised cross section $\bar{\sigma}(x,Q^2)$ and the asymmetry $A_{||}(x,Q^2)$ by

$$\begin{aligned} N^{\overset{\rightarrow}{\Leftarrow}(\overset{\rightarrow}{\Rightarrow})}(x,Q^2) &= \bar{\sigma}(x,Q^2) \int_{\overset{\rightarrow}{\Leftarrow}(\overset{\rightarrow}{\Rightarrow})} \Gamma(t,x,Q^2) \cdot \mathcal{E}(t,x,Q^2) \cdot \mathcal{L}(t)[1 \pm P_{\mathrm{B}} P_{\mathrm{T}} A_{||}(x,Q^2)]\mathrm{d}t \\ &\simeq \bar{\sigma}(x,Q^2)\Gamma(t,x,Q^2) \cdot \mathcal{E}_{\mathrm{rec}}(t,x,Q^2) \int_{\overset{\rightarrow}{\Leftarrow}(\overset{\rightarrow}{\Rightarrow})} \mathcal{E}_{\mathrm{DAQ}}(t,x,Q^2) \cdot \mathcal{L}(t)[1 \pm P_{\mathrm{B}} P_{\mathrm{T}} A_{||}(x,Q^2)]\mathrm{d}t \end{aligned} \qquad (6.4)$$

Where the integration is performed over time periods with anti-parallel (parallel) spin states. $\mathcal{L}$ denotes the luminosity delivered per spin state and the beam and target polarisations account for dilution of the experimental asymmetry $A_{||}^{\mathrm{exp}}$ as given in Eq. 6.3 .

$\Gamma(t,x,Q^2) \simeq \Gamma(x,Q^2)$ in Eq. 6.4 represents the geometrical acceptance function, which is independent of the relative orientation of the beam and target spins. Furthermore, it is assumed to be nearly independent of the time t. This assumption is justified by the fact that the experimental setup is essentially left unchanged during one year of data taking. The quantity $\mathcal{E}(t,x,Q^2)$ in Eq. 6.4 is the detection efficiency, which is the product of the reconstruction efficiency $\mathcal{E}_{\mathrm{rec}}(x,Q^2)$, which may vary over the geometrical acceptance of the spectrometer, and the trigger efficiency $\mathcal{E}_{\mathrm{DAQ}}(x,Q^2)$

may vary on the time scale of the burst and is related to the fractional dead time δ_{Dead}, defined in equation,

$$\delta_{\mathrm{Dead}} = 1 - \frac{N_{\mathrm{accepted}}}{N_{\mathrm{generated}}} = \frac{N_{\mathrm{rejected}}}{N_{\mathrm{generated}}} \tag{6.5}$$

by $\mathcal{E}_{\mathrm{DAQ}}(t) = 1 - \delta_{\mathrm{Dead}}$. Time dependent variations of the reconstruction efficiency $\mathcal{E}_{\mathrm{rec}}$ are small and happen on a time scale which is much longer than the duration of one target spin cycle. In [101] the effect of these small variations on the extracted inclusive proton asymmetry was investigated and found to be negligible. The trigger efficiency $\mathcal{E}_{\mathrm{DAQ}}$ is totally uncorrelated to the kinematics of the scattering process and hence is independent of x and Q^2.

Rewriting the integrals over the luminosity for a given burst i as

$$\ell_i^{\overset{\rightarrow}{\Leftarrow}(\overset{\rightarrow}{\Rightarrow})} = \int_{\overset{\rightarrow}{\Leftarrow}(\overset{\rightarrow}{\Rightarrow})_{\mathrm{i}}} \mathcal{E}_{\mathrm{DAQ}(t)} \mathcal{L}(t) \mathrm{d}t \tag{6.6}$$

$$\ell_{p_i} i^{\overset{\rightarrow}{\Leftarrow}(\overset{\rightarrow}{\Rightarrow})} = \int_{\overset{\rightarrow}{\Leftarrow}(\overset{\rightarrow}{\Rightarrow})_i} \mathcal{E}_{\mathrm{DAQ}(t)} \mathcal{L}(t) P_{\mathrm{B}} P_{\mathrm{T}} \mathrm{d}t \tag{6.7}$$

the number of events $n_i^{\overset{\rightarrow}{\Leftarrow}(\overset{\rightarrow}{\Rightarrow})}(x, Q^2)$ in this burst can be expressed as

$$n_i^{\overset{\rightarrow}{\Leftarrow}(\overset{\rightarrow}{\Rightarrow})}(x, Q^2) = \bar{\sigma}(x, Q^2) \Gamma x, Q^2 \mathcal{E}(x, Q^2) \left(\ell_i^{\overset{\rightarrow}{\Leftarrow}(\overset{\rightarrow}{\Rightarrow})} \pm \ell_{p_i}^{\overset{\rightarrow}{\Leftarrow}(\overset{\rightarrow}{\Rightarrow})} A_{||}(x, Q^2) \right) \tag{6.8}$$

When summing over all bursts and using the following definitions

$$N^{\overset{\rightarrow}{\Leftarrow}(\overset{\rightarrow}{\Rightarrow})} = \sum_i n_i^{\overset{\rightarrow}{\Leftarrow}(\overset{\rightarrow}{\Rightarrow})} \tag{6.9}$$

$$L^{\overset{\rightarrow}{\Leftarrow}(\overset{\rightarrow}{\Rightarrow})} = \sum_i \ell_i^{\overset{\rightarrow}{\Leftarrow}(\overset{\rightarrow}{\Rightarrow})} \tag{6.10}$$

$$L_p^{\overset{\rightarrow}{\Leftarrow}(\overset{\rightarrow}{\Rightarrow})} = \sum_i \ell_{p_i}^{\overset{\rightarrow}{\Leftarrow}(\overset{\rightarrow}{\Rightarrow})} \tag{6.11}$$

the time averaged asymmetry $A_{||}$ can be related to the total event numbers $N^{\overset{\rightarrow}{\Leftarrow}(\overset{\rightarrow}{\Rightarrow})}$ in each state by

$$A_{||} = \frac{N^{\overset{\rightarrow}{\Leftarrow}} L^{\overset{\rightarrow}{\Rightarrow}} - N^{\overset{\rightarrow}{\Rightarrow}} L^{\overset{\rightarrow}{\Leftarrow}}}{N^{\overset{\rightarrow}{\Leftarrow}} L_p^{\overset{\rightarrow}{\Rightarrow}} + N^{\overset{\rightarrow}{\Rightarrow}} L_p^{\overset{\rightarrow}{\Leftarrow}}} \tag{6.12}$$

where the unpolarised cross section $\bar{\sigma}(x, Q^2)$ and the efficiences $\Gamma(x, Q^2)$ and $\mathcal{E}_{\mathrm{rec}}(x, Q^2)$ cancel out. The explicit dependence of $A_{||}$ and $N^{\overset{\rightarrow}{\Leftarrow}(\overset{\rightarrow}{\Rightarrow})}$ on the kinematic quatities x and Q^2 has been omitted in these expressions.

The measured inclusive double spin asymmetry $A^e_{||}$ derived from the equation 6.13

$$A^e_{||}(x) = \frac{N^{e\overset{\rightarrow}{\Leftarrow}}(x) L^{\overset{\rightarrow}{\Rightarrow}} - N^{e\overset{\rightarrow}{\Rightarrow}}(x) L^{\overset{\rightarrow}{\Leftarrow}}}{N^{e\overset{\rightarrow}{\Leftarrow}}(x) L_p^{\overset{\rightarrow}{\Rightarrow}} + N^{e\overset{\rightarrow}{\Rightarrow}}(x) L_p^{\overset{\rightarrow}{\Leftarrow}}} \tag{6.13}$$

is shown in Fig. 6.2 and the relative kinematic factors are shown in Tab. 6.1.

And the measured semi-inclusive double spin asymmetry $A^{K^0_s}_{||}$ derived from the equation 6.14

$$A^{K^0_s}_{||}(x) = \frac{N^{K^0_s\overset{\rightarrow}{\Leftarrow}}(x) L^{\overset{\rightarrow}{\Rightarrow}} - N^{K^0_s\overset{\rightarrow}{\Rightarrow}}(x) L^{\overset{\rightarrow}{\Leftarrow}}}{N^{K^0_s\overset{\rightarrow}{\Leftarrow}}(x) L_p^{\overset{\rightarrow}{\Rightarrow}} + N^{K^0_s\overset{\rightarrow}{\Rightarrow}}(x) L_p^{\overset{\rightarrow}{\Leftarrow}}} \tag{6.14}$$

is shown in Fig. 6.3 and the relative kinematic factors are shown in Tab. 6.2.

6.2 The corrections to double spin asymmetries

Assuming the correction factors are same to the parallel ($\overset{\rightarrow}{\Rightarrow}$) and anti-parallel ($\overset{\rightarrow}{\Leftarrow}$), the corrections to the double spin asymmetries cancel according to the formula. Therefor no corrections were applied to the DSA. This assumption is justified by the fact that a previous analysis result for charged kaons with the same data set [102] show very small correction compared with the statistical errors and the systematic uncertainty.

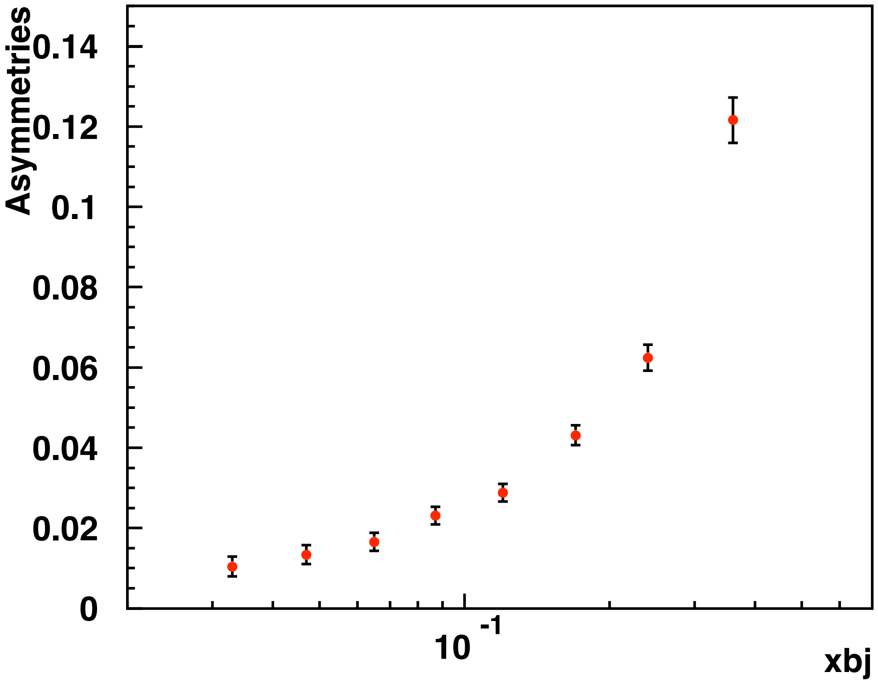

Figure 6.2: Double spin asymmetries of inclusive DIS.

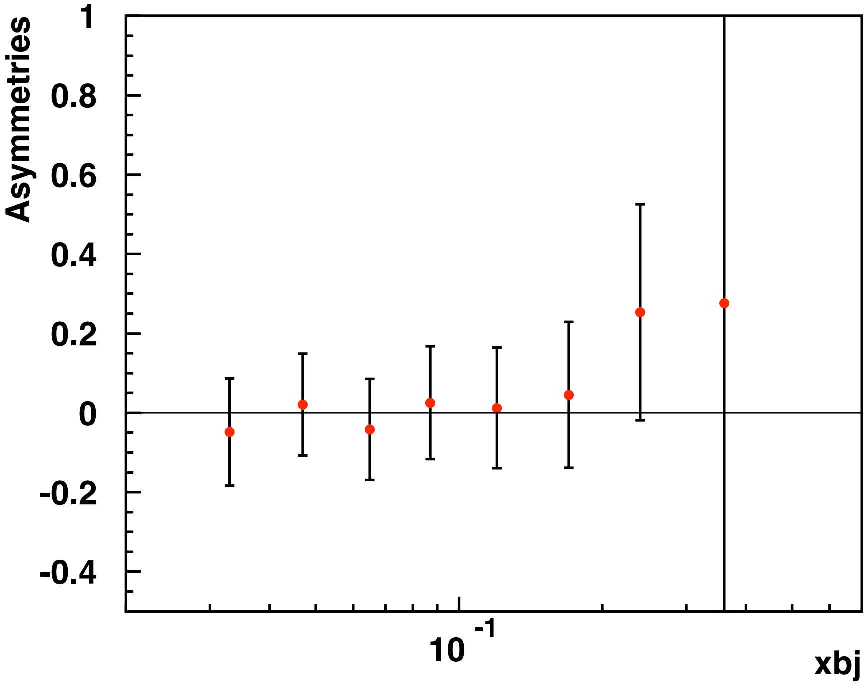

Figure 6.3: Double spin asymmetries of semi-inclusive K_s^0 production.

	$< x >$	η	γ	D	R	δR
1	0.033	0.024	0.056	0.720	0.379	0.028
2	0.047	0.042	0.074	0.593	0.358	0.025
3	0.065	0.062	0.095	0.504	0.335	0.022
4	0.087	0.086	0.120	0.432	0.309	0.019
5	0.118	0.114	0.150	0.384	0.275	0.015
6	0.165	0.139	0.181	0.376	0.222	0.011
7	0.239	0.166	0.216	0.386	0.159	0.008
8	0.360	0.194	0.257	0.415	0.100	0.006

Table 6.1: The kinematic factors extracted from HERMES 2000 polarised deuteron data set are used to evaluate the virtual photon asymmetries.

	$< x >$	η	γ	D	R	δR
1	0.033	0.024	0.056	0.728	0.378	0.028
2	0.047	0.037	0.071	0.639	0.354	0.024
3	0.065	0.048	0.086	0.611	0.320	0.021
4	0.087	0.061	0.103	0.589	0.278	0.017
5	0.118	0.075	0.123	0.583	0.228	0.014
6	0.166	0.093	0.148	0.580	0.172	0.010
7	0.238	0.119	0.182	0.558	0.125	0.008
8	0.352	0.149	0.224	0.557	0.083	0.006

Table 6.2: The kinematic factors extracted from the HERMES 2000 polarised deuteron data set used to evaluate the semi-inclusive K_s^0 asymmetries.

6.3 The photon-nucleon asymmetries

The asymmetry of interest in the analysis is photon-nucleon asymmetry A_1 . It is related to measured asymmetry $A_{||}$ which are extracted from 2000 polarised deuteron data with all kinematic factors in last few sections:

$$A_1 = \frac{A_{||}}{D(1+\eta\gamma)} - \frac{\eta\gamma(1+\gamma^2)}{1+\eta\gamma}\frac{g_2}{F_1} \overset{g_2=0}{\simeq} \frac{A_{||}}{D(1+\eta\gamma)} \tag{6.15}$$

as

$$A_1 = \frac{1}{(1+\eta\gamma)} \cdot \frac{N^{\overset{\rightarrow}{\Leftarrow}} L^{\overset{\rightarrow}{\Rightarrow}} - N^{\overset{\rightarrow}{\Rightarrow}} L^{\overset{\rightarrow}{\Leftarrow}}}{N^{\overset{\rightarrow}{\Leftarrow}} L^{\overset{\rightarrow}{\Rightarrow}} D^{\overset{\rightarrow}{\Rightarrow}} + N^{\overset{\rightarrow}{\Rightarrow}} L^{\overset{\rightarrow}{\Leftarrow}} D^{\overset{\rightarrow}{\Leftarrow}}} \tag{6.16}$$

where the kinematic factors, η, γ, and D, are defined as

$$D = \frac{1-(1-y)\varepsilon}{1+\varepsilon R} \tag{6.17}$$

$$\eta = \frac{\varepsilon\gamma y}{1-(1-y)\varepsilon} \tag{6.18}$$

$$\xi = \sqrt{\frac{2\varepsilon}{1+\varepsilon}} \tag{6.19}$$

$$\gamma^2 = \frac{Q^2}{\nu^2} = \frac{4M^2x^2}{Q^2} \tag{6.20}$$

D counts for the depolarisation of the virtual photon with respect to the polarisation of the positron beam. $R = \sigma_{\mathrm{L}}/\sigma_{\mathrm{T}}$ is the ratio of the longitudinal to the transverse polarisation of the virtual photon. To account for slightly different values for the depolarisation factor D in the different spin states due to binning effects, D is evaluated for each target spin state separately.

The photon-nucleon asymmetries, A_1^d and $A_1^{K_s^0}$, are presented in Fig. 6.4 and Fig. 6.5. These asymmetries will be used in the chapter 8 to extract the strange and the non strange polarisation.

The statistical uncertainty δA_1 on the asymmetry A_1 is obtained from the statistical uncertainties $\delta N = \sqrt{N}$ on the event numbers as

$$\begin{aligned}
\delta A_1 &= \sqrt{\left(\frac{\partial A_1}{\partial N^{\overset{\rightarrow}{\Rightarrow}}}\delta N^{\overset{\rightarrow}{\Rightarrow}}\right)^2 + \left(\frac{\partial A_1}{\partial N^{\overset{\rightarrow}{\Leftarrow}}}\delta N^{\overset{\rightarrow}{\Leftarrow}}\right)^2} \qquad (6.21)\\
&= \frac{1}{(1+\eta\gamma)} \cdot \frac{L^{\overset{\rightarrow}{\Leftarrow}} L_p^{\overset{\rightarrow}{\Rightarrow}} D^{\overset{\rightarrow}{\Rightarrow}} + L^{\overset{\rightarrow}{\Rightarrow}} L_p^{\overset{\rightarrow}{\Leftarrow}} D^{\overset{\rightarrow}{\Leftarrow}}}{\left(N^{\overset{\rightarrow}{\Leftarrow}} L^{\overset{\rightarrow}{\Rightarrow}} D^{\overset{\rightarrow}{\Rightarrow}} + N^{\overset{\rightarrow}{\Rightarrow}} L^{\overset{\rightarrow}{\Leftarrow}} D^{\overset{\rightarrow}{\Leftarrow}}\right)^2} \sqrt{\left(N^{\overset{\rightarrow}{\Rightarrow}}\right)^2 N^{\overset{\rightarrow}{\Leftarrow}} + \left(N^{\overset{\rightarrow}{\Leftarrow}}\right)^2 N^{\overset{\rightarrow}{\Rightarrow}}}
\end{aligned}$$

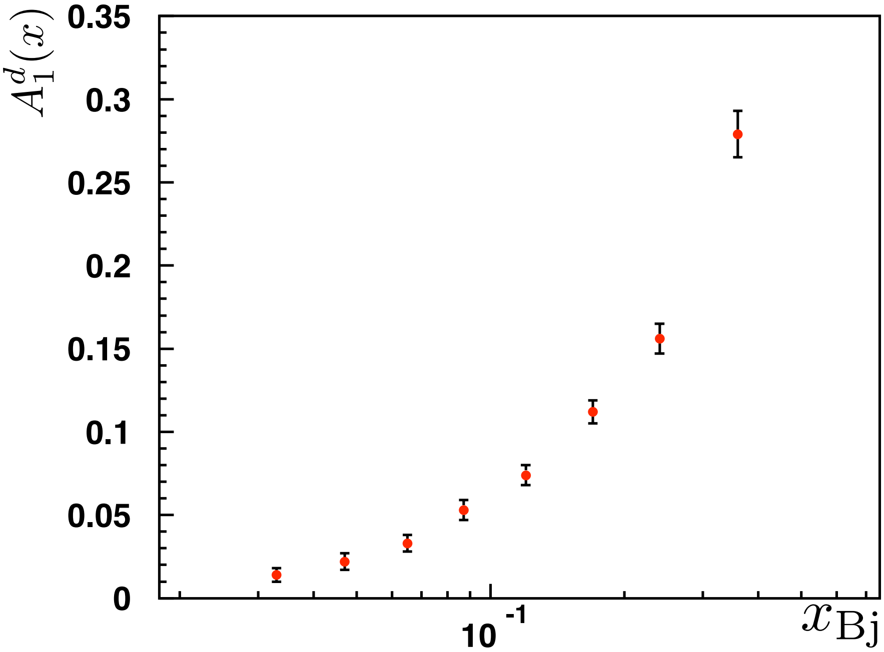

Figure 6.4: The photon-nucleon spin asymmetries of DIS

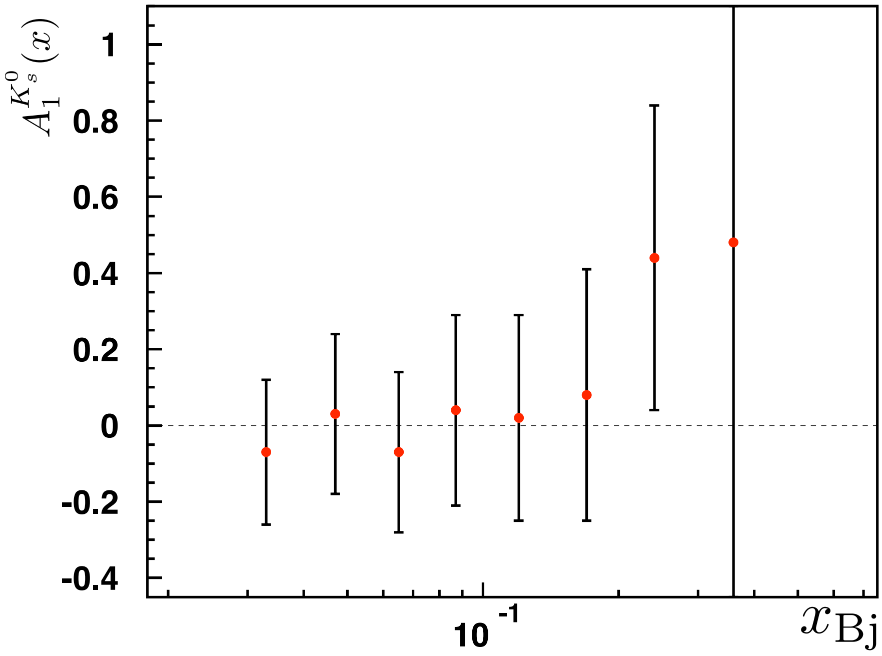

Figure 6.5: The semi-inclusive K_s^0 photon-nucleon asymmetries

This expression is valid under the assumption of a Poisson distribution for the number of scattering events and for experimental asymmetries which are not too close to one.

The semi-inclusive asymmetries A_1^h are extracted in complete analogy to the procedure for the inclusive asymmetry A_1. In case of the semi-inclusive asymmetries, the event number in the above expressions have to be substituted by $N_h^{\overrightarrow{\Leftarrow}(\overrightarrow{\Rightarrow})}$, which denote the number of events with hadron of type h in coincidence with positron. More specifically, if more than one hadron passes the selection cuts explained in Chapter 4, the event is counted multiply, once for each hadron passing the cuts.

6.4 Systematic uncertainty

The contributions to the systematic uncertainty in $A_1^{(h)}$ have different sources and are outlined in this section. The errors related to the HERMES experiment comprise the systematic uncertainties in the beam and target polarisation measurements. Additional systematic uncertainties in $A_1^{(h)}$ are related to external contributions such as the uncertainties in the measurements of the cross section ratio R and the spin structure function g_2. In the following, the formulae of the individual contributions to the systematic uncertainty on the inclusive and semi-inclusive asymmetries will be discussed, and explicitly stated, they hold in the same way for both inclusive and semi-inclusive asymmetries.

The error in each contributing term was added in quadrature to evaluate the total systematic uncertainty in the final asymmetry measurement.

6.4.1 Beam polarisation uncertainty

Measurements from the longitudinal polarimeter were used instead for the 2000 data. The associated fractional uncertainties are $[\delta P_B/P_B]_{(2000)} = 1.9\%$. The systematic uncertainty in the asymmetry A_1 from this contribution is given by

$$[\delta A_1]_{p_B} = \sqrt{\left(\frac{\partial A_1}{\partial P_B}\right)^2 (\delta P_B)^2} = \left| A_1 \cdot \frac{\delta P_B}{P_B} \right| \tag{6.22}$$

6.4.2 Target polarisation uncertainty

The associated systematic uncertainties in the measurement of the target polarisation for the 2000 data set are $[\delta P_T/P_T]_{2000} = 4.0\%$. For this year the systematic uncertainty in the asymmetries was calculated according to

$$[\delta A_1]_{p_T} = \sqrt{\left(\frac{\partial A_1}{\partial P_T}\right)^2 (\delta P_T)^2} = \left| A_1 \cdot \frac{\delta P_T}{P_T} \right| \tag{6.23}$$

6.4.3 Model for the spin structure function g_2

In the derivation of Eq.6.15, the structure function $g_2(x)$ was assumed to be zero which leads to $A_1^{(h)} = g_1^{(h)}/F_1^{(h)}$. For a non-vanishing spin structure function $g_2^{(h)}(x)$ this relation breaks up and the resulting expressions become

$$A_1^{(h)} = \frac{A_{||}^{(h)}}{D(1+\eta\gamma)} - \frac{\eta\gamma(1+\gamma^2)}{1+\eta\gamma}\frac{g_2^{(h)}}{F_1^{(h)}} \tag{6.24}$$

The spin structure functions $g_2(x)$ has been measured for the proton [45, 24] and for the neutron [22] in a range of x and Q^2 similar to the HERMES experiment. The data are consist with $g_2(x) = 0$ within statistical uncertainties.

In order to estimate the systematic uncertainty on the asymmetry A_1 due to the assumption $g_2(x) = 0$, a simple limiting parametrisation was chosen:

$$xg_2^p(x) = \pm 0.055 \cdot (1-x)^{0.7} \tag{6.25}$$

$$xg_2^d(x) = \pm 0.065 \cdot (1-x)^{0.98} \tag{6.26}$$

$$xg_2^n(x) = \pm 0.110 \cdot (1-x)^{0.98} \tag{6.27}$$

For $x \to 1$ these parametrisations follow the behaviour of the twist-2 Wanzura-Wilczek term $xg_2^{WW}(x)$ which approaches zero in this limit.

Using this parametrisation, the systematic uniceratinty on the asymmetry A_1 6.24 can be expressed as:

$$[\delta A_1]_{g_2} = \left| \frac{\eta\gamma(1+\gamma^2)}{1+\eta\gamma} \left(\frac{g_2}{F_1} \right) \right| \tag{6.28}$$

for deuteron asymmetries. The semi-inclusive asymmetries are assumed to have the same systematic uncertainty as the measured uncertainty in the inclusive case.

6.4.4 Uncertainty in the parametrisation of R

The ratio $R = \sigma_L/\sigma_T$ of the longitudinal (σ_L) and transverse (σ_T) photon absorption cross sections enters the asymmetry calculation through the depolarisation factor D (see Eq. 6.18). The uncertainty, δR, of the world-averaged parametrisation of R is presented in Ref. [26] and contributes to the measured asymmetries as

$$[\delta A_1]_R = \frac{\epsilon}{1+\epsilon R} A_1 \delta R \tag{6.29}$$

6.4.5 Smearing and radiative corrections uncertainties

Based on the Eq. 6.12, and the fact that the previous analysis results of charged kaons showed almost no corrections for smearing and radiative effects, as discussed in section 6.2, these corrections for double spin asymmetries are neglected in this work. This neglections results in an uncertainty in the photo-nucleon asymmetries which is estimated to be of the same size as the corrections which have been applied in the analysis of the charged kaon asymmetries [102]

$$[\delta A_1]_{K_{\text{smear}}} = |\Delta A_1|_{K_{\text{smear}}} \tag{6.30}$$

The correction to A_1^d is from 0.004 to 0.008, the maximum correction value is 0.008. And the corrections to $A_1^{K_s^0}$ is from 0.009 to 0.086, the maximum value is 0.086. Where the last two x-bins corrections are large due to the lower statistic. Most of x-bins corrections are lower than 0.01.

6.4.6 Total systematic uncertainty

The total systematic uncertainty assigned to the asymmetries comprises all the contributions described in the previous sections. Each systematic uncertainty was added in quadrature to give the total systematic uncertainty for each x-bin,

$$\delta A_1^{\mathrm{tot}}(x) = \sqrt{\sum_i ([\delta A_1(x)]_i)^2} \tag{6.31}$$

For the data obtained in the year 2000 the uncertainty assigned to g_2 is the most important component. The uncertainty associated with the spin structure function g_2 is strongly dependent on kinematics and becomes the dominant contribution to the bins at highest x.

The shaded band in Fig. 6.6 and 6.7 shows the total systematic uncertainty of the photon-nucleon asymmetry.

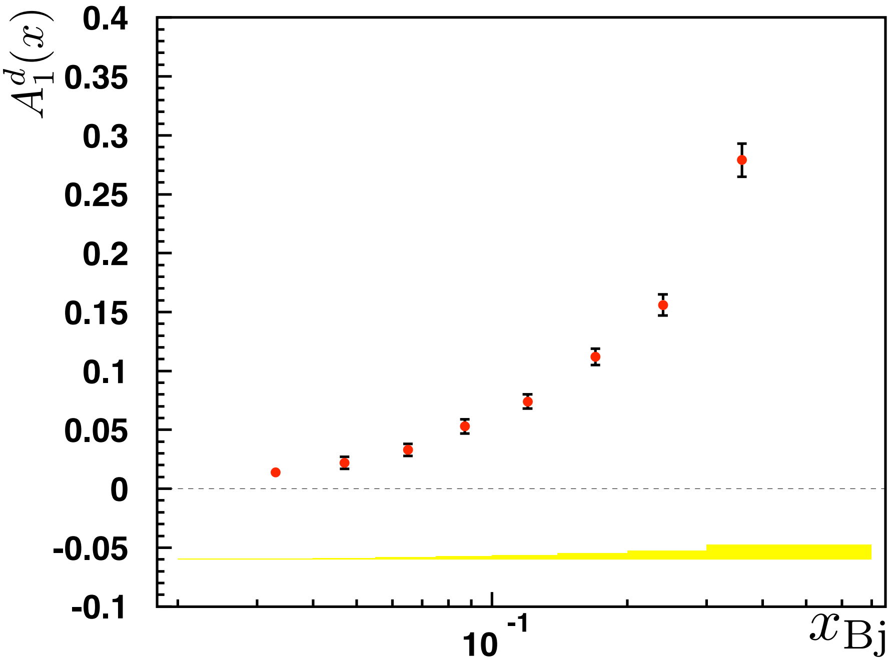

Figure 6.6: The inclusive Born level photon-nucleon asymmetries on the deuteron. The error bars give the statistical uncertainties, and the shaded bands indicate the systematic uncertainty.

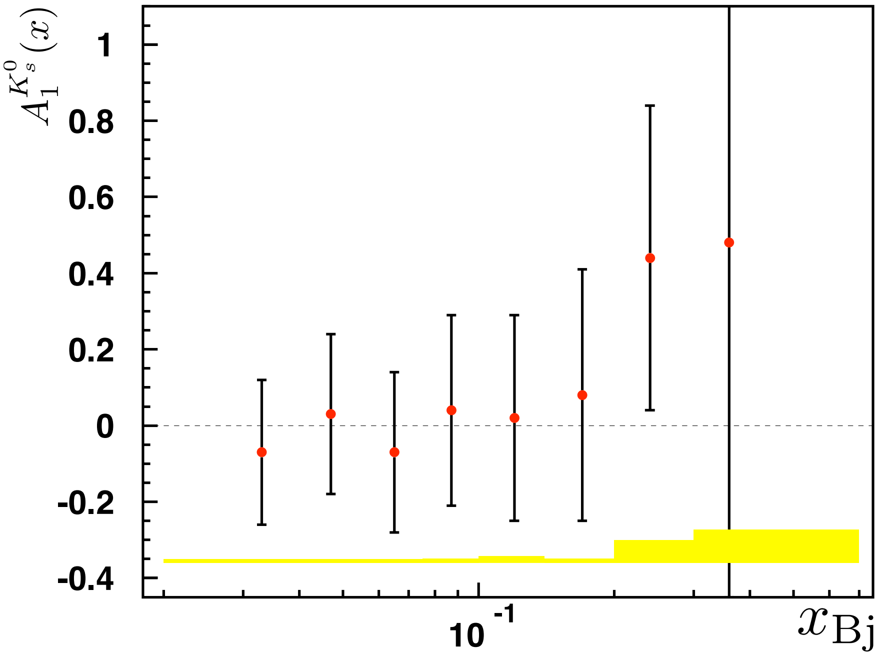

Figure 6.7: The Semi-inclusive K_s^0 Born level photon-nucleon asymmetries on the deuteron. The error bars give the statistical uncertainties, and the shaded bands indicate the systematic uncertainty.

Chapter 7

The Multiplicity of K_s^0 and the integral fragmentation functions

7.1 Determination of multiplicity of K_s^0

The Semi-Inclusive Deep Inelastic Scattering (SIDIS) cross section for hadron production at a given x, normalised to corresponding inclusive cross section, is

$$\frac{\mathrm{d}\sigma^h(x,z)/\mathrm{d}x\mathrm{d}z}{d\sigma^{\mathrm{dis}}(x)/\mathrm{d}x} = \frac{\mathrm{d}N^h(x,z)/\mathrm{d}x\mathrm{d}z}{\mathrm{d}N^{\mathrm{dis}}(x)/\mathrm{d}x} = \frac{\sum_f e_f^2 q_f(x,Q^2) D_f^h(z)}{\sum_f e_f^2 q_f(x,Q^2)} \tag{7.1}$$

Integrating over the measured z range and assuming only charge conjugation invariance, i.e.

$$D_u^{K_s^0} = D_{\bar{u}}^{K_s^0}, \qquad D_d^{K_s^0} = D_{\bar{d}}^{K_s^0}, \qquad D_s^{K_s^0} = D_{\bar{s}}^{K_s^0} \tag{7.2}$$

and supposing isospin invariance of quarks u and d in deuteron,

$$u_p(x) = d_n(x), \qquad d_p(x) = u_n(x) \tag{7.3}$$

Eq. 7.1 becomes for SIDIS K_s^0 production on the deuteron.

$$\frac{\mathrm{d}N^{K_s^0}(x)/\mathrm{d}x}{\mathrm{d}N^{\mathrm{dis}}(x)/\mathrm{d}x} = \frac{Q(x)\int D_{\mathrm{non-strange}}^{K_s^0}(z)\mathrm{d}z + S(x)\int D_{\mathrm{strange}}^{K_s^0}(z)\mathrm{d}z}{5Q(x)+2S(x)} \tag{7.4}$$

Where $Q(x)$, $S(x)$, $\int D^{K^0_s}_{\text{non-strange}}(z)\mathrm{d}z$ and $\int D^{K^0_s}_{\text{strange}}(z)\mathrm{d}z$ are defined as:

$$
\begin{aligned}
Q(x) &= d(x) + u(x) + \bar{d}(x) + \bar{u}(x)\\
S(x) &= s(x) + \bar{s}(x)
\end{aligned}
$$

$$
\begin{aligned}
\int D^{K^0_s}_{\text{non-strange}}(z)\mathrm{d}z &= 4\int D^{K^0_s}_{u}(z)\mathrm{d}z + \int D^{K^0_s}_{d}(z)\mathrm{d}z\\
\int D^{K^0_s}_{\text{strange}}(z)\mathrm{d}z &= 2\int D^{K^0_s}_{s}(z)\mathrm{d}z
\end{aligned}
\tag{7.5}
$$

In order to extract the number of K_s^0 and thus to determine the K_s^0 cross section, it is necessary to estimate the amount of the background under the signal peak and to correct for the detection efficiency. For this purpose, fits similar to those described in chapter 5 (see Fig. 5.2) are performed in different x bins. The signal is divided into 8 bins in the range 0.02 → 0.7 see Tab. 4.3. No significant K_s^0 signal is observed outside this range 0.02 → 0.7.

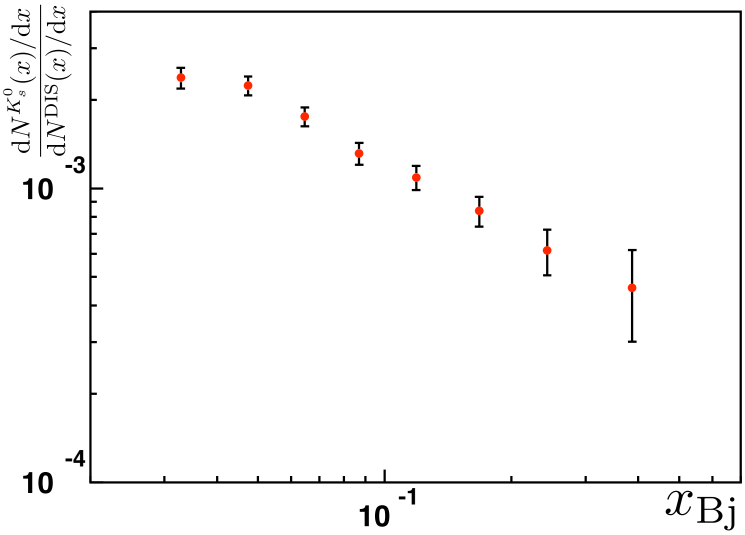

Figure 7.1: The raw multiplicity of K_s^0 versus x_{Bj}

To determine the number of the K_s^0 per x bin, the entries in the mass range from 480 MeV/c^2 to 520 MeV/c^2 are summed up and the background obtained from the fitted polynomial function is subtracted. Fig. 7.1 shows the raw multiplicity from K_s^0 of the 2000 data set of HERMES.

7.2 The corrections for the multiplicity

Charge symmetric background

Process like π^0 decay to two photons or high energy Bremsstrahlung photons constitute a source of e^+e^- pair production. The produced positron may fulfil the deep inelastic scattering kinematic cuts. It will increase the inclusive scattered positron counts. To subtract these faked inclusive scattered positrons, one event has to be removed from the data sample each time when an electron passes the deep inelastic scattering kinematic cuts.

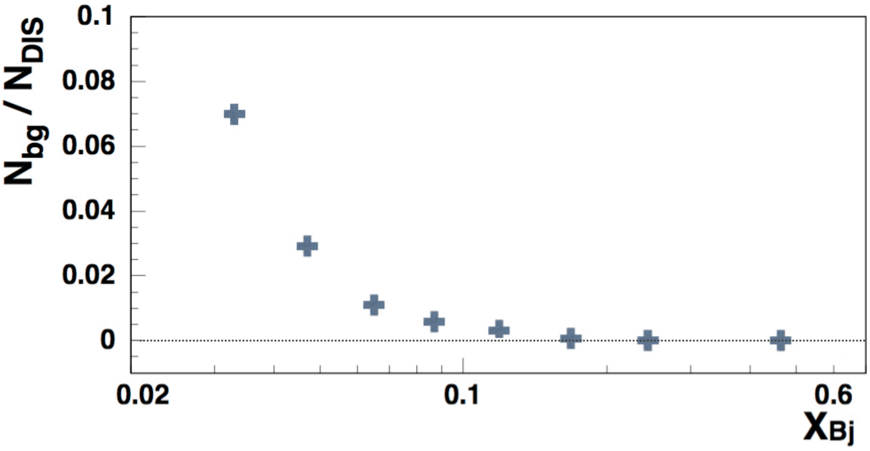

Figure 7.2: Fraction of background events found in each x-bin with respect to the number of DIS candidates after background subtraction.

7.2.1 Smearing, acceptance and radiative corrections

A correction method of the hadron multiplicity for detector smearing, radiative effects and acceptance is described in [103]. For simplicity, these corrections will be called "smearing unfolding". The smearing unfolding is described by the following expression:

$$X_{\mathrm{DIS}(K_s^0)}(i) = L_{\mathrm{DIS}(K_s^0)} k(i) \sum_{j=0}^{n_B} S_{\mathrm{DIS}(K_s^0)}(i,j) B_{\mathrm{DIS}(K_s^0)}(j) \tag{7.6}$$

where,

- $X_{\mathrm{DIS}(K_s^0)}(i)$ denotes the experimental DIS(kaon) yield as function of the experimental kinematic bin i.
- $B_{\mathrm{DIS}(K_s^0)}(j)$ denotes the unkown Born DIS(kaon) yield as function of the Born kinematic bin j.
- $k(i)$ is the unknown integrated luminosity including the unsimulated detector inefficiences.
- $L_{\mathrm{DIS}(K_s^0)}$ are the luminosities. Here L_{DIS} and L_K are equal since the kaon yield is a subsample of the DIS yield.
- $S_{\mathrm{DIS}(K_s^0)}(i,j)$ is the smearing matrix defined by:

$$S_{\mathrm{DIS}(K_s^0)}(i,j) = \frac{\sigma^X(i)}{\sigma^B(j)} = \frac{n_{\mathrm{DIS}(K_s^0)}(i,j)}{n^B_{\mathrm{DIS}(K_s^0)}(j)} \tag{7.7}$$

The matrix $n_{\mathrm{DIS}(K_s^0)}(i,j)$ represents the number of inclusive positron (K_s^0) where the experimental kinematic falls in bin $i = 1, ..., n_X$ and the Born kinematic falls in bin $j = 1, ..., n_B$. The extra bin j = 0 holds the events characterised by the experimental kinematics being inside the HERMES DIS/SIDIS cuts and geometry acceptance (mentioned in section 4, Data selection and cuts) while the corresponding Born kinematics ($Q^2, W^2, ...$) being outside the HERMES acceptance.

Two sets of Monte Carlo files are used to extract the smearing matrices S. In the first set, Born DIS events are generated in 4π without inclusion of any radiative processes and detector simulation. This set is used to calculate the vectors $n^B_{\mathrm{DIS}(K_s^0)}(j)$. The second Monte Carlo set includes all the effects mentioned above and is used to extract the matrices $n_{\mathrm{DIS}(K_s^0)}(i,j)$. The DIS and charge kaons matrices $n_{\mathrm{DIS}(K_s^0)}(i,j)$ obtained are ploted in Fig. 7.3

The unknown factor $k(i)$ is extracted from Eq. 7.6:

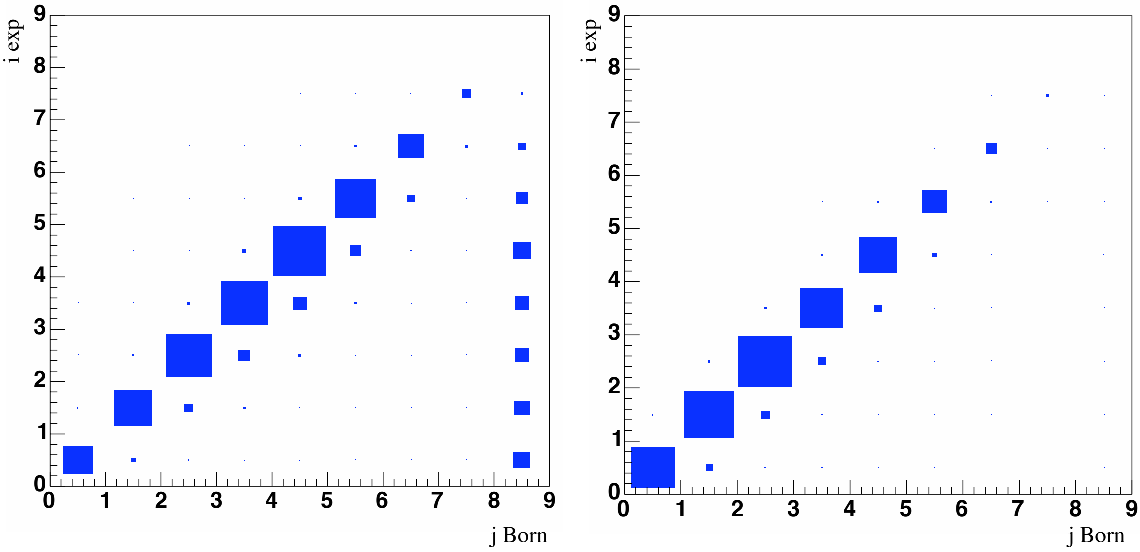

Figure 7.3: The smearing matrices of inclusive positron and K_s^0 which are used to unfold the multiplicity for radiative effects.

$$k(i) = \frac{X_{\mathrm{DIS}}(i)}{L\sum_{j=0}^{n_B} S_{\mathrm{DIS}}(i,j)B_{\mathrm{DIS}}(j)} \tag{7.8}$$

and plugged into the experimental kaon yield:

$$X_{K_s^0}(i) = \frac{X_{\mathrm{DIS}}(i)\sum_{j=0}^{n_B} S_{\mathrm{DIS}}(i,j)B_{\mathrm{DIS}}(j)}{\sum_{j=0}^{n_B} S_{\mathrm{DIS}}(i,j)B_{\mathrm{DIS}}(j)} \tag{7.9}$$

It is evident that the term in the denominator is simply the number of the experimental DIS events extracted from the Monte Carlo $n_{\mathrm{DIS}}^X(i)$. By inverting the matrix and rearranging terms in the above equation, the K_s^0 Born multiplicity $R_B(j) = B_{\mathrm{DIS}}(j)/n_{\mathrm{DIS}}^B(j)$ is obtained.

$$R_B(j) = \frac{1}{n_{\mathrm{DIS}}^B(j)}\sum_{i=1}^{n_X}[S'_{\mathrm{DIS}}]^{-1}(i,j)[R_X(i)n_{DIS}^X - n_{\mathrm{DIS}}(i,0)] \tag{7.10}$$

The error propagation through the smearing unfolding is accomplished via the radiative dilution matrix $D(j,i)$ defined by:

$$D(j,i) = \frac{R_B(j)}{R_X(i)} = \frac{[S'_{\mathrm{DIS}}]^{-1}(j,i)n_{\mathrm{DIS}}^X(i)}{n_{\mathrm{DIS}}^B(j)} \tag{7.11}$$

and the error on the Born kaon multiplicity is

$$\delta(R_B(j)) = \sum_{i=1}^{n_X} D^2(j,i)(R_X(i)) \tag{7.12}$$

7.3 BORN multiplicity of K_s^0

Fig. 7.4 shows the final K_s^0 multiplicity obtained after applying all the corrections discussed above.

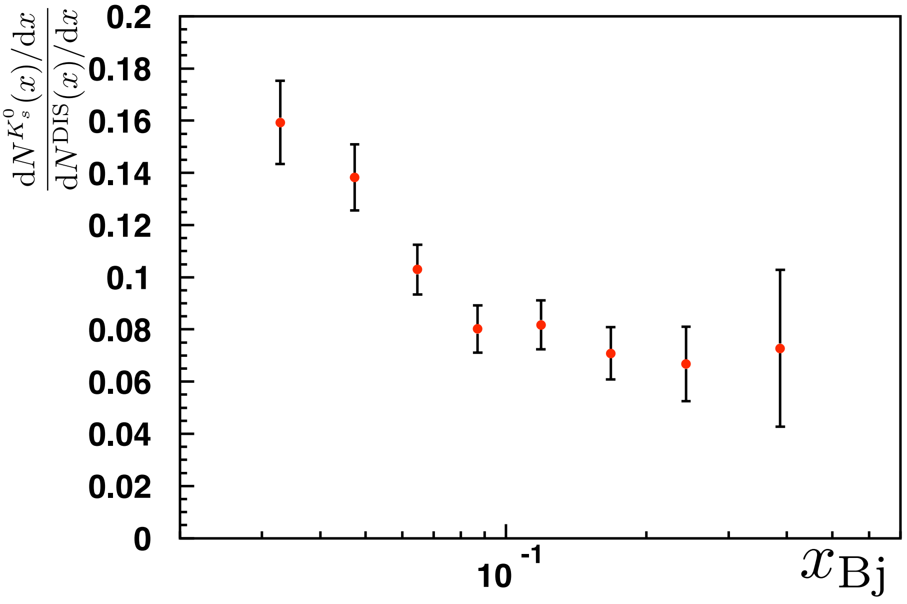

Figure 7.4: The final K_s^0 BORN multiplicity distributions versus x including all corrections.

In Eq. 7.4 the integral strange and non-strange fragmentation functions can be extracted by fitting the x dependence of this ratio together with parton distributions taken from the CTEQ6 compilation.

7.4 Extraction of the integral strange and non-strange K_s^0 fragmentation functions

In this section, the procedure used to extract the strange and the non strange kaon fragmentation functions from HERMES data is presented. As mentioned before, the relation between the K_s^0 multiplicity obtained in the last section and $\int D_{\text{non-strange}}(z)dz$, $\int D_{\text{strange}}(z)dz$ and the parton distribution functions is expressed by the following equation:

$$\frac{\mathrm{d}N^K(x)/\mathrm{d}x}{\mathrm{d}N^{\mathrm{DIS}}(x)/\mathrm{d}x} = \frac{Q(x)\int D^K_{\text{non-strange}}(z)\mathrm{d}z + S(x)\int D^K_{\text{strange}}(z)\mathrm{d}z}{5Q(x)+2S(x)} \tag{7.13}$$

Where the expression of $Q(x) \equiv u(x)+\bar{u}(x)+d(x)+\bar{d}(x)$ and $S(x) \equiv s(x)+\bar{s}(x)$ are given in section 7.1. In a matrix form, the above equation becomes:

$$\vec{M} = Q\vec{D} \tag{7.14}$$

Where the vector $\vec{M}$ contains the K_s^0 multiplicities measured using 8 x_{Bj} bins. The vector $\vec{D}$ holds the two unknown K_s^0 integral fragmentation functions and Q is a 8 x 2 matrix holding the strange and the non-strange CTEQ6 parton distribution function at the different 8 x_{Bj} bins:

$$Q_{ij} = \begin{cases} Q(x_i) & \text{if } j=1 \\ \\ S(x_i) & \text{if } j=2 \end{cases} \tag{7.15}$$

It is clear that we are dealing with an over determined system of equations since the number of available equations exceeds by large the number of unknowns and a solution to the problem is to find a $\vec{D}$ that minimises χ^2:

$$\chi^2 = (\vec{M} - Q\vec{D})^T(\vec{M} - Q\vec{D}) \tag{7.16}$$

The K_s^0 multiplicity obtained from these values combined with the CTEQ6 parton distribution is shown in Fig. 7.5. The CTEQ6 is a well know parametrizations for parton distribution functions, it assumes $s = \bar{s} = 0.2(\bar{u} + \bar{d})$ [107]. A comparison of fragmentation functions parametrizations from B. A. Kniehl, G. Kramer and B. Pötter (KKP) [104] and HERMES data is shown in Tab. 7.1. There are three well known groups [104, 105, 106] who are working on the parametrizations of fragmentation functions by fitting the world available data. Only KKP gives the fragmentation functions parametrizations for K_s^0 currently by assuming $D^{K_s^0/\bar{K_s^0}}_{u,d,s,c,b,g}(x,Q^2) = D^{K^\pm}_{d,u,s,c,b,g}(x,Q^2)$ [104]. These results provide useful constraints on available parameterizations which are based on e^+e^- collider data at much higher center-of-mass energies.

The fit in Fig. 7.5 is not perfect. The shape of the fit function, which is determined by the functional form of the CTEQ6 parameterization is not quite able to reproduce the experimental results. There might be several reasons for it:

- There may be remaining uncertainties in the experimental data due to possible problems in the Monte Carlo simulation of the kaon distributions which were used for the unfolding corrections of the multiplicities.

- The world fits of $s(x)$ from CTEQ6 have remaining uncertainties and are possibly biased by the functional form that was used in the fits. There are no precise data that determine the shape of the unpolarised strange distribution functions in our x and Q^2 range.

- There are possibly limitations in the validity of the factorisation assumption between the hard scattering and the fragmentation process which is required for this analysis. However, from all studies which have been done, there is no indication of a break-down of factorisation in our kinematical range.

The results of the integrated fragmentation functions as shown in table 7.1 come out very different than expected from the analysis of e^+e^- data by KKP. The very small fragmentation function for the production of K_s^0 from unpolarised quarks and the very large contribution from strange quarks is surprising, however these results agree with a previously done similar analysis of charged kaons [102].

	This work	KKP
$\int D^{K_s^0}_{non-strange}(z)\mathrm{d}z$	0.16 ± 0.06	1.111
$\int D^{K_s^0}_{strange}(z)\mathrm{d}z$	3.2 ± 0.6	0.15

Table 7.1: The integral non-strange and strange fragmentation functions with statistical errors which are extracted from HERMES polarised deuteron of 2000 data set. And a comparison of fragmentation functions from KKP is also shown here.

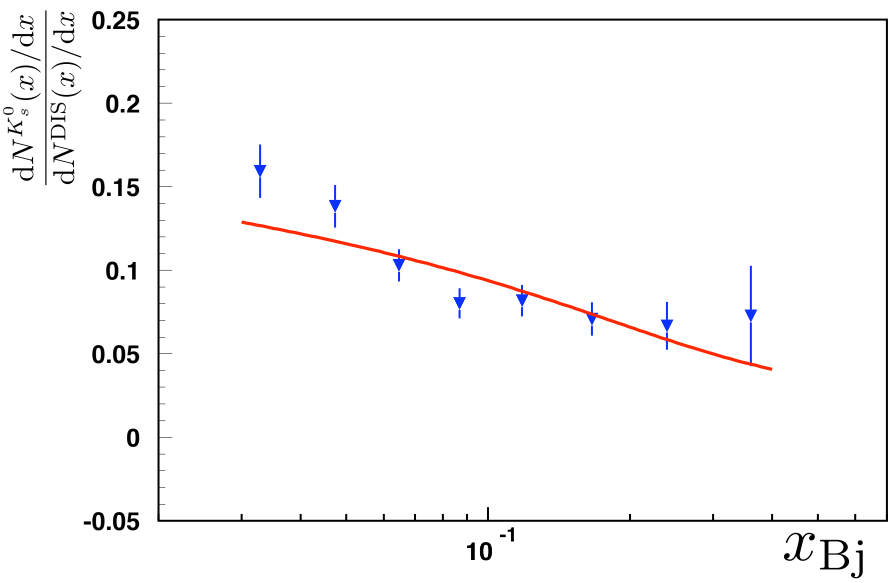

Figure 7.5: The final K_s^0 BORN multiplicity distributions versus x including all corrections (blue triangle points). And the red line shows the fit results combined with the leading order CTEQ6 parameterizations of parton distribution functions. The fit results are shown in Tab. 7.1.

Chapter 8

Extraction of polarisation of strange quarks with isoscalar method

8.1 Isoscalar method formalism

Following the parton model as applied in [108] in leading order the semi-inclusive longitudinal double spin asymmetry for production of hadron h can be written in terms of the quark helicity distributions $\Delta q(x, Q^2)$ and the fragmentation function $D_q^h(x, Q^2)$ as

$$A_1^h(x, Q^2, z) = \frac{\sum_q e_q^2 \Delta q(x, Q^2) D_q^h(z, Q^2)}{\sum_{q'} e_{q'}^2 q'(x, Q^2) D_{q'}^h(z, Q^2)} \tag{8.1}$$

where D_q^h is a measure of the probability that a quark of flavour q will fragment into a hadron of type h. Using the purity formalism Eq. 8.1 can be rewritten as

$$A_1^h(x, Q^2, z) = \sum_q \mathcal{P}_q^h(x, Q^2, z) \frac{\Delta q(x, Q^2)}{q(x, Q^2)} \tag{8.2}$$

where the purity is given by

$$\mathcal{P}_q^h(x,Q^2,z) = \frac{e_q^2 q(x,Q^2) D_q^h(z,Q^2)}{\sum_{q'} e_{q'}^2 q'(x,Q^2) D_{q'}^h(z,Q^2)} \tag{8.3}$$

This formalism can be applied to an analysis of the inclusive asymmetry $A_{1,D}(x,Q^2)$ and the isoscalar K_s^0 asymmetry $A_{1,D}^{K_s^0}(x,Q^2)$ for an isoscalar deuteron target. One assumes only charge conjugation invariance in the evaluation of the purities. The result is a simple linear relationship between the two measured spin asymmetries and the total non-strange and the total strange quark polarisations, $[\Delta Q(x)/Q(x)]$ and $[\Delta S(x)/S(x)]$, which is given by the matrix equation

$$\begin{pmatrix} A_{1,d}^e(x) \\ \\ A_{1,d}^{K_s^0}(x) \end{pmatrix} = C_R \begin{pmatrix} \mathcal{P}_Q^e(x) & \mathcal{P}_S^e(x) \\ \\ \mathcal{P}_Q^{K_s^0}(x) & \mathcal{P}_S^{K_s^0}(x) \end{pmatrix} \begin{pmatrix} \Delta Q(x)/Q(x) \\ \\ \Delta S(x)/S(x) \end{pmatrix} \tag{8.4}$$

Both $Q(x) \equiv u(x) + \bar{u}(x) + d(x) + \bar{d}(x)$ and $S(x) \equiv s(x) + \bar{s}(x)$ are isoscalar. The inclusive purities given in terms of parton distributions have the simple form

$$\mathcal{P}_Q^e(x) = \frac{5Q(x)}{5Q(x)+2S(x)}, \quad \mathcal{P}_S^e(x) = \frac{2S(x)}{5Q(x)+2S(x)} \tag{8.5}$$

The purities for the K_s^0 asymmetries include factors given by the appropriate fragmentation functions integrated over the measured range of values of $z = E_h/\nu$

$$\begin{aligned} \mathcal{P}_Q^{K_s^0}(x) &= \frac{Q(x)\int D_{\mathrm{non-strange}}^{K_s^0}(z)\mathrm{d}z}{Q(x)\int D_{\mathrm{non-strange}}^{K_s^0}(z)\mathrm{d}z + S(x)\int D_{\mathrm{strange}}^{K_s^0}(z)\mathrm{d}z} \\ \mathcal{P}_S^{K_s^0}(x) &= \frac{S(x)\int D_{\mathrm{strange}}^{K_s^0}(z)\mathrm{d}z}{Q(x)\int D_{\mathrm{non-strange}}^{K_s^0}(z)\mathrm{d}z + S(x)\int D_{\mathrm{strange}}^{K_s^0}(z)\mathrm{d}z} \end{aligned} \tag{8.6}$$

The strange and non-strange fragmentation functions of Eq. 8.6 are simple functions of the familiar fragmentation functions measured in collider experiments [105]:

$$\begin{aligned} \int D_{\mathrm{non-strange}}^{K_s^0}(z)\mathrm{d}z &= 4\int D(z)_u^{K_s^0}\mathrm{d}z + \int D(z)_d^{K_s^0}\mathrm{d}z \\ \int D_{\mathrm{strange}}^{K_s^0}(z)\mathrm{d}z &= 2\int D(z)_s^{K_s^0}\mathrm{d}z \end{aligned} \tag{8.7}$$

The factor $C_R \equiv (1+R)/(1+\gamma^2)$ in Eq. 8.4 connects the usual compiled parton distributions with those needed here to describe the longitudinal spin asymmetries.

	$< x >$	$< Q >$	$P_Q(x)$	$P_S(x)$	$P_Q^{K_s^0}$	$P_S^{K_s^0}$
1	0.033	1.222	0.9750	0.0250	0.4341	0.5659
2	0.047	1.489	0.9751	0.0249	0.4344	0.5656
3	0.065	1.743	0.9770	0.0230	0.4544	0.5456
4	0.087	2.013	0.9798	0.0202	0.4875	0.5125
5	0.118	2.413	0.9834	0.0166	0.5381	0.4619
6	0.166	3.225	0.9880	0.0120	0.6169	0.3831
7	0.239	4.591	0.9993	0.0007	0.9640	0.0360
8	0.360	7.134	0.9997	0.0003	0.9848	0.0152

Table 8.1: The element value of Purity matrix $\mathcal{P}(x)$ calculated as a function of x from both the parameterisation CTEQ6LO and the integral fragmentation functions which are obtained from the fitting to HERMES K_s^0 multiplicities.

8.2 Extraction of $\Delta S(x)/S(x)$ and $\Delta Q(x)/Q(x)$

Results obtained in the previous sections are used to extract $(\Delta s(x)+\Delta\bar{s}(x))/(s(x)+\bar{s}(x))$ and $\Delta Q(x)/Q(x)$. These quantities are related to the measured inclusive asymmetry $A_{1,D}(x)$ and to the K_s^0 asymmetries $A_{1,D}^{K_s^0}(x)$ through the purity matrix $\mathcal{P}(x)$ in equation 8.4. The elements of the purity matrix $\mathcal{P}(x)$ are defined in equation 8.5 and 8.6. They are evaluated using the strange and the non-strange K_s^0 fragmentation functions obtained in section 7.4 and using the CTEQ6LO quark distribution function. The definition of the C_R factor is also given in section 8.1. The solution of the system of equation 8.4 allows the determination of $(\Delta s(x) + \Delta\bar{s}(x))/(\Delta s(x) + \bar{s}(x))$ and $x(\Delta s(x) + \Delta\bar{s}(x))$:

$$\frac{\Delta Q(x)}{Q(x)} = \frac{1}{C_R}\frac{\mathcal{P}_S^{K_s^0} A_{\mathrm{D}}(x) - \mathcal{P}_S A_{\mathrm{D}}^{K_s^0}(x)}{\mathcal{P}_S^{K_s^0}\mathcal{P}_Q - \mathcal{P}_S\mathcal{P}_Q^{K_s^0}} \tag{8.8}$$

$$\frac{\Delta S(x)}{S(x)} = \frac{1}{C_R}\frac{\mathcal{P}_Q A_{\mathrm{D}}^{K_s^0}(x) - \mathcal{P}_Q^{K_s^0} A_{\mathrm{D}}(x)}{\mathcal{P}_S^{K_s^0}\mathcal{P}_Q - \mathcal{P}_S\mathcal{P}_Q^{K_s^0}} \tag{8.9}$$

The results are shown in Fig.8.1 and Fig.8.2

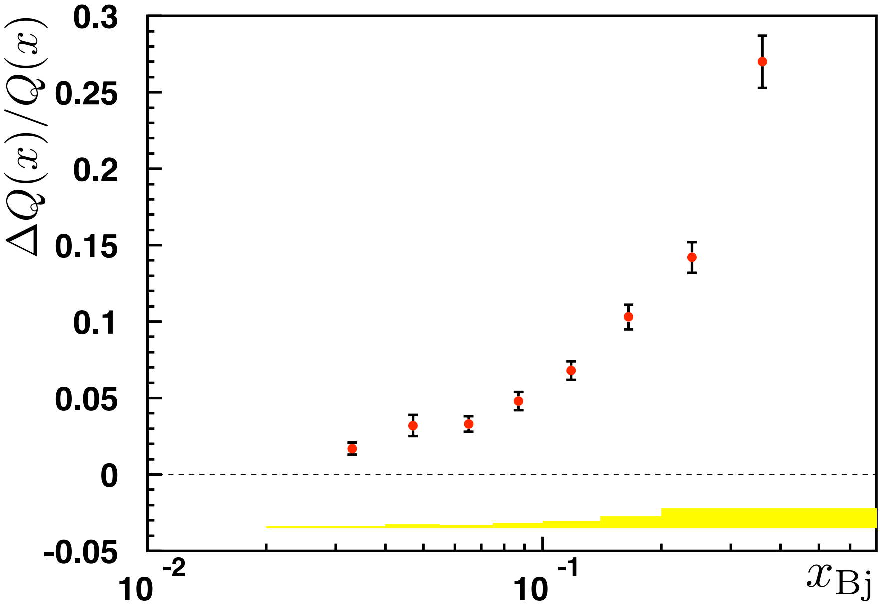

Figure 8.1: The non-strange quark polarisations, $\Delta Q(x)/Q(x)$, is shown as a function of x, as extracted from the HERMES inclusive and semi-inclusive asymmetries. The error bars are the statistical uncertainties. The band represents the total systematic uncertainty.

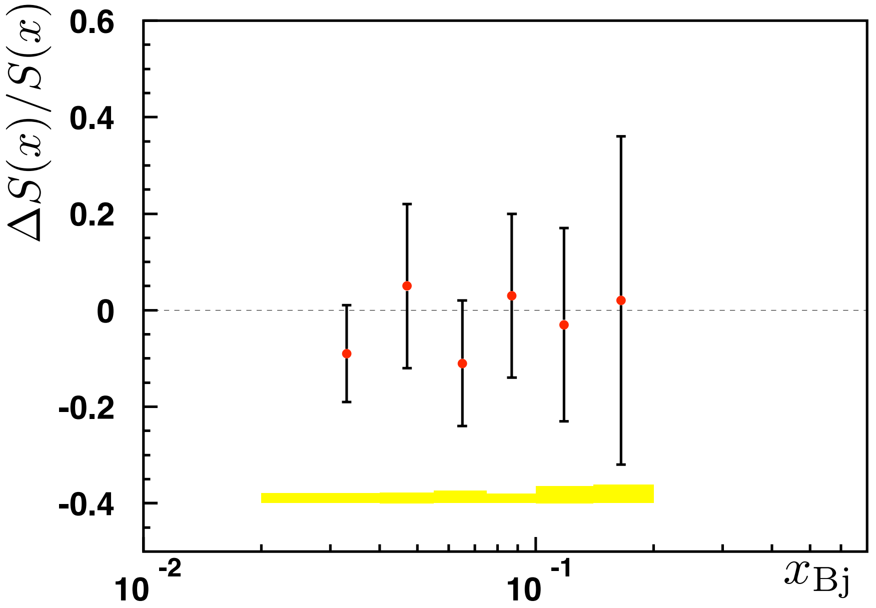

Figure 8.2: The strange quark polarisations, $\Delta S(x)/S(x)$, is shown as a function of x, as extracted from the HERMES inclusive and semi-inclusive asymmetries. The error bars are the statistical uncertainties. The band represents the total systematic uncertainty.

8.3 The systematic errors

The systematic uncertainty of the strange and non-strange quark polarisation comes mainly from three aspects. The first contribution, comes from the systematic uncertainty of the spin asymmetries which is extracted from inclusive and semi-inclusive data. The second part, comes from the systematic uncertainty from the determination of the fragmentation functions which are used to calculate the purity matrice $\mathcal{P}$. The third part, comes from the factor C_R that connects the usual compiled parton distributions which describes the longitudinal spin asymmetries.

The systematic uncertainty of the strange quarks polarisation are extracted in complete analogy to the non-strange quarks polarisation.

Here, only the strange quarks polarisation systematic uncertainty formula will be presented in detail.

8.3.1 The errors from asymmetries

There are several different systematic uncertainty is from the determination of the inclusive asymmetries and semi-inclusive asymmetries that contribute to the total systematic uncertainty of inclusive asymmetries and semi-inclusive asymmetries as described in chapter 6.4:

- Target polarisation systematic uncertainty.
- Beam polarisation systematic uncertainty.
- The photon absorption cross section ratio parametrisation $R(x, Q^2) = \sigma_L/\sigma_T$.
- Model of proton polarisation structure function $g_2(x, Q^2)$.
- Smearing and radiative corrections uncertainties.

The $\delta A_D^{K_s^0}(x)$ and $\delta A_D(x)$ systematic uncertainty from above systematic uncertainty contribution will be propagated to the systematic uncertainty of the strange quarks polarisation.

The contribution to the total strange quarks polarisation systematic uncertainty can be expressed as:

$$\delta\left[\frac{\Delta S(x)}{S(x)}\right]_A = \sqrt{\left(\frac{\partial(\Delta S(x)/S(x))}{\partial A_D^{K_s^0}(x)}\delta A_D^{K_s^0}(x)\right)^2 + \left(\frac{\partial(\Delta S(x)/S(x))}{\partial A_D(x)}\delta A_D(x)\right)^2} \tag{8.10}$$

8.3.2 The errors from the purity $\mathcal{P}$ matrix

The systematic uncertainty associated to the determination of the fragmentation functions which are used to calculate the purity matrix $\mathcal{P}$ can be writen as:

$$\delta\left[\frac{\Delta S(x)}{S(x)}\right]_{\mathcal{P}} = \sqrt{\left(\frac{\partial(\Delta S(x)/S(x))}{\partial \mathcal{P}_Q^{K_s^0}(x)}\delta \mathcal{P}_Q^{K_s^0}(x)\right)^2 + \left(\frac{\partial(\Delta S(x)/S(x))}{\partial \mathcal{P}_S^{K_s^0}(x)}\delta \mathcal{P}_S^{K_s^0}(x)\right)^2} \tag{8.11}$$

where the systematic uncertainty $\delta\mathcal{P}_Q^{K_s^0}(x)$ and $\delta\mathcal{P}_S^{K_s^0}$ are calculated from equation 8.6

8.3.3 The errors from factor $C_R(x, Q^2)$

The systematic uncertainty associated with the factor $C_R(x, Q^2)$, which related to the parametrisation of the photon absorption ration $R(x, Q^2)$:

$$\delta C_R(x, Q^2) = \frac{1}{1+\gamma^2}\delta R(x, Q^2) \tag{8.12}$$

the contribution to the total systematic uncertainty of the strange quarks polarisation from $C_R(x, Q^2)$ is:

$$\delta\left[\frac{\Delta S(x)}{S(x)}\right]_{C_R} = \sqrt{\left(\frac{\partial(\Delta S(x)/S(x))}{\partial C_R}\delta C_R\right)^2} \tag{8.13}$$

8.3.4 The total errors

The total systematic uncertainty of the strange quarks polarisation is the quadratic sum of the different partial systematic uncertainties discussed above.

$$\delta\left[\frac{\Delta S(x)}{S(x)}\right] = \sqrt{\left(\delta\left[\frac{\Delta S(x)}{S(x)}\right]_A\right)^2 + \left(\delta\left[\frac{\Delta S(x)}{S(x)}\right]_{\mathcal{P}}\right)^2 + \left(\delta\left[\frac{\Delta S(x)}{S(x)}\right]_{C_R}\right)^2} \qquad (8.14)$$

$$\delta\left[\frac{\Delta Q(x)}{Q(x)}\right] = \sqrt{\left(\delta\left[\frac{\Delta Q(x)}{Q(x)}\right]_A\right)^2 + \left(\delta\left[\frac{\Delta Q(x)}{Q(x)}\right]_{\mathcal{P}}\right)^2 + \left(\delta\left[\frac{\Delta Q(x)}{Q(x)}\right]_{C_R}\right)^2} \qquad (8.15)$$

The remaining uncertainties coming from uncertainties in the used Monte Carlo, from the factorisation assumption and from uncertainties in the parton distributions functions have not been included in this quantitative error estimate.

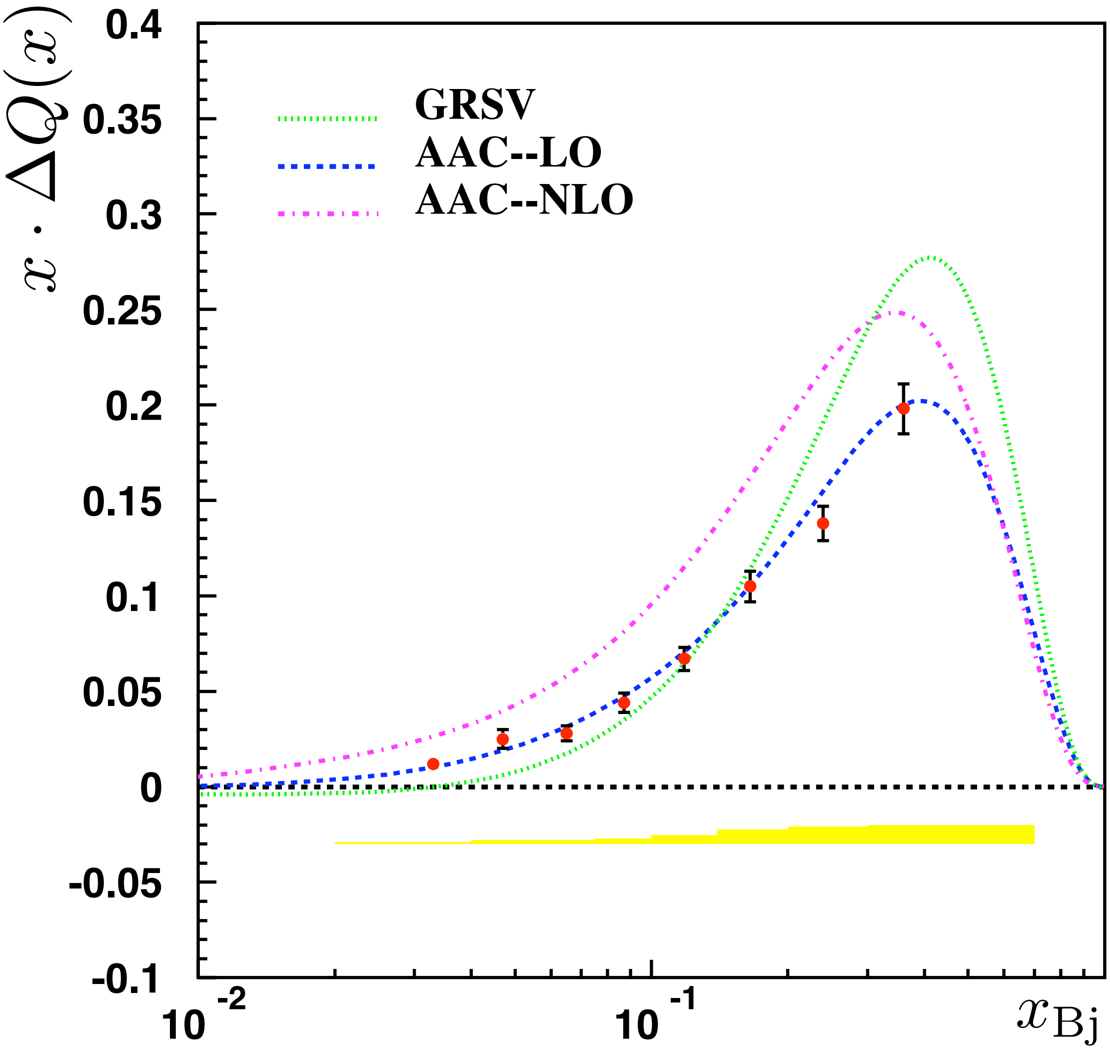

Figure 8.3: The quark helicity distributions $x \cdot \Delta Q(x)$ shown as a function of x. The dashed line is the GRSV2000 parameterisation (LO, standard) [109] and dashed-dotted line is AAC parameterisation (LO,2000) [110].The error bars are the statistical uncertainties. The band represents the total systematic uncertainty.

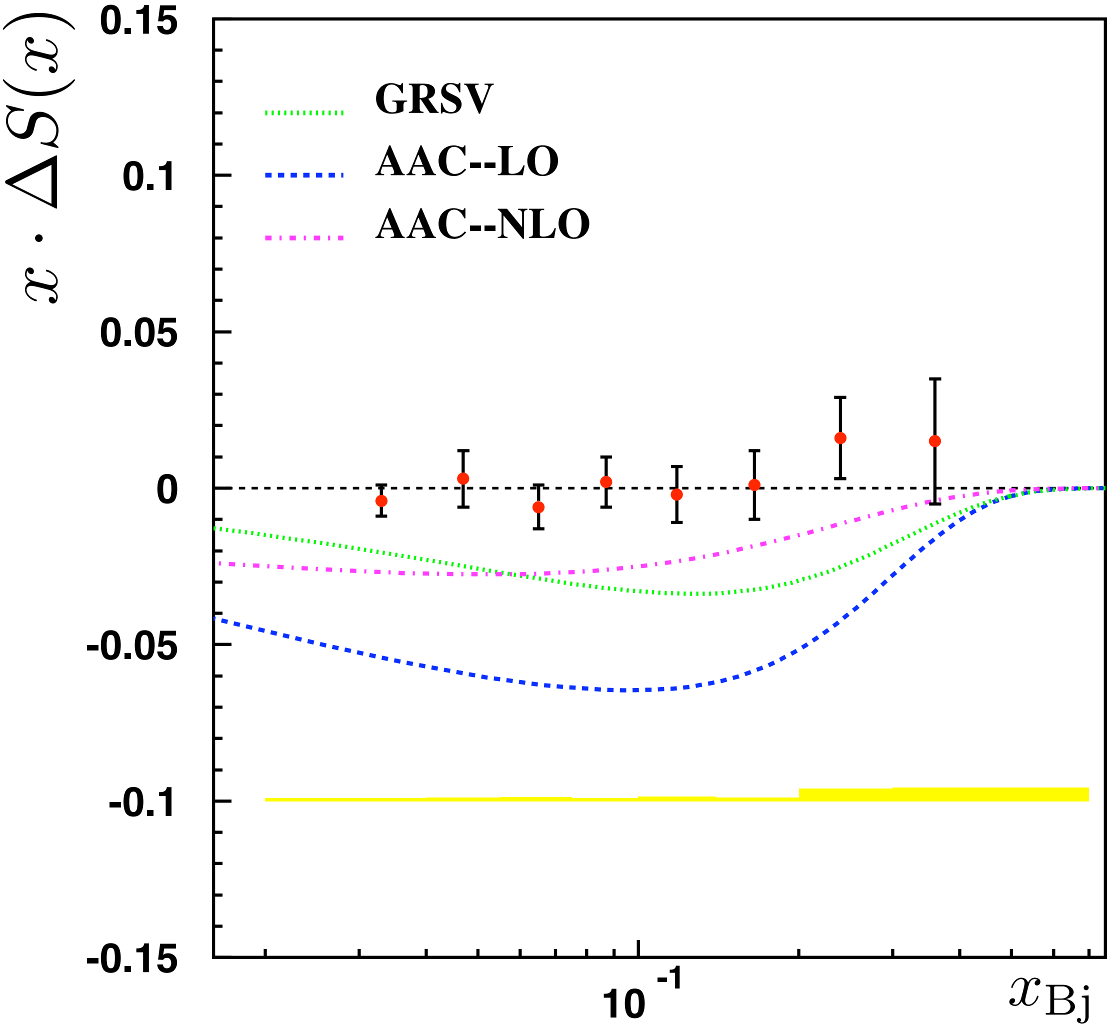

Figure 8.4: The quark helicity distributions $x \cdot \Delta S(x)$ shown as a function of x. The dashed line is the GRSV2000 parameterisation (LO, standard) [109] and dashed-dotted line is AAC parameterisation (LO,2000) [110] .The error bars are the statistical uncertainties. The band represents the total systematic uncertainty.

8.4 First moment

The n^{th} moment of the polarised parton distribution $\Delta q_f(Q^2)$ is given by:

$$\Delta^{(n)} q_f(Q^2) = \int_0^1 \mathrm{d}x \cdot x^{n-1} \Delta q(x, Q^2) \tag{8.16}$$

The first moment ($n = 1$) of the strange and non-strange polarised parton distributions, in the measured x-region ($0.2 < x < 0.7$), are obtained from the measurement presented above by applying the following formula:

$$\Delta Q = \int_{0.02}^{0.7} \mathrm{d}x \Delta Q(x, Q^2) = \sum_i \frac{\Delta Q}{Q}(x_i) \int_{x_i}^{x_{i+1}} Q(x, Q^2) \mathrm{d}x \tag{8.17}$$

$$\Delta S = \int_{0.02}^{0.7} \mathrm{d}x \Delta S(x, Q^2) = \sum_i \frac{\Delta S}{S}(x_i) \int_{x_i}^{x_{i+1}} S(x, Q^2) \mathrm{d}x \tag{8.18}$$

where the strange and the non-strange quark polarisations were assumed to be constant with each $[x_i, x_{i+1}]$ bin and Q^2-independent. The parametrisation of the unpolarisaed quark distributions are taken from the CTEQ6LO at each Q^2 and are integrated over each $[x_i, x_{i+1}]$ bin.

The first moment and their statistic errors and systematic uncertainties are given in Tab. 8.2.

	First moments	statistic error	systematic uncertainty
ΔQ	0.371	± 0.029	± 0.013
ΔS	0.010	± 0.066	± 0.004

Table 8.2: The first moment of the non-strange and the strange polarised quark distributions in the range $0.2 < x < 0.7$.

A comparison with other analysis results is shown in Tab. 8.3. This work gives the results from analysis of K_s^0 and the "analysis 1" shows the results from the analysis of charged kaons [102], both of them use "isoscalar method". The "analysis 2" is the results which are extracted with "purity methods" [108].

	This work	Analysis 1 [102]	Analysis 2 [108]
ΔQ	0.371 ± 0.029 ± 0.013	0.286 ± 0.026 ± 0.011	0.319 ± 0.043 ± 0.052
ΔS	0.010 ± 0.066 ± 0.004	0.006 ± 0.029 ± 0.007	0.028 ± 0.033 ± 0.009

Table 8.3: The first moment of the non-strange and the strange polarised quark distributions. The errors shown in the table are statistic errors and systematic uncertainties respectively. The Analysis 1 and Analysis 2 are the results from the methods of isoscalar and purity used by HERMES collaboration.

Chapter 9

Conclusion

The study of the nucleon structure via inclusive deep-inelastic scattering has played and still plays an important role in the establishment of the Quark-Parton Model in the composition of hadrons and subsequently of QCD as the theory of strong interactions. With polarised DIS the spin observables of the nucleon become accessible. A unique insight into the nucleon spin structure is provided by the semi-inclusive DIS process where both the scattered lepton and hadrons produced from the struck quark are detected.

In this thesis, inclusive DIS lepton and semi-inclusive K_s^0 double-spin asymmetries have been extracted from data collected by the HERMES experiment by using deep-inelastic scattering of a longitudinally polarised positron beam of 27.5 GeV from a longitudinal polarised deuteron gas target.

The same data set is used to extract two integral strange and non-strange fragmentation functions of K_s^0. These two values are used to determine a purity matrix which in turn allows the direct extraction of the strange and non-strange quark polarisation.

The value of the strange quark polarisation $\Delta S = 0.010 \pm 0.066(stat) \pm 0.004(syst)$ is obtained.

The value is compatible to zero. Consequently, the conclusion is the strange quark polarisation is compatible to zero within the experimental uncertainty over the measured x kinematic range.

This result is in contrast to the result obtained by inclusive data and the assumption of the validity of SU(3) flavour symmetry, but it agrees with previous direct measurements of HERMES from the analysis of semi-inclusive data. It confirms the previous finding of a unpolarised strange sea in a statistically and systematically independent way.

Acknowledgements

It is a great pleasure for me to work in the international environment of the HERMES Collaboration and involve the construction of an SFT (Scintillating Fibre Tracker) in the HERMES group of Justus-Liebig-Universität Giessen for more than four years and I am grateful for many invaluable experiences that I could gather here.

First and foremost, I would like to thank my supervisor Prof. Dr. M. Düren for giving me the freedom to pursue my personal preferences, for his constant support and also for his excellent guidance. Furthermore, I very much appreciate for his understanding and patience during private issues. It is his valuable suggestions that significantly make progress in my scientific research. At the same time, I want to sincerely thank Dr. E.C. Aschenauer and Senior physicist Dr. H.E. Jackson for their essential guidance and help during this work of the Δq analysis.

I very much appreciate my colleague Dr. M. Hoek for his help from the first day when I was in Germany. He picked me up from the railway station to the guest house at the Saturday afternoon. And he gave me a lot of help in the following four years work, specially, the benefit discussion on both hardware and software of the SFT detector.

Further, thanks to Dr. A. Hillenbrand, Dr. A.E. Alaoui and Y. Naryshkin for the help and cross check on the Δq analysis. I learned a lot from them during the discussion on the analysis. My thanks also to Dr. B. Maiheu for providing the example unfolding code; to T. Keri, Dr. L. Rubacek for their support on DAQ; to Dr. H. Lu, Z. Ye, H. Ye, Dr. S. Wang, W. Yu for their great tips about the C++ and root.

I sincerely express my gratitude to R. Schmidt, Dr. M. Ehrenfried and Dr. N.

Wang for their carefully reading my manuscript.

The special thanks must be given to Secretary M. Brunotte and A. Rühl. Without their help, I couldn't be concentrated on my work. "Vielen Dank".

My thanks also extend to Dr. B. Seitz, Dr. M. Hoek, T. Keri, Dr. R. Kaiser and R. Perez for their encouragement. They always said they like to work with me or like my production.

I want to thank Deutsche Forschungsgemeineschaft (DFG) and German Bundesministerium für Bildung und Forschung (BMBF) for the financial support, and thank the Europäisches Graduiertenkolleg for providing a lot of interest talks and also providing me many chances to visit other institutes during the Ph.D. work.

Also I send my thanks to many other people, too numerous to mention, who helped in their own little way throughout this work.

Last, but not least, I want to take this opportunity to thank my parents for providing me a sustained understanding and encouragement. I am forever grateful to my beloved wife Y. Han for her personal care and support. I sincerely appreciate and thank her for her love and also delicious dinner everyday.

Bibliography

[1] B. W. Filippone and Xiang-Dong Ji. The spin structure of the nucleon. *Adv. Nucl. Phys.* **26**, 1 (2001).

[2] Murray Gell-Mann. A schematic model of baryons and mesons. *Phys. Lett.* **8**, 214–215 (1964).

[3] G. Zweig. An su(3) model for strong interaction symmetry and its breaking. In *Lichtenberg, D. B. (Ed.), Rosen, S. P. (Ed.): Developments In The Quark Theory Of Hadrons, Vol. 1*, 22- 101 and CERN Geneva - TH. 401 (REC.JAN. 64) 24p.

[4] Richard P. Feynman. Very high-energy collisions of hadrons. *Phys. Rev. Lett.* **23**, 1415–1417 (1969).

[5] D. H. Perkins. Neutrino interactions. In *Chicago 1972, Proceedings, High Energy Physics Conference, Vol. 4*, Batavia 1973, 189-247.

[6] J. J. Aubert et al.. A detailed study of the nucleon structure functions in deep elastic muon scattering in iron. *Nucl. Phys.* **B272**, 158 (1986).

[7] D. J. Gross and Frank Wilczek. Asymptotically free gauge theories. 1. *Phys. Rev.* **D8**, 3633–3652 (1973).

[8] H. David Politzer. Reliable perturbative results for strong interactions? *Phys. Rev. Lett.* **30**, 1346–1349 (1973).

[9] H. Fritzsch, Murray Gell-Mann, and H. Leutwyler. Advantages of the color octet gluon picture. *Phys. Lett.* **B47**, 365–368 (1973).

[10] Jerome I. Friedman and Henry W. Kendall. Deep inelastic electron scattering. *Ann. Rev. Nucl. Part. Sci.* **22**, 203–254 (1972).

[11] J. D. Bjorken. Asymptotic sum rules at infinite momentum. *Phys. Rev.* **179**, 1547–1553 (1969).

[12] Jr. Callan, Curtis G. and David J. Gross. High-energy electroproduction and the constitution of the electric current. *Phys. Rev. Lett.* **22**, 156–159 (1969).

[13] B. H. Wiik. First results from petra. In *Bergen 1979, Proceedings, Neutrino '79, Vol.1*, 113- 154.(See Conference Index).

[14] M. J. Alguard et al.. Deep inelastic scattering of polarized electrons by polarized protons. *Phys. Rev. Lett.* **37**, 1261 (1976).

[15] M. J. Alguard et al.. Deep inelastic e p asymmetry measurements and comparison with the bjorken sum rule and models of the proton spin structure. *Phys. Rev. Lett.* **41**, 70 (1978).

[16] Guenter Baum et al.. A new measurement of deep inelastic e p asymmetries. *Phys. Rev. Lett.* **51**, 1135 (1983).

[17] J. Ashman et al.. A measurement of the spin asymmetry and determination of the structure function g_1 in deep inelastic muon proton scattering. *Phys. Lett.* **B206**, 364 (1988).

[18] P. L. Anthony et al.. Determination of the neutron spin structure function. *Phys. Rev. Lett.* **71**, 959–962 (1993).

[19] K. Abe et al.. Precision measurement of the proton spin structure function $g_1(p)$. *Phys. Rev. Lett.* **74**, 346–350 (1995).

[20] K. Abe et al.. Precision measurement of the deuteron spin structure function $g_1(d)$. *Phys. Rev. Lett.* **75**, 25–28 (1995).

[21] K. Abe et al.. Precision determination of the neutron spin structure function $g_1(n)$. *Phys. Rev. Lett.* **79**, 26–30 (1997).

[22] K. Abe et al.. Measurement of the neutron spin structure function $g_2(n)$ and asymmetry $A_2(n)$. *Phys. Lett.* **B404**, 377–382 (1997).

[23] P. L. Anthony et al.. Measurement of the deuteron spin structure function $g_1(d)(x)$ for $1(GeV/c)^2 < Q^2 < 40(GeV/c)^2$. *Phys. Lett.* **B463**, 339–345 (1999).

[24] P. L. Anthony et al.. Measurement of the proton and deuteron spin structure functions g_2 and asymmetry $A(2)$. *Phys. Lett.* **B458**, 529–535 (1999).

[25] D. Adams et al.. Spin structure of the proton from polarized inclusive deep-inelastic muon proton scattering. *Phys. Rev.* **D56**, 5330–5358 (1997).

[26] E. S. Ageev et al.. Measurement of the spin structure of the deuteron in the dis region. *Phys. Lett.* **B612**, 154–164 (2005).

[27] R. G. Roberts. The structure of the proton: Deep inelastic scattering. Cambridge, UK: Univ. Pr. (1990) 182 p. (Cambridge monographs on mathematical physics).

[28] E. Leader. Spin in particle physics. *Camb. Monogr. Part. Phys. Nucl. Phys. Cosmol.* **15**, 1 (2001).

[29] E. Leader and E. Predazzi. An introduction to gauge theories and the 'new physics.'. Cambridge, Uk: Univ. Pr. (1982) 498p.

[30] M. Anselmino, A. Efremov, and E. Leader. The theory and phenomenology of polarized deep inelastic scattering. *Phys. Rept.* **261**, 1–124 (1995).

[31] David J. Griffiths. Introduction to elementary particles. NEW YORK, USA: WILEY (1987) 392p.

[32] Vincenzo Barone, Alessandro Drago, and Philip G. Ratcliffe. Transverse polarisation of quarks in hadrons. *Phys. Rept.* **359**, 1–168 (2002).

[33] M. Dueren. The HERMES experiment: From the design to the first results. Hamburg DESY - Int.Rep.HERMES-95-02 (95/07,rec.Aug.) 234 p.

[34] S. D. Drell and J. D. Walecka. Electrodynamic processes with nuclear targets. *Ann. Phys.* **28**, 18–33 (1964).

[35] A. C. Benvenuti et al.. A high statistics measurement of the proton structure functions $F_2(x, Q^2)$ and r from deep inelastic muon scattering at high Q^2. *Phys. Lett.* **B223**, 485 (1989).

[36] M. R. Adams et al.. Proton and deuteron structure functions in muon scattering at 470 GeV. *Phys. Rev.* **D54**, 3006–3056 (1996).

[37] M. Arneodo et al.. Measurement of the proton and deuteron structure functions, $F_2(p)$ and $F_2(d)$, and of the ratio $\sigma(L)/\sigma(T)$. *Nucl. Phys.* **B483**, 3–43 (1997).

[38] L. W. Whitlow, E. M. Riordan, S. Dasu, Stephen Rock, and A. Bodek. Precise measurements of the proton and deuteron structure functions from a global analysis of the slac deep inelastic electron scattering cross-sections. *Phys. Lett.* **B282**, 475–482 (1992).

[39] S. Chekanov et al.. Measurement of the neutral current cross section and F_2 structure function for deep inelastic e^+ p scattering at hera. *Eur. Phys. J.* **C21**, 443–471 (2001).

[40] C. Adloff et al.. Deep-inelastic inclusive e p scattering at low x and a determination of alpha(s). *Eur. Phys. J.* **C21**, 33–61 (2001).

[41] W.-M. Yao et al.. Review of particle physics. *Journal of Physics G* **33**, 1+ (2006).

[42] K. Abe et al.. Measurements of R = σ(L)/σ(T) for $0.03 < x < 0.1$ and fit to world data. *Phys. Lett.* **B452**, 194–200 (1999).

[43] J. Ashman et al.. An investigation of the spin structure of the proton in deep inelastic scattering of polarized muons on polarized protons. *Nucl. Phys.* **B328**, 1 (1989).

[44] P. L. Anthony et al.. Deep inelastic scattering of polarized electrons by polarized ^{3}He and the study of the neutron spin structure. *Phys. Rev.* **D54**, 6620–6650 (1996).

[45] K. Abe et al.. Measurements of the proton and deuteron spin structure functions g_1 and g_2. *Phys. Rev.* **D58**, 112003 (1998).

[46] B. Adeva et al.. A next-to-leading order qcd analysis of the spin structure function g_1. *Phys. Rev.* **D58**, 112002 (1998).

[47] A. Airapetian et al.. Measurement of the proton spin structure function $g_1(p)$ with a pure hydrogen target. *Phys. Lett.* **B442**, 484–492 (1998).

[48] P. L. Anthony et al.. Measurements of the Q^2 dependence of the proton and neutron spin structure functions $g_1(p)$ and $g_1(n)$. *Phys. Lett.* **B493**, 19–28 (2000).

[49] K. Ackerstaff et al.. Measurement of the neutron spin structure function $g_1(n)$ with a polarized ^{3}He internal target. *Phys. Lett.* **B404**, 383–389 (1997).

[50] J. D. Bjorken and Emmanuel A. Paschos. Inelastic electron proton and gamma proton scattering, and the structure of the nucleon. *Phys. Rev.* **185**, 1975–1982 (1969).

[51] R. P. Feynman. Photon-hadron interactions. Reading 1972, 282p.

[52] G. Zweig. An SU(3) model for strong interaction symmetry and its breaking. CERN-TH-412.

[53] M. Arneodo et al.. A reevaluation of the Gottfried sum. *Phys. Rev.* **D50**, 1–3 (1994).

[54] Guido Altarelli and G. Parisi. Asymptotic freedom in parton language. *Nucl. Phys.* **B126**, 298 (1977).

[55] Marc Virchaux and Alain Milsztajn. A measurement of alpha-s and higher twists from a QCD analysis of high statistics F_2 data on hydrogen and deuterium targets. *Phys. Lett.* **B274**, 221–229 (1992).

[56] Michael E. Peskin and D. V. Schroeder. An introduction to quantum field theory. Reading, USA: Addison-Wesley (1995) 842 p.

[57] Kenneth G. Wilson. Nonlagrangian models of current algebra. *Phys. Rev.* **179**, 1499–1512 (1969).

[58] Wolfhart Zimmermann. Normal products and the short distance expansion in the perturbation theory of renormalizable interactions. *Ann. Phys.* **77**, 570–601 (1973).

[59] Kurt Gottfried. Sum rule for high-energy electron - proton scattering. *Phys. Rev. Lett.* **18**, 1174 (1967).

[60] D. A. Ross and Christopher T. Sachrajda. Flavor symmetry breaking in anti-quark distributions. *Nucl. Phys.* **B149**, 497 (1979).

[61] P. Amaudruz et al.. The Gottfried sum from the ratio $F_2(n)/F_2(p)$. *Phys. Rev. Lett.* **66**, 2712–2715 (1991).

[62] S. A. Larin. The next-to-leading QCD approximation to the Ellis-Jaffe sum rule. *Phys. Lett.* **B334**, 192–198 (1994).

[63] F. E. Close and R. G. Roberts. Consistent analysis of the spin content of the nucleon. *Phys. Lett.* **B316**, 165–171 (1993).

[64] R. Michael Barnett et al.. Review of particle physics. particle data group. *Phys. Rev.* **D54**, 1–720 (1996).

[65] Philip G. Ratcliffe. SU(3) breaking in hyperon beta decays: A prediction for $\Xi^0 \to \Sigma^+ e\bar{\nu}$. *Phys. Rev.* **D59**, 014038 (1999).

[66] J. D. Bjorken. Applications of the chiral U(6)$\bigotimes$U(6) algebra of current densities. *Phys. Rev.* **148**, 1467–1478 (1966).

[67] C. Caso et al.. Review of particle physics. *Eur. Phys. J.* **C3**, 1–794 (1998).

[68] John R. Ellis and Robert L. Jaffe. A sum rule for deep inelastic electroproduction from polarized protons. *Phys. Rev.* **D9**, 1444 (1974).

[69] C. Adloff et al.. Measurement of event shape variables in deep inelastic e p scattering. *Phys. Lett.* **B406**, 256–270 (1997).

[70] J. Breitweg et al.. Measurement of multiplicity and momentum spectra in the current and target regions of the breit frame in deep inelastic scattering at hera. *Eur. Phys. J.* **C11**, 251–270 (1999).

[71] B. R. Webber. Hadronization. (1994).

[72] Torbjorn Sjostrand. High-energy physics event generation with pythia 5.7 and jetset 7.4. *Comput. Phys. Commun.* **82**, 74–90 (1994).

[73] Torbjorn Sjostrand et al.. High-energy-physics event generation with pythia 6.1. *Comput. Phys. Commun.* **135**, 238–259 (2001).

[74] Torbjorn Sjostrand, Stephen Mrenna, and Peter Skands. Pythia 6.4 physics and manual. *JHEP* **05**, 026 (2006).

[75] Philipp Geiger. Measurement of fragmentation functions at HERMES. DESY-HERMES-98-05.

[76] Hugh A. M. Tallini. A measurement of the quark spin distributions of the nucleon at HERMES. DESY-HERMES-98-24.

[77] R. D. Field and R. P. Feynman. A parametrization of the properties of quark jets. *Nucl. Phys.* **B136**, 1 (1978).

[78] Bo Andersson, G. Gustafson, G. Ingelman, and T. Sjostrand. Parton fragmentation and string dynamics. *Phys. Rept.* **97**, 31 (1983).

[79] K. Ackerstaff et al.. HERMES spectrometer. *Nucl. Instrum. Meth.* **A417**, 230–265 (1998).

[80] A. A. Sokolov and I. M. Ternov. On polarization and spin effects in the theory of synchrotron radiation. *Phys. Dokl.* **8**, 1203–1205 (1964).

[81] A. Airapetian et al.. The HERMES polarized hydrogen and deuterium gas target in the hera electron storage ring. *Nucl. Instrum. Meth.* **A540**, 68–101 (2005).

[82] A. Nass et al.. The HERMES polarized atomic beam source. *Nucl. Instrum. Meth.* **A505**, 633–644 (2003).

[83] J. T. Brack et al.. The HERMES forward tracking chambers: Construction, operation, and aging effects. *Nucl. Instrum. Meth.* **A469**, 47–54 (2001).

[84] A. Andreev et al.. Multiwire proportional chambers in the HERMES experiment. *Nucl. Instrum. Meth.* **A465**, 482–497 (2001).

[85] S. Bernreuther et al.. Design and performance of the large HERMES drift chambers. *Nucl. Instrum. Meth.* **A367**, 96–99 (1995).

[86] S. Bernreuther et al.. The HERMES back drift chambers. *Nucl. Instrum. Meth.* **A416**, 45–58 (1998).

[87] N. Akopov et al.. The HERMES dual-radiator ring imaging cerenkov detector. *Nucl. Instrum. Meth.* **A479**, 511–530 (2002).

[88] W. R. Leo. Techniques for nuclear and particle physics experiments: A how to approach. Berlin, Germany: Springer (1987) 368 p.

[89] A. T. Maas. Particle identification with rich detectors: Algorithms and their optimization. a case study on the experiments ceres and HERMES. DESY-THESIS-2000-051.

[90] H. Avakian et al.. Performance of the electromagnetic calorimeter of the HERMES experiment. *Nucl. Instrum. Meth.* **A417**, 69–78 (1998).

[91] T. Benisch et al.. The luminosity monitor of the HERMES experiment at desy. *Nucl. Instrum. Meth.* **A471**, 314–324 (2001).

[92] Thomas Benisch. Polarized bhabha scattering and luminosity measurement at the HERMES experiment. (in german). DESY-HERMES-98-45.

[93] C. Weiskopf. Untersuchung der bhabha-asymmetrien mit dem HERMES-luminositaetsmonitor. DESY-HERMES-1998-042.

[94] U. Elschenbroich. Analysis of luminosity monitor data for different years. page 13pp (2002). DESY-HERMES-02-013.

[95] U. Elschenbroich. Bhabha-streuung and luminositaetsmessung in HERMES-experiment. (2001). DESY-HERMES-01-044.

[96] G. Schnell. Longitudinal polarization of the lambda in deep inelastic scattering of polarized positrons from nucleons. DESY-HERMES-1999-037.

[97] F. Meissner et al.. Photoproduction trigger at HERMES. DESY-HERMES-1996-026.

[98] F. Meissner. Measurement of the j/ψ cross section and double spin asymmetries in vector meson production in polarized lepton-nucleon scattering at HERMES. DESY-HERMES-2000-014.

[99] The HERMES target group. The polarization of HERMES target and its error for the deuterium running in 2000. DESY-HERMES-2002-010.

[100] K. Hagiwara et al.. Review of particle physics. *Phys. Rev.* **D66**, 010001 (2002).

[101] Wolfgang Andreas Lachnit. The rear HERMES drift chambers and their influence on systematic errors of asymmetry measurements. (in german). DESY-HERMES-98-41.

[102] Ahmed El Alaoui. La contribution du quark étrange au spin du proton. HERMES-05-048.

[103] A. Miller. Applying radiative corrections to ratios of cross sections for deeply inelastic scattering.

[104] Bernd A. Kniehl, G. Kramer, and B. Potter. Fragmentation functions for pions, kaons, and protons at next-to-leading order. *Nucl. Phys.* **B582**, 514–536 (2000).

[105] S. Kretzer. Fragmentation functions from flavour-inclusive and flavour-tagged e^+e^- annihilations. *Phys. Rev.* **D62**, 054001 (2000).

[106] L. Bourhis, M. Fontannaz, J. P. Guillet, and M. Werlen. Next-to-leading order determination of fragmentation functions. *Eur. Phys. J.* **C19**, 89–98 (2001).

[107] J. Pumplin et al.. New generation of parton distributions with uncertainties from global qcd analysis. *JHEP* **07**, 012 (2002).

[108] A. Airapetian et al.. Quark helicity distributions in the nucleon for up, down, and strange quarks from semi-inclusive deep-inelastic scattering. *Phys. Rev.* **D71**, 012003 (2005).

[109] M. Gluck, E. Reya, M. Stratmann, and W. Vogelsang. Models for the polarized parton distributions of the nucleon. *Phys. Rev.* **D63**, 094005 (2001).

[110] Y. Goto et al.. Polarized parton distribution functions in the nucleon. *Phys. Rev.* **D62**, 034017 (2000).